NUMERICAL STUDY ON CAPILLARITY- DOMINANT FREE SURFACE AND INTERFACIAL FLOWS

by

ZHAOYUAN WANG

Presented to the Faculty of the Graduate School of

The University of Texas at Arlington in Partial Fulfillment

of the Requirements

for the Degree of

DOCTOR OF PHILOSOPHY

THE UNIVERSITY OF TEXAS AT ARLINGTON

May 2006

ACKNOWLEDGEMENTS

I would like to express my gratitude to my supervising professor, Dr. Albert. Y. Tong, for leading me into this wonderful and interesting research field. I really appreciate his guidance, support, help and endless friendliness during the nearly four years of study and life at The University of Texas at Arlington. Dr. Tong was always ready and available when I needed his help. I am really thankful for his time sacrificed for our meetings at weekend or during vacations and his patience during those long meetings. Every discussion was so fruitful where I could always get hints and new ideas encouraging and stimulating me to better understand the problems and overcome the difficulties. It is a great pleasure to work with Dr. Tong and I am lucky to be his student.

I would also like to thank my committee members, Dr. J. Craig Dutton, Dr. C. Q. Liu, Dr. D. R. Wilson and Dr. S. M. You, for their suggestions and advice on this work. I am especially thankful to Dr. Dutton for his constructive editorial suggestions.

I am really grateful for the assistantship offered by the Aerospace and Mechanical Engineering Department at UTA. This support is essential for me to maintain financial security without which I could not have completed this work.

Finally, I would like to thank my family for their support, understanding and constant care.

April 11, 2006

ABSTRACT

NUMERICAL STUDY ON CAPILLARITY- DOMINANT

FREE SURFACE AND INTERFACIAL FLOWS

Publication No. _____

Zhaoyuan Wang, PhD.

The University of Texas at Arlington, 2006

Supervising Professor: Albert Y. Tong

The continuum surface force (CSF) method has been extensively employed in the volume-of-fluid (VOF), level set (LS) and front tracking methods to model surface tension forces. Its ability is limited for the surface tension dominant free surface and interfacial flows due to the existence of spurious currents. These currents may lead to disastrous interface instabilities and failure of grid convergence, which are present in all the previous versions of the CSF algorithm. In this study, a coupled level set and volume-of-fluid method (CLSVOF) is employed for interface tracking, which offers more accurate computations of the curvature and the normal vector and excellent mass

conservation properties. The surface tension is modeled by a new surface tension implementation algorithm, referred to as the pressure boundary method (PBM). The surface tension effect is incorporated into the Navier-Stokes equation via a capillary pressure gradient term in the first step of a two-step projection method.

The accuracy and capability of the present algorithms are tested and validated by a series of numerical experiments carried out for both free surface and two-phase interfacial flows. The CLSVOF method demonstrates superiority over the VOF method in surface tension modeling. It has been shown that the PBM method drastically suppresses the spurious currents with the sharp pressure jump condition preserved. The robustness of the PBM method on interfacial flows with large density ratios has also been exhibited. The CLSVOF and PBM methods have been applied to study the pinch-off mechanism of a pendant droplet, the relaxation of an elongated liquid ligament and the dynamics of a gas bubble rising in a vertical tube. The results of the simulations are compared with data from the experimental and theoretical measurements available in the literature, and good agreement has been achieved. The accuracy, robustness and capability of the current numerical methods are further validated through these applications.

TABLE OF CONTENTS

ACKNOWLEDGEMENTS ii

ABSTRACT iii

LIST OF ILLUSTRATIONS viii

LIST OF TABLES xii

Chapter Page

1. INTRODUCTION 1

1.1 Motivation 1

1.2 Organization of Thesis 3

2. LITERATURE REVIEW 4

2.1 Interface Simulation Methods 4

2.1.1 Lagrangian Methods 5

2.1.2 Eulerian Methods 7

2.2 Surface Tension Modeling 11

2.2.1 Surface Tensile Force Method 11

2.2.2 Continuum Surface Force Model 12

2.2.3 Boundary and Jump Condition Method 14

3. MATHEMATICAL FORMULATIONS 17

3.1 Governing Equations 17

3.1.1 Whole-Domain Formulation 17
3.1.2 Jump-Condition Formulation 20
3.2 Interface Tracking 21
3.3 Surface Tension Force Modeling 22
4. CLSVOF METHOD 24
4.1 Introduction 24
4.2 Volume-of-Fluid Method 25
4.3 Level Set Method 26
4.4 Interface Reconstruction 28
4.5 Re-distancing of the Level Set Function 30
4.6 Advection Tests 33
4.6.1 Rotation of a Slotted Disc 34
4.6.2 A Circle in Shearing Flow 34
5. SURFACE TENSION IMPLEMENTATION ALGORITHM 43
5.1 Overview 43
5.2 Continuum Surface Force Model 45
5.3 Pressure Boundary Method 46
5.3.1 PBM Algorithm 47
5.3.2 Capillary Pressure Field Calculation 48
5.4 Numerical Tests and Discussion 54
5.4.1 Free Surface Flows 54
5.4.2 Tests for Two-Phase Interfacial Flows 59

6. APPLICATIONS 81

6.1 Pinch-Off Mechanism of a Pendant Droplet 82

6.1.1 Introduction 82

6.1.2 Initial Configuration and Boundary Conditions 82

6.1.3 Results and Discussion 83

6.2 Relaxation of an Elongated Liquid Ligament 85

6.2.1 Introduction 85

6.2.2 Results and Discussion 87

6.2.3 Conclusions 92

6.3 Motion of a Large-Sized Gas Bubble in a Narrow Vertical Tube 93

6.3.1 Introduction 93

6.3.2 Results and Discussion 96

6.3.3 Conclusions 102

7. CONCLUSIONS AND FUTURE WORK 122

Appendix

A. COMPUTER PROGRAM EXECUTION 126

REFERENCES 132

BIOGRAPHICAL INFORMATION 144

LIST OF ILLUSTRATIONS

Figure Page

2.1 Molecular forces and surface tension..... 15

2.2 Illustration of the surface tensile force exerted at a point $\vec{x}_s$ on an interface element ds 15

2.3 Spurious currents at the interface in the CSF method: (a) spurious currents arising around a droplet; (b) a typical deformed shape of a droplet at the end of the simulation 16

4.1 Flow chart for the CLSVOF scheme: coupling process in the dashed box 36

4.2 A sample VOF data on the mesh representing a circle interface..... 36

4.3 The location of variables on a computational cell. 37

4.4 Level set function values corresponding to a circle over a square grid 37

4.5 Level sets of a falling droplet and a rising bubble. Top: without re-initialization; Bottom: with re-initialization. Contours shown from -0.5 to 0.5 by 0.25, dashed line is the zero contour..... 38

4.6 Possible configurations for the interface reconstruction..... 39

4.7 Possible configurations of the interface for the level set function re-distancing..... 40

4.8 Slotted disc rotation test for the LS, VOF-PLIC and CLSVOF methods respectively..... 41

4.9 A circle in shearing flow test..... 42

5.1 (a) Distribution of surface tension forces in the CSF model. (b) Variation of the magnitude of the body force across the transition region. 65

5.2 Flow diagram for one computational cycle 66

5.3 Discretization of pressure gradient at the interface and determination of the distance fraction q 66

5.4 Gradient discretization across the interface: (a) $q_r > 0.5$; (b) $q_r < 0.5$ 67

5.5 Maximum and mean velocity magnitudes versus time. Grid spacing at top: 0.04×0.04; middle: 0.02×0.02; bottom: 0.01×0.01 68

5.6 Velocity profiles for a stationary droplet at 0.5ms: (a) VOF-CSF; (b) CLSVOF-CSF; (c) CLSVOF-PBM. Grid: 0.02×0.02. 69

5.7 Pressure distribution for a static droplet at time 0.5ms: (a) VOF-CSF; (b) CLSVOF-CSF; (c) CLSVOF-PBM 70

5.8 Time sequence and velocity profiles of a falling droplet in air, CLSVOF used in both cases 71

5.9 Schematic representation of an elongated liquid ligament 71

5.10 Breakup sequence of an elongated liquid ligament: (a)VOF-CSF; (b) CLSVOF-CSF; (c) CLSVOF-PBM. Dash: 0.06×0.06; dash-dot: 0.03×0.03; solid: 0.015×0.015; dot: 0.0075×0.0075 72

5.11 Velocity profiles of an elongated ligament for different methods: top row: earlier stage of the relaxation process; bottom row: immediately prior to the pinch-off occurrence 73

5.12 Velocity vector field for cases with different density ratios (PBM on the left, CSF on the right): (a) r_l / r_g =1; (b) r_l / r_g =100; (c) r_l / r_g =1000 74

5.13 Maximum velocity magnitude versus time for different density ratios. 75

5.14 Pressure distribution: (a)PBM method; (b)CSF method. 75

5.15 Maximum velocity magnitude versus time for different mesh sizes 76

5.16 Time evolution of drop shapes for different methods: (a) CSF; (b) PBM 77

5.17 Velocity profiles of a falling drop at one time instant: (a) CSF; (b) PBM..... 78

5.18 Air bubble rising in water with different diameters..... 79

5.19 Numerical and experimental rise velocities versus bubble diameter..... 80

6.1 The schematic of pendant drop forming from a vertical capillary tube..... 103

6.2 The initial flow field of water droplet computation..... 104

6.3 (a)-(o) The evolution of a pendant drop from a tube of inner radius R_i = 1.0 mm and outer radius R = 1.6 mm at the liquid flow rate Q = 10 mL/min with a parabolic inlet velocity profile. The numerical scheme is the VOF-PLIC 105

6.4 (a)-(o) The evolution of a pendant drop from a tube of inner radius R_i = 1.0 mm and outer radius R = 1.6 mm at the liquid flow rate Q = 10 mL/min with a parabolic inlet velocity profile. The numerical scheme is the CLSVOF..... 106

6.5 (a)-(m) Time sequence of a pendant water droplet from a tube in air 107

6.6 Comparison of characteristic values of water droplets as a function of the liquid flow rate..... 108

6.7 Schematic representation of an elongated ligament: (a)a full ligament with elliptic ends; (b) computational domain configuration 108

6.8 Pressure and velocity distribution during relaxation process: (a) pressure distribution along the axis of the ligament; (b) velocity profile 109

6.9 Flow field and pressure distribution immediately prior to breakup (magnified view): (a) flow field; (b) pressure distribution 110

6.10 Ligament relaxation process with different end shapes: (a) circular shape; (b) reference case (elliptic shape); (c) more elliptic shape; (d) pencil-head shape..... 111

6.11 Relaxation process of an elongated ligament with pencil-head end shape: (a) Pressure distribution along the axis of the ligament; (b) Velocity profile, magnified the dashed region of (a) 112

6.12 Relaxation processes of a ligament with different Oh numbers: (a) Oh=0.2018; (b) Oh=0.1009; (c) Oh=0.0678; d) Oh=0.0101. 113

6.13 Initial configuration of the computational domain 114

6.14 Time dependent deformation sequence of a single air bubble in a narrow tube 114

6.15 Velocity vector field and streamline plot at one time instant 115

6.16 Velocity field (magnified views): (a) top region; (b) side region; (c) wake region 116

6.17 The axial velocity versus time at the nose and bottom of the bubble 117

6.18 (a) Pressure contour plot. (b) Pressure distribution along the centerline of the tube at various radial positions 117

6.19 The variation of bubble length versus time 118

6.20 Power spectra for the oscillations of the bottom velocity and bubble length 118

6.21 Bubble rise velocity at the nose and bottom for different cases: (a) high viscosity ($10n$); (b) low viscosity ($0.1n$); (c) high surface tension ($2.0\,s$); (d) low surface tension ($0.5\,s$) 119

6.22 Spectra of bubble bottom velocity oscillations: (a) viscosity effect; (b) surface tension effect 120

6.23 Time evolution of the bubble shapes for different cases: (a) high viscosity;(b) low viscosity; (c) high surface tension; (d) low surface tension 121

6.24 (a) Bubble rise velocity at the nose and bottom of the bubble with a higher surface tension ($10\,s$). (b) Time evolution of bubble shapes 121

LIST OF TABLES

Table Page

5.1 Maximum and Mean Velocity Magnitude after 0.5 ms, time step: Δt =1.0e-4, 1.0e-5, 1.0e-6 for three grids respectively 55

5.2 Relative Differences of Ligament Volume between Consecutively Reduced Grid Sizes at One Time Instant 59

7.1 Comparison of the Accuracy and Capability of Different Methods for Free Surface and Two-Phase Interfacial Flows 123

CHAPTER 1

INTRODUCTION

1.1 Motivation

Interfacial and free surface flows are common phenomena in fluid dynamics, which appear in various natural and engineering processes. An enormous number of engineering applications can be found in a wide range of areas such as rocket engines, chemical reactors, contamination spreading, multiphase mixture transport, cavitation, ink-jet printing, particle transport in blood, crystallization, multiphase cooling, fluidized beds, drying of gases and air entrainment in oceans and rivers. Surface tension dominant flows with large flow distortions, such as deformation and breakup of liquid particles and bursting and coalescence of gas bubbles, attract much attention of researchers [1-9]. Due to the fact that these phenomena often occur on scales of space and time for which experimental methods, such as visualization techniques, are difficult and sometime impossible to perform, numerical simulation serves as a useful alternative to better understand such flows.

The challenge arising in the numerical simulation of interfacial and free surface flows is the moving surface between two immiscible fluids with distinct physical properties, the shape, location and movement of which need to be identified and determined. The interface and flow field interact dynamically in the sense that the

interface moves under the action of the flow field, and the flow field is affected by the position of the interface. When the surface tension force is dominant, the flow field is greatly dependent on the geometric properties of the surface such as the curvature and normal at the interface. In that case, accurate modeling of the surface tension force and representation of the interface are critical. The numerical methods currently available for surface tension modeling often cause instabilities and exhibit a poor convergence property due to the singular nature of the surface tension at the interface [10], which is especially serious for interface modeling methods on fixed grids. When the surface tension force is dominant and the density jump is large, catastrophic numerical instabilities may occur in the computations.

The objective of this thesis is to investigate and develop numerical methods for surface tension dominant interfacial and free surface flows, in order to increase the accuracy of the interface representation and improve on the modeling of the surface tension force. A surface tension implementation algorithm, referred to as the pressure boundary method (PBM), has been developed, which is used in conjunction with a coupled level set and volume-of-fluid method (CLSVOF) [11-14] for the tracking of the interface. The integrated algorithm is incorporated into a finite-volume single-phase flow solver [15, 16], where a two-step projection method on a fixed grid is employed. It is subsequently extended to two-phase interfacial flows for which different physical properties across the interface are considered.

It should be mentioned that, for convenience, the term free surface flow refers to flows with single phase, and two-phase flow refers to interfacial flow. Free surface flow

is a limiting case of flows with an interface, where the dynamic effect of one phase (usually gas) is neglected and the jump condition at the interface becomes a boundary condition. This simplifies the problems for the cases for which one of the two phases has insignificant influence on the dynamics of the system considered.

1.2 Organization of Thesis

In Chapter 2, a literature review on interface simulation methods and surface tension modeling algorithms is presented. Mathematical formulations are presented in Chapter 3, which include governing equations, interface tracking and surface tension force modeling methods. The coupled level set and volume-of-fluid (CLSVOF) scheme is discussed in Chapter 4 along with the results of numerical tests. In Chapter 5, the PBM surface tension implementation algorithm is described. Comparisons of the numerical results with different methods are made and the accuracy and superiority of the present scheme are demonstrated.

Several applications of the CLSVOF method and the new surface tension model are presented in Chapter 6. They serve as further evidence for the accuracy and capability of the numerical algorithms developed in this thesis. Finally, conclusions and future work are given in Chapter 7.

CHAPTER 2

LITERATURE REVIEW

2.1 Interface Simulation Methods

Over the past few decades, a number of numerical methods have been developed for interface simulation [10, 17]. Generally, these methods can be divided into two categories depending on the way the interface is represented and followed, and the type of grids used. They are classified as either Lagrangian or Eulerian methods [17]. In the Lagrangian methods, the interface is usually defined as a series of discrete points which are tracked explicitly, and the interface is maintained as a discontinuity. Lagrangian methods allow precise representation of the interface, and are more accurate for problems with small interfacial deformations. In the Eulerian methods, the interface is represented by appropriate field functions, such as fluid fractions, on a fixed grid, and the interface is captured implicitly. Specific advection schemes are required in order to preserve the sharpness of the interfacial front. Eulerian methods are preferred for flows with complex topological changes and interface deformations. Under the categories of Lagrangian and Eulerian methods, the numerical techniques popularly used for interface simulation are briefly reviewed in the following.

2.1.1 Lagrangian Methods

Lagrangian based methods track the interface explicitly and the exact location of the interface is obtained directly by solving the equations of motion:

$$\frac{d\vec{x}_i}{dt} = \vec{V}_i \tag{2-1}$$

where $\vec{x}_i$ is the position vector and $\vec{V}_i$ the velocity vector of the interface. Moving grid, front tracking, boundary integral and particle-based methods belong to this category. A brief discussion is given in the following.

2.1.1.1 Moving Grid Method

Moving grid methods have been particularly successful for studies of small amplitude waves and weakly deformed bubbles [18-20]. In the moving grid methods, a Lagrangian grid is constructed where the interface is a boundary between two sub-domains. When the grid moves with the fluid, the interface is automatically tracked by the grid. Many finite-element methods use this approach. Generally, for interfacial flows undergoing small deformation with regular topologies, the moving grid method can yield very accurate solutions. When the interface undergoes large deformations, the solution accuracy will deteriorate and may lead to the termination of the simulation if the element connectivity rules are violated. In this case, the computational domain needs to be re-meshed either by keeping the original mesh connectivity constant or allowing it to change. Applications of the moving grid method can be found in [21-23].

2.1.1.2 Front Tracking Method

The front tracking method originates from the marker-and-cell (MAC) method [24] and the subsequent extension made by Daly [25]. Its applications can be found in a variety of interfacial flow problems [26-30]. In the front tracking method, the interface is represented by Lagrangian markers connected to form a front that moves through a stationary Eulerian grid. The front tracking method, which tracks the exact location of the interface explicitly, achieves a high degree of accuracy by representing the interface with high-order interpolation polynomials. However, the handling of topological changes is often artificial rather than physical. Mass conservation is another weakness that the front tracking method fails to address.

2.1.1.3 Boundary Integral Method

For some special cases, such as inviscid or creeping flows, boundary integral methods can be used. For inviscid flows, the Navier-Stokes equation is reduced to the Euler equation where the interface is both a free boundary between phases and a vortex sheet [31]. The flow solution in the entire domain is deduced from the discrete points along the interface. For creeping flows, Stone and Leal [6, 7] have applied a boundary integral method to study the deformation, relaxation and breakup processes of a viscous drop. In their method, it is assumed that the inertia of the fluid flow can be neglected.

The major advantage of the boundary integral method is the reduction of the flow problem by one dimension. In addition, highly accurate solutions can be obtained if the flow has a regular topology. However, its extension to 3-D problems is very

difficult, and artificial manipulation is necessary for local interface transformation when dealing with severe topological changes.

2.1.1.4 Particle-Based Method

In the particle-based methods, the macroscopic fluid in the domain is represented by a number of discrete particles, which carry mass, momentum and energy. The interface is automatically tracked by identifying the position of each individual particle. Particle-based methods eliminate the grid partially, such as the particle-in-cell (PIC) method [32], or completely, such as the smoothed particle hydrodynamics (SPH) method [33, 34].

Particle-based methods are able to handle topological changes easily due to the fact that each individual particle can move freely. The numerical diffusion across interfaces can be completely eliminated by using particle motion to approximate the advection terms. Moreover, it is relatively simple and straightforward to extend the implementation from 2-D to 3-D. However, the fatal drawback of the particle-based method is that it is extremely expensive in terms of CPU time and memory requirements, which prohibits its use in practical applications.

2.1.2 Eulerian Methods

In the Eulerian methods, the interface is represented by an appropriate field function *C*, which is advanced by solving an advection equation:

$$\frac{DC}{Dt} = \frac{\partial C}{\partial t} + \left(\vec{V} \bullet \nabla\right) C = 0 \qquad (2\text{-}2)$$

The interface is implicitly captured and can be reconstructed from the updated field functions according to their properties. This category includes continuum advection,

volume tracking, level set, and phase field methods, which will be discussed briefly in the following.

2.1.2.1 Continuum Advection Method

The continuum advection method refers to traditional difference methods for solving the advection Equation (2-2). The equation is a simple hyperbolic type that can be solved with various techniques such as first-order upwind, high-order monotonic van Leer [35], PPM [36], and TVD [37] schemes. Continuum advection schemes have been employed as interface tracking methods in mold filling simulations [38]. This kind of scheme is designed upon the premise that C in Equation (2-2) is smoothly varying. However, when C is discontinuous, such schemes will have interface diffusion problems if the convection term is approximated by standard spatial differences of C directly across the interface. Even with higher-order approximations, the numerical diffusion will broaden the interface to an unacceptable width of as many as four to eight cells. One approach to fix the interface diffusion problem is to transform the discontinuous C function into another smooth and continuous function f, then solve Equation (2-2) with f, and finally transform f back to C. This idea, proposed in [39], is the basic premise of the level set method.

2.1.2.2 Volume Tracking Method

Volume tracking methods originated in the early 1970s [40-42] are the most widely used Eulerian approaches for interface tracking. In the volume tracking method, the interface is captured by the VOF function which represents the volume fraction occupied by the liquid phase in each computational cell. Interface locations are

reconstructed from the VOF function, and usually non-diffusive and geometric techniques are used to advect the VOF function in order to keep the interface sharp.

Various improvements and developments have been made over the last three decades [43]. Recently, a more accurate interface reconstruction scheme, the piecewise linear interface construction (PLIC) method, has been employed [44-45]. One of the most important advantages of the VOF method is that mass can be conserved exactly; however, the interface normal and curvature can not be estimated accurately from the VOF function whose spatial derivatives are not continuous near the interface.

2.1.2.3 Level Set Method

The level set method was first introduced by Osher and Sethian [46]. Its application has expanded from modeling interfacial phenomena in fluid dynamics to image enhancement, computer recognition, grid generation, and so on [47, 48].

In the level set method, the interface is described by the level set function $f(\vec{x},t)$ which is defined as a signed distance function. Its magnitude equals the shortest distance from the interface to the cell center with its sign being negative inside the interface and positive outside of the interface. At the interface, the level set function is zero.

The LS function is advanced by the following advection equation:

$$\frac{\partial f}{\partial t} = -(\vec{V} \bullet \nabla) f \tag{2-3}$$

The discretization of the above equation is straightforward, because the LS function is smooth and continuous. However, it has been found that the LS function will fail to be a

distance function after being advanced by Eq. (2-3) and a re-initialization process [49] is needed for its return to a distance function. The reinitialization process generally is not mass conservative, which is the major drawback of the level set method.

2.1.2.4 Phase Field Method

Although phase field methods have been successfully used in the simulation of solidification microstructures [50], their applications to Navier-Stokes flows are fewer [51]. In this method, a phase field variable y is defined on a fixed grid, which is assumed to be discrete values of 1 in one phase and 0 in the other.

Phase field methods are based on the model of fluid free energy where the interfacial energy density depends upon both y and gradients of y. The phase field variable y can be updated by solving the Cahn-Hilliard equation [51]:

$$\frac{\partial y}{\partial t} + (\vec{V} \bullet \nabla) y = a \nabla^2 j \qquad (2\text{-}4)$$

where a is the diffusion parameter, called the mobility, and j is the chemical potential, defined as the rate of change of the free energy with respect to y. The advantage of this method is that simple standard schemes for the advection terms can be used. The main drawback of the phase field methods is that a wide numerical interfacial layer is usually needed which might cause problems. Nevertheless, phase field formulations for interfacial flows are still new and deserve further attention and exploration.

It should be noted that this review of interface simulation methods remains at an introductory level. Some methods are emphasized; some are omitted and not mentioned.

Comprehensive and detailed discussions on each particular method can be found in the relevant references given in this thesis.

2.2 Surface Tension Modeling

Within a fluid, the intermolecular forces of attraction are balanced in all directions. However, for the fluid molecules at or near the surface, the cohesive forces are unbalanced due to the discontinuity of fluid properties at the interface (see Figure 2.1). The unbalanced forces of intermolecular attraction at the surface result in the surface tension effect, which causes the interface to behave like an elastic membrane.

The surface tension force plays a significant role in some important interfacial flow problems such as droplet deformation, bubble motion, liquid ligament breakup, *etc*. The accurate computation of surface tension is one of the most critical elements of numerical methods devised for free surface and interfacial flows. The accuracy and choice of surface tension modeling methods are closely related to the interface tracking approaches. In the following, a brief review on surface tension modeling techniques associated with different interface tracking methods is given.

2.2.1 Surface Tensile Force Method

In the conventional front tracking methods, the surface tension force is calculated directly on the Lagrangian interface grid [52-54], and then distributed to the fixed Eulerian grid. Provided the precise location of the interface is known, it is probably the most straightforward way to treat the surface tension as a surface tensile force that is pulling along the interface. In the two-dimensional case, with reference to Figure 2.2, the surface tension force on an element of the interface can be written as:

$$\vec{F}_s(\vec{x}_s) = \int_1^2 s\, d\vec{t} = s\,(\vec{t}_2 - \vec{t}_1) \tag{2-5}$$

where s is the surface tension coefficient and $\vec{t}_1$ and $\vec{t}_2$ are unit tangent vectors at the ends of an interface element. In this method, only the tangents at the end points of an interface element need be found; curvature is not necessary. The advantage of this form is that it exactly preserves the conservation property that the sum of the surface tension forces around a closed surface identically equals zero.

This method is commonly used in the front tracking approaches [53, 55] where the interface can be explicitly represented with discrete points and elements. For the Eulerian based capture methods, in which the precise locations of the interface are not offered, this model may fail.

2.2.2 Continuum Surface Force Model

The continuum surface force (CSF) model has been extensively used in the VOF and level set methods to model surface tension force since it was first introduced by Brackbill *et al.* [56]. In the CSF method, the surface tension effect is treated as a body force distributed within a transition region of finite thickness at the interface across which the fluid properties are assumed to change continuously from one fluid to another. The body force is located at the grid points acting on the fluid elements everywhere in the transition region. Since the surface tension force is no longer applied exactly at the interface, the precise interface location is not required.

The basic idea of this method is that the volume integral of the body force is equal to the surface integral of the surface tensile force in the limit of infinitesimally small transition region thickness h:

$$\lim_{h\to 0}\int_{dV}\vec{F}_b(\vec{x})dV=\int_{dS}\vec{F}_{sa}(\vec{x}_s)dS \tag{2-6}$$

where $\vec{x}_s$ is a position vector at the interface, and $\vec{F}_{sa}$ the surface force per unit interfacial area, given by:

$$\vec{F}_{sa}=\frac{d\vec{F}_s}{ds}=s\,\frac{d\vec{t}(\vec{x}_s)}{ds}=s\,k(\vec{x}_s)\vec{n}(\vec{x}_s) \tag{2-7}$$

The body force is given by:

$$\vec{F}_b=s\,k(\vec{x})\vec{n}(\vec{x})d(\vec{x}) \tag{2-8}$$

where s is the coefficient of surface tension, k the mean curvature, $\vec{n}$ the normal to the surface, and $d(\vec{x})$ a delta function concentrated at the interface. It can be proved that the expression on the right hand side of Equation (2-8) satisfies the identity in the integral equation (2-6). Detailed derivation and proof can be found in reference [56].

This body force is included in the momentum equations as a source term. The continuum treatment of the discontinuous change at the interface eases the implementation of the surface tension effect where only the VOF function or the LS function is needed. In problems with complex topological changes, the CSF model shows robustness and versatility over the conventional method. However, the CSF model has been found to generate so-called spurious currents in the neighborhood of the interface [45, 57, 58]. When the surface tension forces are dominant, these vortex-like currents may destroy the interface and lead to disastrous instabilities at the interface

(see Figure 2.3). This often leads to failure of convergence upon grid refinement as well.

2.2.3 Boundary and Jump Condition Method

At the interface between two immiscible fluids, the surface stress condition in the normal direction is given by

$$p_v - p + s\,k = -2\mu\frac{\partial u}{\partial n} \tag{2-9}$$

where k is the local free surface curvature, s the surface tension coefficient, μ the dynamic viscosity, p_v the vapor (gas) pressure, n the free surface normal and u the velocity. For two-phase flows, the surface tension effect serves as an internal jump condition for the pressure at the interface. Direct application of this jump condition is difficult, and requires the solution of a more complicated elliptic problem [59].

For free surface flows, viscous effects are negligible and Eq. (2-9) is reduced to the Laplace's formula:

$$p - p_v = s\,k \tag{2-10}$$

The gas side pressure, p_v, is taken as constant, and then the surface tension effect becomes a Dirichlet pressure boundary condition, which can be easily applied at the free surface. This method is well suited for moving and adaptive grid methods [10]; its application can be found in the VOF [60] and MAC [61] methods for free surface flows.

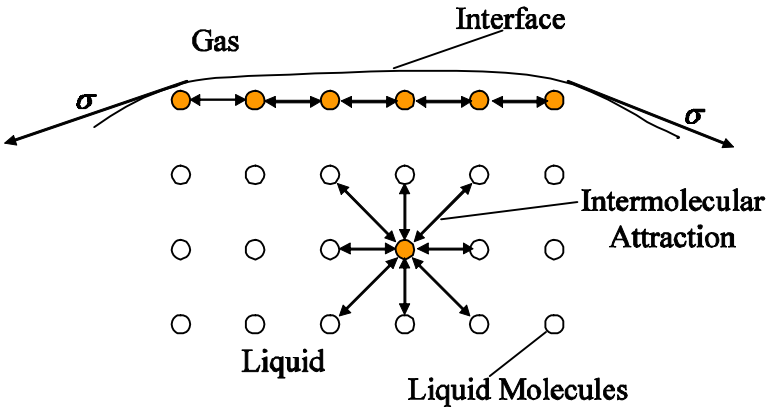

Figure 2.1 Molecular forces and surface tension.

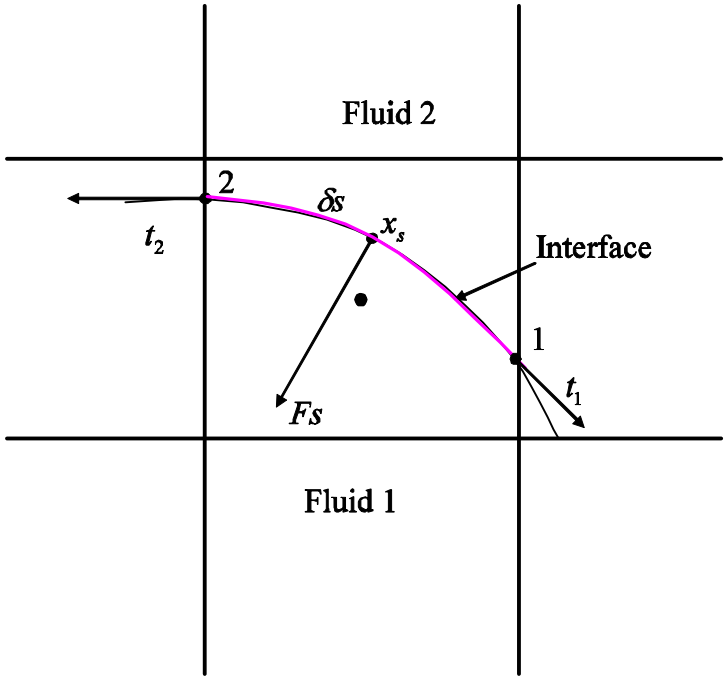

Figure 2.2 Illustration of the surface tensile force exerted at a point $\vec{x}_s$ on an interface element ds.

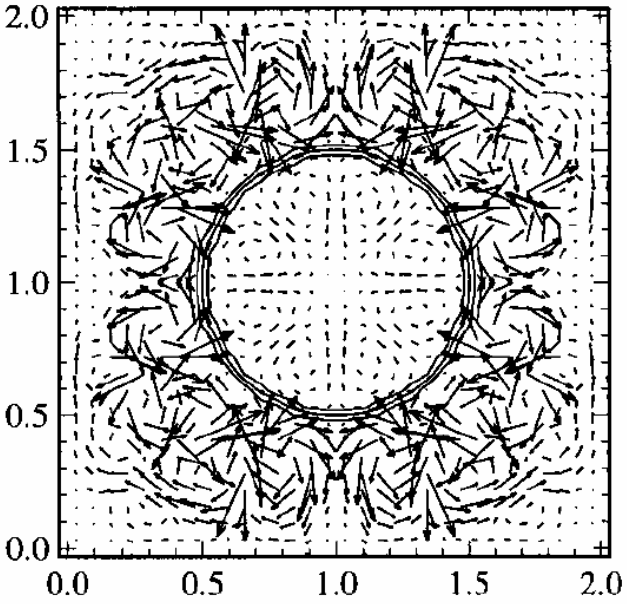

(a)

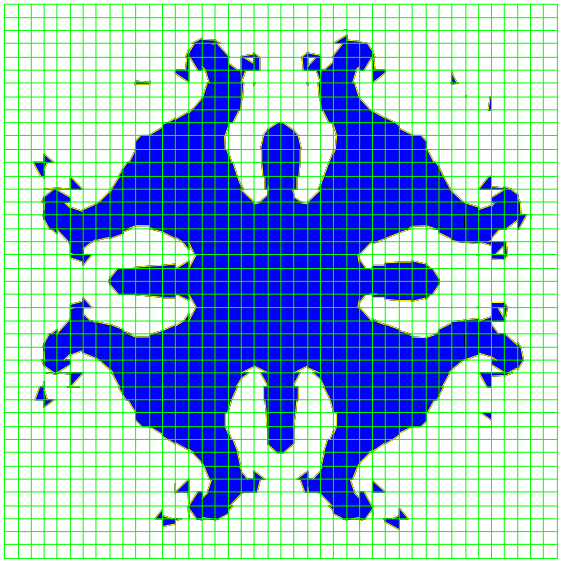

(b)

Figure 2.3 Spurious currents at the interface in the CSF method: (a) spurious currents arising around a droplet [Rudman, 1998]; (b) a typical deformed shape of a droplet at the end of the simulation [Meier *et al.*, 2002].

CHAPTER 3

MATHEMATICAL FORMULATIONS

3.1 Governing Equations

For two incompressible, immiscible fluids that are separated by a moving surface, the motion of both fluids can be described by the Navier-Stokes equations. The discontinuities in physical properties such as density, viscosity and surface tension at the interface can be treated in different ways; accordingly, the governing equations are reformulated into two types: whole-domain (one-field) and jump-condition (multi-field) formulations [10].

3.1.1 Whole-Domain Formulation

The whole flow domain considered can be divided into some sub-domains which are occupied by different fluids. At the interface, the discontinuous physical properties, such as density, viscosity and surface tension can be smoothed over a transition region of finite thickness. Thus, the whole flow domain can be described by a single set of momentum and continuity equations within the "one-field" formulation approach, where different fluid properties are considered in each individual phase. Proper stress conditions at the interface between different phases are enforced implicitly. With the assumption that the fluid properties are constant in both phases, the governing equations are written as:

$$\nabla \bullet \vec{V} = 0 \tag{3-1}$$

$$\frac{\partial \vec{V}}{\partial t} + \nabla \bullet (\vec{V}\vec{V}) = -\frac{1}{r}\nabla p + \frac{1}{r}\nabla \bullet t + \vec{g} + \frac{1}{r}\vec{F}_b \tag{3-2}$$

where $\vec{V}$ is the velocity, r the density, p the pressure, t the viscous stress tensor, $\vec{g}$ the gravitational acceleration and $\vec{F}_b$ the body force. For Newtonian fluids, the stress tensor, t , can be written as

$$t = 2mS \tag{3-3}$$

where m is the dynamic viscosity and S is the strain rate tensor given by:

$$S = \frac{1}{2}\left[\left(\nabla \vec{V}\right) + \left(\nabla \vec{V}\right)^T\right] \tag{3-4}$$

The effective density and viscosity at each grid point are evaluated as:

$$r = r_g(1-H) + r_l H \tag{3-5}$$

$$m = m_g(1-H) + m_l H \tag{3-6}$$

where subscripts g and l denote gas and liquid respectively; H is a step function smoothed over three grid spacings to prevent numerical instability arising from steep density gradients [49], defined as:

$$H \equiv \begin{cases} 1 & if\ f \geq +1.5h \\ 0 & if\ f \leq -1.5h \\ 0.5 + f/3h + [\sin(2\pi f/3h)]/2\pi & if\ |f| \leq 1.5h \end{cases}$$

where f is the level set function, and h is the grid spacing.

Equation (3-2) is discretized as

$$\frac{\vec{V}^{n+1}-\vec{V}^{n}}{dt}=-\nabla\bullet(\vec{V}\vec{V})^{n}-\frac{1}{r^{n}}\nabla p^{n+1}+\frac{1}{r^{n}}\nabla\bullet t^{n}+\vec{g}^{n}+\frac{1}{r^{n}}\vec{F}_{b}^{n} \tag{3-7}$$

where the superscripts n and n+1 represent the value of the variable at consecutive time steps. The only implicit term in the above equation is the pressure. Gravity, advection, surface tension and viscosity are approximated with old time t^{n} values.

A two-step projection method [16] is used where Equation (3-7) is decomposed into two equations:

$$\frac{\tilde{\vec{V}}-\vec{V}^{n}}{dt}=-\nabla\cdot\left(\vec{V}\vec{V}\right)^{n}+\frac{1}{r^{n}}\nabla\cdot t^{n}+\vec{g}^{n}+\frac{1}{r^{n}}\vec{F}_{b}^{n} \tag{3-8}$$

and

$$\frac{\vec{V}^{n+1}-\tilde{\vec{V}}}{dt}=-\frac{1}{r^{n}}\nabla p^{n+1} \tag{3-9}$$

where $\tilde{\vec{V}}$ is the intermediate value of velocity. In the first step, the intermediate velocity field, $\tilde{\vec{V}}$, is obtained from the previous time step after accounting for the effects of advection, viscosity, gravity, and body forces. In the second step, the velocity field, $\vec{V}^{n+1}$, is projected onto a zero-divergence vector field resulting in a pressure Poisson equation given by

$$\nabla\cdot\left[\frac{1}{r^{n}}\nabla p^{n+1}\right]=\frac{\nabla\cdot\tilde{\vec{V}}}{dt} \tag{3-10}$$

which can be solved by using an incomplete Cholesky conjugate gradient (ICCG) solution technique [62].

3.1.2 Jump-Condition Formulation

In contrast to the "one-field" model, where the discontinuous properties, such as density, viscosity and surface tension, at the interface are treated in a continuum fashion, an alternative method treats the discontinuities as jump conditions. The entire flow domain is decomposed into a number of bulk-phase domains within which the usual nonsingular Navier-Stokes equation holds. Across the interface between different domains, some quantities, such as velocities, should be continuous, whereas others, such as pressure, should have specific jumps.

The jump conditions at the interface include the pressure boundary condition written in tensor form as:

$$p_v - p + s\,k = -2\mu n_k \frac{\partial u_k}{\partial n} \tag{3-11}$$

for the normal direction, and the velocity boundary condition:

$$\mu(t_i \frac{\partial u_i}{\partial n} + n_k \frac{\partial u_k}{\partial s}) = \frac{\partial s}{\partial s} \tag{3-12}$$

for the tangential direction, where $\frac{\partial}{\partial s}$ and $\frac{\partial}{\partial \mathrm{n}}$ are the surface and normal derivatives respectively. With a constant surface tension coefficient, the term on the right hand side of Equation (3-12) will be zero.

Away from the interface, the Navier-Stokes equation is written as:

$$\frac{\partial \vec{V}}{\partial t} + \nabla \bullet (\vec{V}\vec{V}) = -\frac{1}{\rho}\nabla p + \frac{1}{\rho}\nabla \bullet \tau + \vec{g} \tag{3-13}$$

and the continuity equation remains the same as Equation (3-1). Equation (3-13) is then discretized as:

$$\frac{\vec{V}^{n+1}-\vec{V}^{n}}{dt} = -\nabla \bullet (\vec{V}\vec{V})^{n} - \frac{1}{r^{n}}\nabla p^{n+1} + \frac{1}{r^{n}}\nabla \bullet t^{n} + \vec{g}^{n} \qquad (3\text{-}14)$$

Equation (3-14) can be solved by the same two-step projection method as discussed in the previous section with proper jump conditions applied at the interface. In this study, the surface tension effect is treated as a pressure jump condition; the implementation algorithm for this will be detailed in Chapter 5.

3.2 Interface Tracking

The choice of the interface tracking approach is dependent on the physical problem under consideration. As mentioned in Chapter 1, the problems of interest in the present study are capillarity-dominant free surface and interfacial flows with large flow distortions and topological changes, for which the Eulerian based methods are better suited. The volume-of-fluid (VOF) method [15-17, 42, 44, 45] and the level set (LS) method [49], as two Eulerian-based methods, have been extensively used. They both use phase functions to track the interface implicitly: volume fraction for the VOF method and distance function for the LS method.

One of the advantages of these methods is that they can easily handle flow problems with large topological changes and interface deformations such as liquid ligament breakup, bubble merging and bursting, and droplet elongation and breakup. As discussed in Chapter 2, however, each method has its own strengths and weaknesses. The VOF method has the desirable property of mass conservation, but lacks accuracy

on the normal and curvature calculations due to discontinuous spatial derivatives of the VOF function near the interface. On the other hand, the normal and curvature can be calculated accurately from the continuous and smooth distance functions in the LS method. One serious drawback of this method is that mass conservation is often violated. To overcome such weaknesses of the LS method and the VOF method, the coupled level set and volume-of-fluid (CLSVOF) method has recently been explored [11-14]. The implementation algorithm of the CLSVOF method in this study will be discussed in detail in the next chapter.

3.3 Surface Tension Force Modeling

The continuum surface force (CSF) model is commonly used in the volume-of-fluid (VOF) and level set (LS) methods to model the surface tension force. As mentioned in Chapter 2, the CSF model interprets the surface tension force as a body force, $\vec{F}_b$, distributed within a transition region of finite thickness at the interface. It has shown its robustness and versatility over the conventional methods.

In the continuum method, the surface tension force is smoothed out over a finite thickness involving several layers of computational cells. This smoothing of a discontinuity is actually detrimental and results in numerical errors that worsen with increasing width of the smoothing region. On a fixed orthogonal grid, the mass contained in a given cell is to be accelerated by the body force. In the transition region, the body force and the mass often do not vary at the same rate. While the mass approaches a small value near the free surface, the body force may still maintain a relatively large value. This will lead to an increase in flow acceleration and

consequently the formation of spurious currents. This severely limits its ability to model capillarity-dominant flows.

In the present study, a new surface tension implementation algorithm, referred to as the pressure boundary method (PBM), is introduced. The surface tension force is incorporated into the Navier-Stokes equation via a capillary pressure gradient term in the first step of a two-step projection method. The details of this implementation algorithm will be given in Chapter 5.

CHAPTER 4

CLSVOF METHOD

4.1 Introduction

The basic idea for the CLSVOF method is to combine the strengths of the LS method with the VOF method in order to represent and capture the interface more accurately. In general, the interface is reconstructed via a piecewise linear interface construction (PLIC) scheme from the VOF function and the interface normal vector computed from the LS function. Based on the reconstructed interface, the level set functions are re-distanced via a geometric procedure for achieving mass conservation. By taking advantage of both the VOF and LS methods, the CLSVOF method is able to compute the normal and curvature more accurately while mass conservation is well satisfied. A flow chart for the CLSVOF algorithm is shown in Figure 4.1. The coupling of the LS and VOF methods occurs at the interface reconstruction and the re-distancing of the level set function.

It should be noted that the implementation of the PLIC scheme is not unique; various implementation algorithms have been reported. The same is true with the CLSVOF method where different re-distance implementation schemes have been attempted. In the present study, the PLIC scheme presented by Rudman [44, 45] is used and the LS re-distance algorithm proposed by Son and Hur [13] is followed. A brief

introduction of the VOF and LS methods is given next, followed by the CLSVOF algorithm.

4.2 Volume-of-Fluid Method

In the volume-of-fluid method, the interface is tracked by the VOF function which is defined as the liquid volume fraction in a cell with its value between zero and one in a surface cell and at zero and one in air and liquid respectively, i.e.,

$$F(\vec{x},t)=\begin{cases}1, & \text{in the fluid,}\\ 0<\mathrm{F}<1, & \text{at free surface,}\\ 0, & \text{external to fluid.}\end{cases} \tag{4-1}$$

An example for the VOF functions representing a circle is shown in Figure 4.2. The number in each cell denotes the volume fraction occupied by the liquid. The VOF functions are advanced by the following propagating equation:

$$\frac{\partial F}{\partial t}+(\vec{V}\bullet\nabla)F=0 \tag{4-2}$$

In order to preserve mass, Equation (4-2) is rewritten in the conservative form:

$$\frac{\partial F}{\partial t}+\nabla\bullet(\vec{V}F)=F(\nabla\bullet\vec{V}) \tag{4-3}$$

It is discretized temporally and decomposed into two fractional steps, for the two-dimensional case, given by:

$$\frac{\tilde{F}-F^{n}}{dt}+\frac{\partial}{\partial x}\left(uF^{n}\right)=\tilde{F}\frac{\partial u}{\partial x} \tag{4-4}$$

$$\frac{F^{n+1}-\tilde{F}}{dt}+\frac{\partial}{\partial y}\left(v\tilde{F}\right)=F^{n+1}\frac{\partial v}{\partial y} \tag{4-5}$$

where $\tilde{\tilde{F}}$ is the intermediate VOF function. On the staggered grid, the VOF function, *F*, is located at the cell center and velocities, *u* and *v*, are stored at the cell edges, as shown in Figure 4.3. Discretizing the above equations spatially and integrating over a computational cell (i, j) yields:

$$\tilde{\tilde{F}}_{i,j} = \frac{F_{i,j}^{n} dx_i dy_j - dtdy_j \left(flux_{i+\frac{1}{2},j} - flux_{i-\frac{1}{2},j} \right)}{dx_i dy_j - dtdy_j \left(u_{i+\frac{1}{2},j} - u_{i-\frac{1}{2},j} \right)} \tag{4-6}$$

$$F_{i,j}^{n+1} = \frac{\tilde{\tilde{F}}_{i,j} dx_i dy_j - dtdx_i \left(flux_{i,j+\frac{1}{2}} - flux_{i,j-\frac{1}{2}} \right)}{dx_i dy_j - dtdx_i \left(v_{i,j+\frac{1}{2}} - v_{i,j-\frac{1}{2}} \right)} \tag{4-7}$$

where $flux_{i\pm 1/2,j} = (uF^{n})_{i\pm 1/2,j}$ and $flux_{i,j\pm 1/2} = (v\tilde{\tilde{F}})_{i,j\pm 1/2}$. They denote VOF fluxes across the edges of the computational cell. However, $F_{i\pm 1/2,j}$ and $F_{i,j\pm 1/2}$ are the VOF functions at the cell edges which are not defined. Direct arithmetic interpolation from the neighboring cell-centered values results in serious numerical errors because *F* is not continuously distributed across the interface. A geometric calculation procedure, referred to as interface reconstruction, is necessarily adopted.

4.3 Level Set Method

The LS function, f, is defined as a signed distance function whose magnitude equals the shortest distance from the interface. Its sign is determined as:

$$f(\vec{x},t)\begin{cases} > 0, \text{outside of the interface,} \\ = 0, \text{at the interface,} \\ < 0, \text{inside the interface.} \end{cases} \tag{4-8}$$

The zero level set contours are used to represent the interface. The LS function data corresponding to a circle are shown in Figure 4.4. All the LS values are located at the cell center and assigned as the shortest distance to the interface. The LS function is initialized as a distance function because of its important property, namely, $|\nabla f| = 1$, which can be used to make a number of simplifications.

After initialization, the LS function is moved with the flow field, according to the following advection equation:

$$\frac{\partial f}{\partial t} + (\vec{V} \bullet \nabla) f = 0 \tag{4-9}$$

Since the LS function is smooth and continuous, the discretization of Equation (4-9) is much more straightforward and some simple advection schemes can be used.

It should be noted that the LS function will fail to be a distance function (i.e., $|\nabla f| \neq 1$) after being advanced by Eq. (4-9). After some period of time, the LS functions become irregular as shown in Figure 4.5. In some regions, the level sets pile up on each other, increasing the local gradient, while in other regions, the level sets separate from each other, flattening out the gradient. In order to reduce numerical errors, the level set function must be reinitialized, which can be achieved by obtaining a steady-state solution of the following equation:

$$\frac{\partial f}{\partial t} = \frac{f_0}{\sqrt{f_0{}^2 + h^2}}(1 - |\nabla f|) \tag{4-10}$$

where f_0 is the LS function of the previous time step, *t* the artificial time, and *h* the grid spacing. Equation (4-10) can be re-written in the form:

$$\frac{\partial f}{\partial t} + (\vec{w} \bullet \nabla) f = \frac{f_0}{\sqrt{{f_0}^2 + h^2}} \tag{4-11}$$

where $\vec{w}$ is the propagating velocity normal to the interface with unity magnitude, given by:

$$\vec{w} = \frac{f_0}{\sqrt{{f_0}^2 + h^2}} \left(\frac{\nabla f}{|\nabla f|} \right) \tag{4-12}$$

The zero level set is propagated both inwards and outwards in the normal direction. The level set function will return to a distance function after the reinitialization process.

It is well known that the advection and reinitialization processes do not guarantee mass conservation. The LS functions must be re-distanced prior to being used. This is achieved by calculating the distance geometrically from the cell center to the reconstructed interface.

4.4 Interface Reconstruction

The purpose of the interface reconstruction is to locate the interface from the discrete VOF and LS functions by a specific scheme. As previously discussed, the interface reconstruction serves two purposes: one is to calculate the VOF fluxes across each computational cell with an interface, and the other is to re-distance the LS function for achieving mass conservation. The interface configuration is not unique, and different approximations of the interface have been used [44]. In this study, a piecewise linear interface construction (PLIC) algorithm presented by Rudman [44, 45] is

adopted. The interface within each cell is approximated by a straight line segment the orientation of which is given by the normal vector. The properly oriented interface is then located in the cell such that the area (volume) is determined from the VOF function.

In the CLSVOF method, the normal vector to the interface is estimated from the smooth LS function as:

$$\vec{n} = \frac{\nabla f}{|\nabla f|} = \nabla f \tag{4-13}$$

This is different from the usually "pure" VOF method where discontinuous VOF functions in the neighboring cells are used [16]. The orientation angle of the interface is then defined as:

$$a = \tan^{-1}\left(\frac{n_y}{n_x}\right) (0 < a \le 2p) \tag{4-14}$$

where a is the angle that the outward pointing unit surface normal makes with the positive x-axis. By rotating each interfacial cell such that a lies in the range of $0 \le a \le p/2$, the multitude of possible interface configurations are reduced. As shown in Figure 4.6, only four cases need to be considered. The line segment is moved along the normal direction to fit the shadow area (volume) with the VOF value in the cell. The shadow area (volume) can be calculated by the following n-sided area (volume) formula:

$$A_{xy} = \frac{1}{2}\sum_{i=1}^{n}\left(x_i y_{i+1} - x_{i+1} y_i\right) \tag{4-15}$$

for the two-dimensional case, and

$$V_{rz} = \frac{1}{6}\sum_{i=1}^{n}(r_i + r_{i+1})(r_i z_{i+1} - r_{i+1} z_i) \tag{4-16}$$

for the axisymmetric case. Once the calculated area (volume) matches the VOF value at the cell, the coordinates of endpoints ($\vec{x}_{s1}, \vec{x}_{s2}$) of the line segment are determined, and the reconstruction of the interface is completed. Then, the fluxes for the VOF advection can be evaluated based on the reconstructed interface. Details of this procedure can be found in [15, 45] and are not discussed here.

4.5 Re-distancing of the Level Set Function

After the reconstruction of the interface, the LS functions must be re-distanced in order to achieve mass conservation. The re-distancing of the LS function includes initial determination of the sign of the LS function and the subsequent calculation of the shortest distance from the cell centers to the reconstructed interface through a geometric process.

The sign of the LS function, S^f, is given by:

$$S^f = sign(0.5 - C) \tag{4-17}$$

where *sign* denotes a function that returns the sign of the numeric argument. C is the VOF function for the two-dimensional case. It is obvious that when $C>0.5$, the cell center will fall inside the liquid where the LS function takes the negative sign, and vice versa. For the axisymmetric case, however, C will be the fractional area of the shadowed region as shown in Figure 4.6 rather than the VOF function. Since the VOF function denotes the volume fraction for the axisymmetric case, a value greater than 0.5 does not guarantee that the cell center lies inside the liquid.

Next, the magnitude of the LS function is determined, which is the key step of the re-distancing process. The basic idea is to find the closest point on an interfacial cell to the neighboring cell centers. Although various configurations of the reconstructed interface exist, generally, all the interfacial cells can be simply divided into two cases: single-phase cells (i.e., *F=0 or 1)* and interfacial cells (i.e., *0<F<1*). For two adjoining cells (i, j) and (i', j'), the closest point on cell (i', j') to the center of cell (i, j) will always either be at the corner or the centroid of the cell edges. As a result, these points should always be considered first when calculating the shortest distance associated with two adjoining cells. When cell (i', j') contains a line segment, the closest point on the segment will be either the endpoint or the projection point of the center of cell (i, j). Thus, the possible closest points on cell (i', j') to cell (i, j) can be the corners and edge centers on the cell faces, or the endpoints and projection points on the line segment contained in the cell. As shown in Figure 4.7a, when the cell (i', j') is a full liquid cell, the shortest distances are calculated simply by connecting the centers of the neighboring cells to the corners or face centroids of cell (i', j'). In Figure 4.7b, the nearest point on the shadowed area to point A is its projection point onto the line segment within cell (i', j') rather than the top right corner at all. For a more general case, as shown in Figure 4.7c, for point A and B, the shortest distance is from the cell center to the projection point; for point C and D, the nearest point is the endpoint of the segment, and for the other cells, the closest points on cell (i', j') are either corners or face centroids.

The LS function is re-distanced following the algorithm presented by Son and Hur [13]. The logic procedure is given as:

1. Set the magnitude of the LS function, $|f|$ = large value, and discard all the old values.

2. For each computational cell (i', j'), apply the following procedures:

(a) If the cell (i', j') is a single-phase cell (i.e., $F_{i',j'} = 0$ or 1) and has an adjoining cell (i'', j''), where $|i''-i'| \le 1$ and $|j''-j'| \le 1$, satisfying $S^f_{i'',j''} \neq S^f_{i',j'}$ (refer to Figure 4.7a):

For each neighbor cell (i, j), where $|i'-i| \le 4$ and $|j'-j| \le 4$, satisfying $S^f_{i,j} \neq S^f_{i',j'}$, $|f_{i,j}|$ is assigned to be the shortest distance between cell center $\vec{x}_{i,j}$ and the points $\vec{x}_{i'+m/2,\, j'+n/2}$ on the cell (i', j') faces and vertexes, where $m = \max[-1, \min(1, i-i')]$ and $n = \max[-1, \min(1, j-j')]$, as shown in Figure 4.7a.

(b) If $0 < F_{i',j'} < 1$ (refer to Figures 4.7b, c):

(1)Determine the distance from any neighboring cell center to the segment which is evaluated as $d(\vec{x}) = \vec{n} \bullet (\vec{x} - \vec{x}_{s1})$ or $d(\vec{x}) = \vec{n} \bullet (\vec{x} - \vec{x}_{s2})$, where $\vec{x}_{s1}$ and $\vec{x}_{s2}$ are the end points of the interface obtained in the interface reconstruction procedure.

(2) Then, for each neighbor cell (i,j), $\left|f_{i,j}\right|$ is assigned to be the shortest distance between the cell center $\vec{x}_{i,j}$ and the interface segment or the points $\vec{x}_{i'+m/2,j'+n/2}$ on the cell (i', j') faces:

If $S_{i,j}^{f} \neq sign[d(\vec{x}_{i'+m/2,j'+n/2})]$, (refer to point E of Figure 4.7c),

$$\left|f_{i,j}\right| = \min\left(\left|f_{i,j}\right|, \left|\vec{x} - \vec{x}_{i'+m/2,j'+n/2}\right|\right)$$

Else if the point $\vec{x}_{i,j} - \vec{n}d(\vec{x}_{i,j})$, which is projected from $\vec{x}_{i,j}$ onto the interface, is inside the cell (i', j') (point A and B in Figure 4.7c),

$$\left|f_{i,j}\right| = \min\left(\left|f_{i,j}\right|, \left|d(\vec{x}_{i,j})\right|\right)$$

Otherwise (point C and D of Figure 4.7c),

$$\left|f_{i,j}\right| = \min\left(\left|f_{i,j}\right|, \left|\vec{x}_{i,j} - \vec{x}_{s1}\right|, \left|\vec{x}_{i,j} - \vec{x}_{s2}\right|\right)$$

It should be noted that only the LS functions within the interface neighboring cells are re-distanced; cells several layers away from the interface are not considered, since the LS information is needed only at the vicinity of the interfacial cells for the computations of the normal vector and curvature.

4.6 Advection Tests

In this section, the CLSVOF scheme, along with the LS and VOF methods, is tested with prescribed velocity fields. This allows direct comparison of the advection schemes alone without the involvement of a flow solver.

4.6.1 Rotation of a Slotted Disc

A slotted disc with a radius of 0.6 and slot width of 0.16 is initially located at (2.0, 3.0) on a 4×4 computational domain, as shown in Figure 4.8. A uniform grid of 100×100 is used. This problem, referred to as the Zalesak's problem, is often used for the advection scheme test [63]. The prescribed velocity field is given as:

$$u(x, y) = 2.0 - y, \qquad v(x, y) = x - 2.0$$

with the axis of rotation centered at (2.0, 2.0).

The results are shown in Figure 4.8 after one, two and three rotations for the LS, VOF and CLSVOF methods. In the case of the LS method, the slot has completely vanished after one rotation; as for the VOF and CLSVOF methods, the slot remains even after three rotations although the sharp edges of the slot have been smoothed out. The slotted disc shapes obtained from the VOF and CLSVOF methods are in very close agreement. The improvement of the CLSVOF method over the VOF scheme is not significant.

4.6.2 A Circle in Shearing Flow

A circle evolving in a shearing flow is another challenging test for advection schemes, which involves severe topological changes. A prescribed shearing flow has been proposed by Rudman [44], which is given by:

$$u(x, y) = \sin(x)\cos(y), \;\; v(x, y) = -\cos(x)\sin(y), \;\; 0 \le x, y \le p \;.$$

A circle with a radius of $p/5$ is prescribed at $(p/2, p/4)$ on a domain of $p \times p$. The computational grid chosen is 80×80. The initial configuration and velocity profile are shown at the top row of Figure 4.9. The circle is advanced under the shearing flow

for 800 and 1600 time steps, and then returns back by reversing the flow. In the LS method, serious mass loss can be seen in the figure. Mass conservation is well preserved for the VOF and CLSVOF methods as expected. Again, the results obtained from VOF and CLSVOF methods are very close, and the superiority of the CLSVOF method over the VOF method is not shown.

In the two advection tests, the weakness of the LS method in maintaining the interface sharpness and mass conservation is clearly demonstrated. The improvement of the CLSVOF method over the VOF method is not obvious in the above two tests, which has been confirmed by private discussion with other researchers [64]. This might be explained by the reason that the flow fields in the advection tests are prescribed analytically without variations with time. The shape and topological changes of the interface have no effects on the flow field. However, the superiority of the CLSVOF will be demonstrated when combined with the flow solver for surface tension calculation, which will be discussed in later chapters.

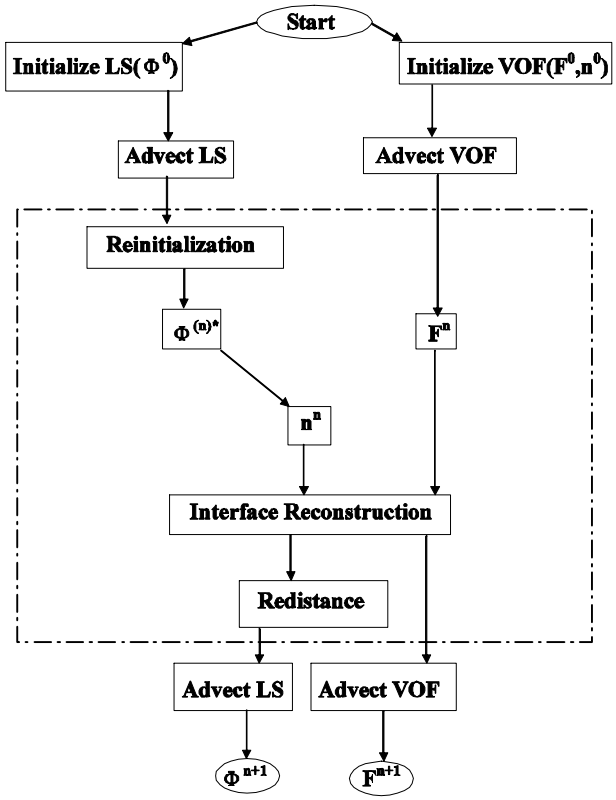

Figure 4.1 Flow chart for the CLSVOF scheme: coupling process in the dashed box.

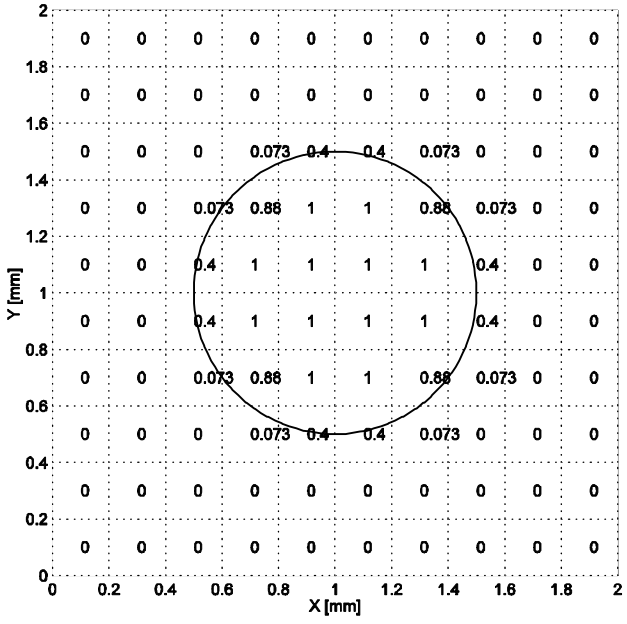

Figure 4.2 A sample VOF data on the mesh representing a circle interface.

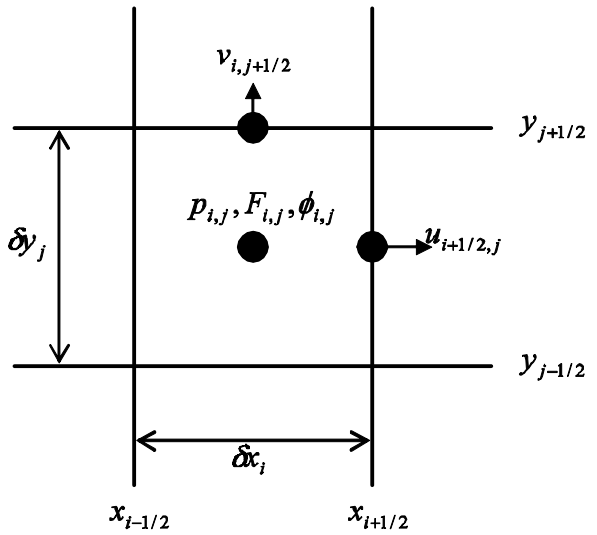

Figure 4.3 The location of variables on a computational cell. The x- and y-velocities are located at the vertical and horizontal cell faces, respectively, and the pressure, the VOF function and the level set function are stored at the cell centers.

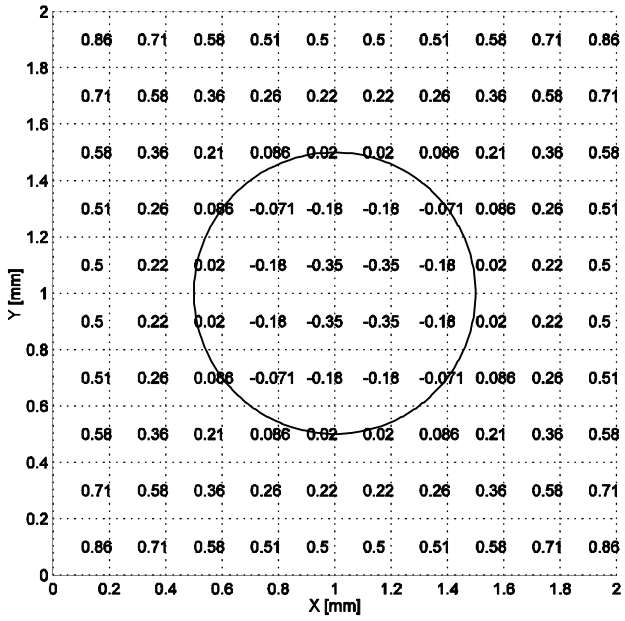

Figure 4.4 Level set function values corresponding to a circle over a square grid.

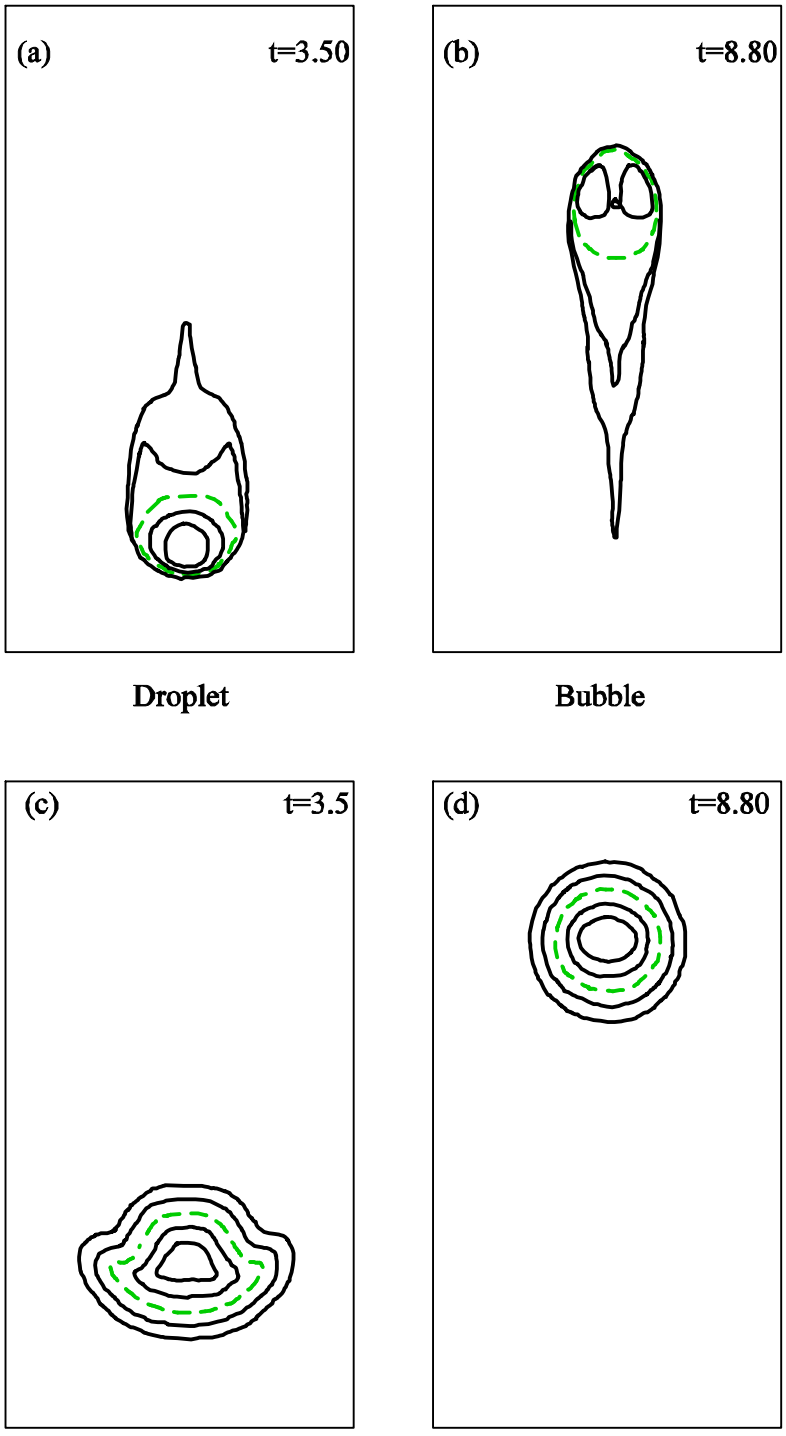

Figure 4.5 Level sets of a falling droplet and a rising bubble. Top: without re-initialization; Bottom: with re-initialization. Contours shown from -0.5 to 0.5 by 0.25, dashed line is the zero contour. [Sussman *et al.*, 1994]

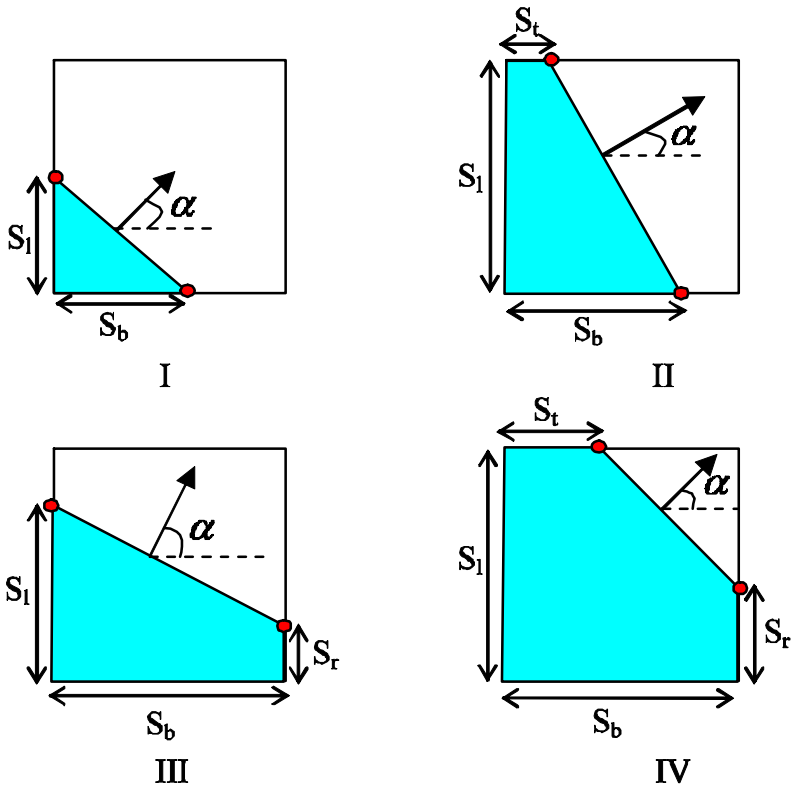

Figure 4.6 Possible configurations for the interface reconstruction.

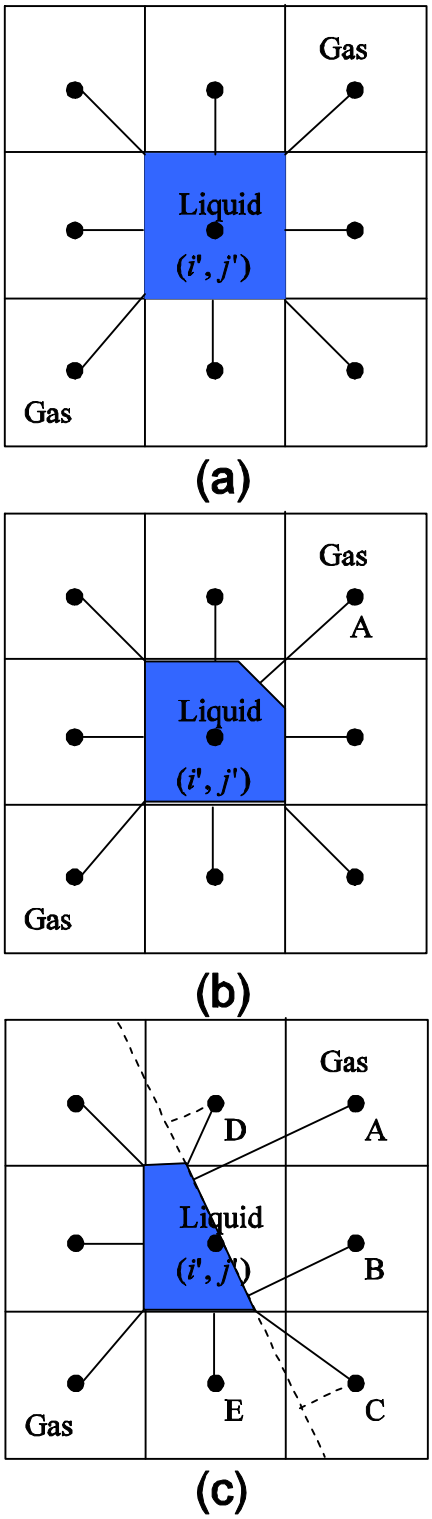

Figure 4.7 Possible configurations of the interface for the level set function re-distancing.

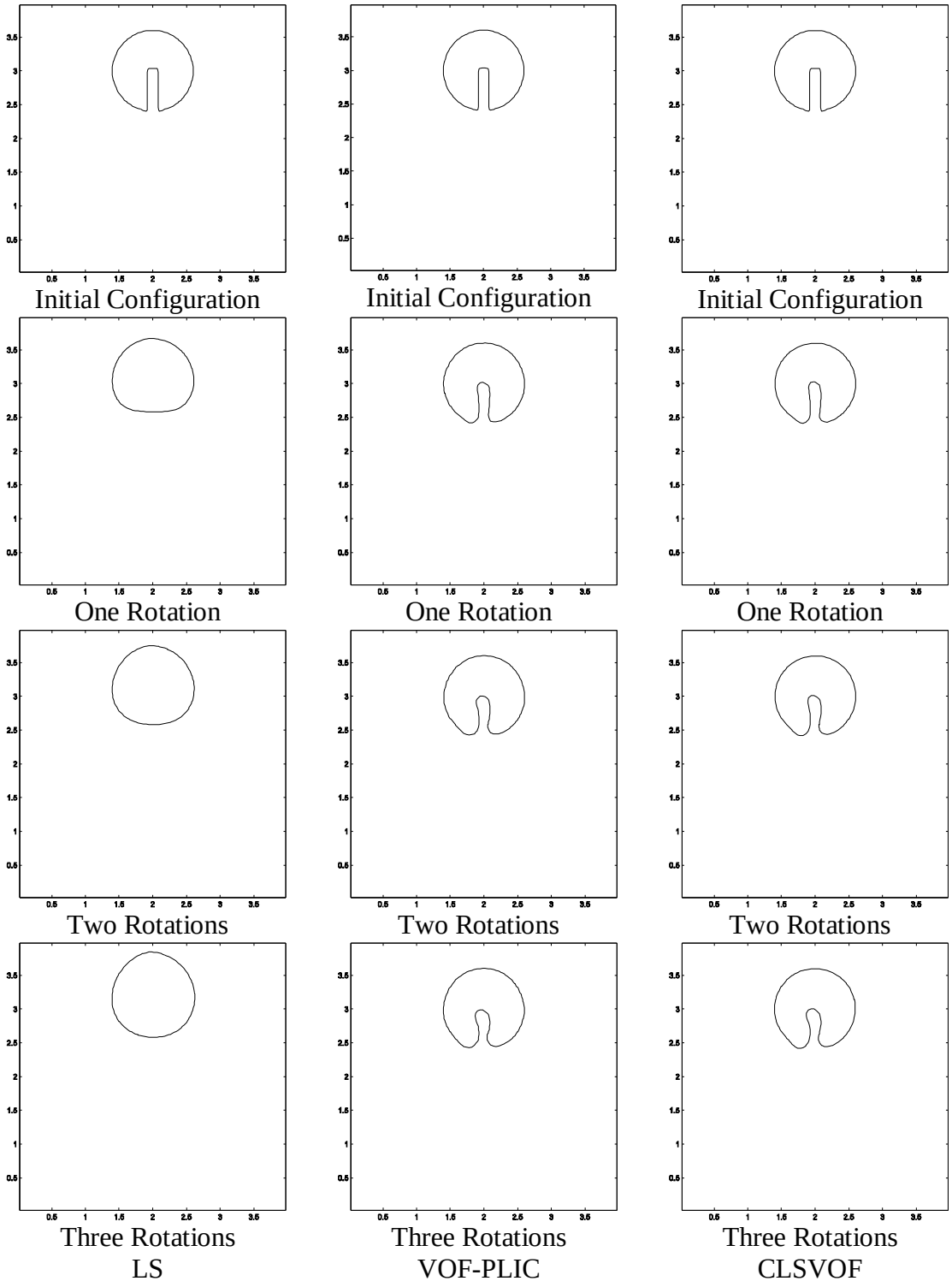

Figure 4.8 Slotted disc rotation test for the LS, VOF-PLIC and CLSVOF methods respectively.

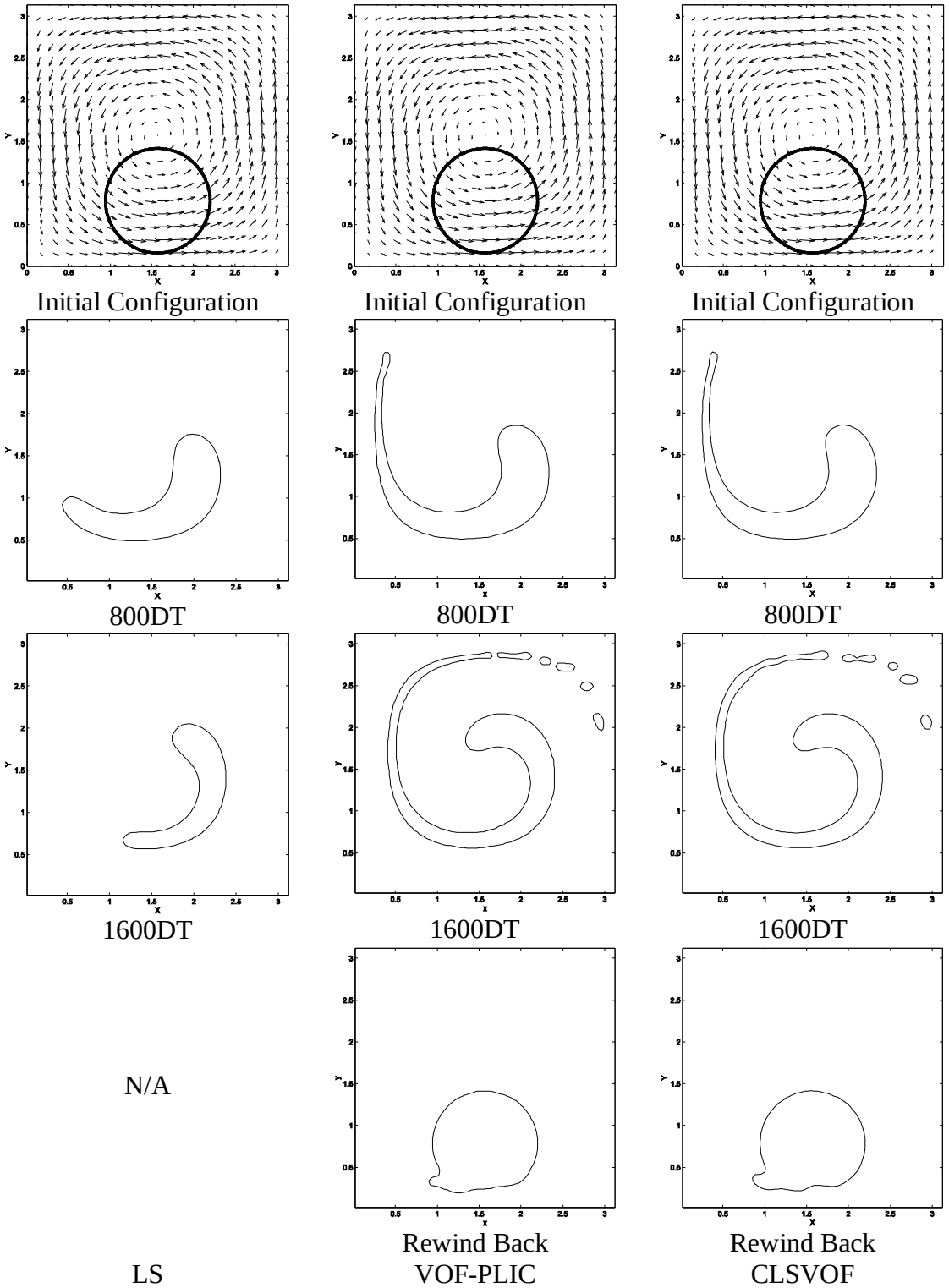

Figure 4.9 A circle in shearing flow test.

CHAPTER 5

SURFACE TENSION IMPLEMENTATION ALGORITHM

5.1 Overview

A major difficulty with many interface simulation methods is the accuracy of modeling the surface tension force, which often deteriorates due to the existence of spurious or parasite currents. These currents are found in most surface tension models [10] and are especially serious when using a fixed Eulerian grid.

In recent studies [45, 54-55, 57-58], much research work has been devoted to suppressing spurious currents and increasing the accuracy of surface tension modeling. Generally, those efforts are focused on two aspects: the accuracy of the curvature estimation and the coupling of the surface tension effect with the flow solver. As for the first aspect, various methods have been devised to represent the interface more accurately. Based on the VOF method, Meier *et al.* [58] have developed a new technique using empirical formulas and data bases which have been generated and stored in a data bank to determine interface curvature. In their algorithm, a third-degree polynomial is used to fit the data. The surface tension force is only applied on the interfacial cells rather than over several computational layers. It is found that the choice of density at the interfacial cells significantly affects the spurious currents. Renardy and Renardy [57] developed a parabolic reconstruction of surface tension (PROST) method

by using a quadratic representation of the surface with a least-squares fit to the VOF functions along with a new body force algorithm. The key idea of their method is that the discrete pressure gradient should be exactly balanced by the body force term at the discrete level. The same idea is adopted by a more recent study carried out by Shin *et al*. [54] in the context of a front tracking method. Popinet and Zaleski [55] use cubic splines to construct the interface but track the interface using marker particles with the volume fractions estimated from the constructed interface. The pressure gradient calculation is improved by a pressure gradient correction procedure. All the studies discussed above greatly contribute to improving the accuracy of surface tension modeling and offer deep insight on the origin of the spurious currents. However, the surface tension effect is still treated as a body force [45, 54, 57-58], or as a source term [55] in the momentum equation, and the surface discontinuity is still numerically smoothed. This numerical smoothing of the discontinuity at the interface is found to be the cause of errors in numerical simulations [65].

Some schemes [59, 65-66] have appeared recently which treat the boundary effects at the interface in a sharp fashion. In [66], the Ghost Fluid Method (GFM) was developed for two-phase compressible inviscid flow, which allows sharp resolution of the contact discontinuities. Kang *et al*. [59] extended this idea to three-dimensional multiphase incompressible flows including the physical effects of viscosity and surface tension. The method proposed in [65] can maintain discontinuous properties at the interface without any artificial smoothing; however, it cannot be applied to viscous flows. The level set method is commonly used in the above studies. Although it offers

the exact sub-cell interface locations, the inherent mass conservation problem in the level set formula remains. Moreover, the sharp treatment of boundary effects sometimes introduces disturbances at the interface which may cause convergence problems, particularly for calculations with less resolved grid spacing.

In the present study, a different surface tension implementation algorithm, referred to as the pressure boundary method (PBM), is introduced. The surface tension effect is treated as a jump condition at the interface rather than being smoothed out over a transition region. The surface tension force is incorporated into the Navier-Stokes equation via a pressure gradient.

5.2 Continuum Surface Force Model

In the CSF model, the surface tension effect is treated as a body force, $\vec{F}_b$, which is distributed within a transition region of finite thickness at the interface, given by:

$$\vec{F}_b = s k \vec{n} d(\vec{x}) \tag{5-1}$$

where s is the coefficient of surface tension, k the mean curvature, $\vec{n}$ the normal to the surface, and $d(\vec{x})$ a delta function concentrated at the interface defined by:

$$d(\vec{x}) \equiv \begin{cases} (1+\cos(2p f/3h))/3h & if\ |f| \le 1.5h \\ 0 & otherwise \end{cases} \tag{5-2}$$

where f is the level set function, and h is the grid spacing. In the context of the VOF method, the delta function $d(\vec{x})$ is replaced by:

$$d(\vec{x}) = |\nabla F| / [F] \tag{5-3}$$

where F is the VOF function, and $[F]$ is the jump of the VOF function [56]. A sketch of a sample CSF distribution is shown in Figure 5.1. Non-zero body forces are only located in the transition regions outside of which no body forces exist. Along an interface normal, the magnitude of the body force exhibits a bell-shaped profile as shown in Figure 5.1b.

The CSF formulation makes use of the fact that numerical models of discontinuities in finite volume schemes are really continuous transitions within which the fluid properties vary smoothly. The surface tension force acts on every fluid element in the transition region.

5.3 Pressure Boundary Method

In the PBM method, the surface tension effect is treated as a sharp boundary condition at the interface for a capillary pressure field. Other discontinuous properties at the interface, such as density and viscosity, however, are treated in a continuous way and weighted by the VOF function:

$$r = r_g(1-F) + r_l F \tag{5-4}$$

$$m = m_g(1-F) + m_l F \tag{5-5}$$

For free surface flows, both r_g and m_g are zero.

It is worthy noting that both the density and viscosity are weighed by the VOF function rather than the Heaviside function as expressed in Equations (3-5) and (3-6). This gives more accurate estimation of the density and viscosity at the interfacial cells, and allows mass conservation to be well preserved. On the other hand, the smearing of

the density and viscosity can prevent disturbances resulting from the otherwise sharp treatment [59].

5.3.1 PBM Algorithm

Basically, the pressure term in Equation (3-14) is separated into two components: one accounting for the surface tension and the other for achieving mass conservation. This enables the surface tension induced sharp pressure conditions at the free surface to be preserved.

The two-step projection method [16] is used where the momentum equation given by Eq. (3-14) is decomposed into the following two equations:

$$\frac{\vec{\tilde{V}} - \vec{V}^{n}}{dt} = -\nabla \bullet (\vec{V}\vec{V})^{n} + \frac{1}{r^{n}} \nabla \bullet t^{n} + \vec{g}^{n} - \frac{1}{r^{n}} \nabla p_{1} \tag{5-6}$$

and

$$\frac{\vec{V}^{n+1} - \vec{\tilde{V}}}{dt} = -\frac{1}{r^{n}} \nabla p_{2} \tag{5-7}$$

where $\vec{\tilde{V}}$ represents an intermediate velocity and

$$p^{n+1} = p_{1} + p_{2} \tag{5-8}$$

Prior to the execution of the two-step projection procedure, p_1 is first computed from the following equation:

$$\nabla \bullet \left[\frac{1}{r^{n}} \nabla p_{1} \right] = 0 \tag{5-9}$$

along with the jump condition induced solely by surface tension at the interface. The discretization of the above equation and the jump conditions applied at the interface will be discussed in a later section.

In the first step of the projection method, an intermediate velocity field $\vec{\tilde{V}}$ is computed from Eq. (5-6). The second step involves taking the divergence of Eq. (5-7) while imposing the incompressibility condition on the velocity field $\vec{V}^{n+1}$ with:

$$\nabla \bullet \vec{V}^{n+1} = 0 \tag{5-10}$$

This results in a single Poisson equation for p_2 given by:

$$\nabla \bullet \left[\frac{1}{r^{n}} \nabla p_2 \right] = \frac{\nabla \bullet \vec{\tilde{V}}}{dt} \tag{5-11}$$

This equation can be readily solved by using an incomplete Cholesky conjugate gradient solution technique. The velocity field $\vec{V}^{n+1}$ is then updated via Eq. (5-7) and the pressure p^{n+1} from Eq. (5-8). A flow chart for the overall computational cycle is given in Figure 5.2.

5.3.2 Capillary Pressure Field Calculation

The capillary pressure field is obtained by solving Eq. (5-9) associated with the internal jump boundary conditions induced by the surface tension effect at the interface. Discretization of Equation (5-9) gives:

$$\frac{(\nabla p_1 / r)_{i+1/2,j} - (\nabla p_1 / r)_{i-1/2,j}}{\Delta x} + \frac{(\nabla p_1 / r)_{i,j+1/2} - (\nabla p_1 / r)_{i,j-1/2}}{\Delta y} = 0 \tag{5-12}$$

The complete pressure jump condition at the interface is given by Equation (3-11), which can be rewritten as:

$$p - p_v = sk + 2\mu n_k \frac{\partial u_k}{\partial n} \tag{5-13}$$

The above equation implies that both the surface tension and viscous stress at the interface contribute to the pressure jump. Since p_1 is extracted to handle the surface tension effect only, the pressure jump condition for solving Equation (5-12) is reduced to Laplace's formula:

$$p - p_v = sk \tag{5-14}$$

The viscous contribution to the pressure jump at the interface will be enforced implicitly as in a "one-field" formulation.

In order to obtain the pressure gradient in Equation (5-12), special discretization techniques need to be adopted for the computational cell at the interface where pressure is not continuous, but rather has sharp variations. The discretization of the pressure gradient will be discussed separately for free surface flow and two-phase interfacial flow in the following.

For free surface flows, the dynamic effect of one phase (e.g., gas) is neglected, where the pressure is treated as constant. Thus, the jump pressure condition becomes a Dirichlet boundary condition at the interface given by:

$$p_I = p_v + sk \tag{5-15}$$

where p_I is the liquid side interface pressure which is used as the boundary value for p_1 in the solution of Eq. (5-12).

The finite difference scheme employed by Gibou *et al.* [67] is adopted here to discretize Eq. (5-12) in the interface regime. With reference to Figure 5.3 and the

pressure subscript 1 dropped, the pressure gradients in Eq. (5-12) at the faces of cell (i, j) are given by:

$$(\nabla p)_{i+1/2,j} = \frac{p_{Ir} - p_{i,j}}{q_r \Delta x} \tag{5-16a}$$

$$(\nabla p)_{i-1/2,j} = \frac{p_{i,j} - p_{i-1,j}}{\Delta x} \tag{5-16b}$$

$$(\nabla p)_{i,j+1/2} = \frac{p_{It} - p_{i,j}}{q_t \Delta y} \tag{5-16c}$$

$$(\nabla p)_{i,j-1/2} = \frac{p_{i,j} - p_{i,j-1}}{\Delta y} \tag{5-16d}$$

where p_{Ir} and p_{It} are pressures at the interface given by Eq. (5-15). q is the fraction of the distance from the interface to the center of cell (i, j) given by (refer to Figure 5.3):

$$\begin{aligned} q_r &= \frac{|f_{i,j}|}{|f_{i,j}| + |f_{i+1,j}|} \\ q_t &= \frac{|f_{i,j}|}{|f_{i,j}| + |f_{i,j+1}|} \end{aligned} \tag{5-17}$$

with the LS function, f, serving as the distance function.

The level set function is used to locate the free surface where its value changes sign and the discretizations given in Eq. (5-16a) and Eq. (5-16c) are applied. Otherwise, standard discretizations given in Eq. (5-16b) and Eq. (5-16d) are used.

For two-phase interfacial flows, the standard discretization method can be used to approximate the pressure gradient at the cell face where there is no interface between

two adjacent cells. For example, refer to Figure 5.4, at the left face of cell (i,j), the derivative is discretized as

$$(\nabla p)_{i-1/2,j} = \frac{p_{i,j} - p_{i-1,j}}{\Delta x} \tag{5-18}$$

On the other hand, if there is an interface between two adjacent cells, special attention must be paid to the discretization of the derivative at the cell face. Because pressure is not continuous across the interface due to the jump conditions induced by the surface tension effect, the standard discretization method described above cannot be applied; otherwise, the pressure profile will be numerically smeared as in the continuum method. A first-order-accurate discretization method was developed in [68] for the variable coefficient Poisson equation with jump conditions. In this method, the pressure gradient at the cell face between two adjacent cells where an interface is located is given by

$$(\nabla p)_{i+1/2,j} = \frac{p_{i+1,j} - (p_{i,j} - sk)}{\Delta x} \tag{5-19}$$

where s is the coefficient of surface tension, and k is the mean curvature. Then, the pressure equation can be discretized as

$$\nabla \bullet \left[\frac{1}{r^n} \nabla P_1 \right]_{i,j} = F^L + F^R + F^T + F^B \tag{5-20}$$

where F^L, F^R, F^T and F^B are source terms. For example, with reference to Figure 5.4a, an interface lies between cell (i, j) and (i+1,j),

$$F^R = \frac{-(\frac{1}{r})_{i+1/2,j}(sk)}{(\Delta x)^2} \tag{5-21}$$

These source terms are zero where no interface exists between two cells.

The basic idea of the above method is to apply the jump conditions, namely,

$$p_{i,j} - p_{i+1,j} = s\,k \tag{5-22}$$

near the interface rather than at the exact interface location.

Considering the sub-cell location enclosed by the interface and the cell faces, in fact, the jump condition is exactly as follows at the interface, refer to Figure 5.4,

$$p_{Il} - p_{Ig} = s\,k \tag{5-23}$$

where p_{Il} is the liquid side interface pressure, and p_{Ig} is the gas side interface pressure. As shown in Figures 5.4a, b, if an interface is crossing two adjacent cells, two possible cases exist. In case a, the right face of the cell (i, j) is within the liquid phase; whereas in case b the right face is in the gas phase.

Refering to Figure 5.4a, the pressure gradient at the right face of cell (i, j) is given by

$$(\nabla p)_{i+1/2,j} = \frac{p_{Il} - p_{i,j}}{q_r \Delta x} \tag{5-24}$$

where q_r is the distance fraction which can be obtained from the level set functions. Substitution of Equation (5-23) into the above equation yields,

$$(\nabla p)_{i+1/2,j} = \frac{(p_{Ig} + s\,k) - p_{i,j}}{q_r \Delta x} \tag{5-25}$$

In the above equation, a new unknown, the gas side pressure p_{Ig}, is introduced. Next, attention will be turned to the determination of this unknown. For free surface flow, the gas side pressure can be taken as constant, then a second-order-accurate

symmetric discretization with Dirichlet boundary conditions, as discussed in the preceding section, may be used. However, for some two-phase flow problems, in which the gas side pressure cannot be taken as constant, then p_{Ig} can be extrapolated by using a high-order polynomial among the points adjacent to the interface. However, this will lead to a non-symmetric discretization which cannot be solved by efficient linear system solvers. To rectify this shortcoming, refer to Figure 5.4a, notice that on the gas side, the interface is much closer to the center of cell (i+1,j); therefore, the variation from p_{Ig} to $p_{i+1,j}$ can be neglected, which means,

$$p_{Ig} \approx p_{i+1,j} \tag{5-26}$$

Substitution of the above equation into Eq. (5-25) gives,

$$(\nabla p)_{i+1/2,j} = \frac{(p_{i+1,j} + sk) - p_{i,j}}{q_r \Delta x} \tag{5-27}$$

Likewise, in case b, the derivative at the right face will be

$$(\nabla p)_{i+1/2,j} = \frac{p_{i+1,j} - p_{Ig}}{(1-q_r)\Delta x} \tag{5-26}$$

Plugging the jump condition into the above equation, one obtains

$$(\nabla p)_{i+1/2,j} = \frac{p_{i+1,j} - (p_{Il} - sk)}{(1-q_r)\Delta x} \tag{5-27}$$

Using pressure $p_{i,j}$ to replace the liquid side interface pressure p_{Il}, and substituting into the above equation gives,

$$(\nabla p)_{i+1/2,j} = \frac{p_{i+1,j} - (p_{i,j} - sk)}{(1-q_r)\Delta x} \tag{5-28}$$

In the y direction, a similar discretization method will be used.

Finally, substituting the pressure gradients into Equation (5-12), a symmetric discretization of the pressure equation is obtained, which can be solved readily by using an incomplete Cholesky conjugate gradient (ICCG) method [62].

5.4 Numerical Tests and Discussion

In this section, a number of numerical experiments have been carried out to validate the accuracy of the PBM algorithm for free surface and two-phase interfacial flows. For free surface flows, first, a stationary droplet is employed to test the static performance, and then the impingement of a falling droplet onto a substrate is modeled. Finally, the relaxation process of an elongated liquid droplet is studied which serves as an example for capillarity-dominant flows. For two-phase interfacial flows, spurious currents at the interface of a stationary circular droplet are investigated first, and then a falling droplet in air and different regimes of gas bubbles rising in water are simulated.

5.4.1 Free Surface Flows

5.4.1.1 A Stationary Droplet in Air

A stationary spherical droplet in the absence of gravity is often used as a benchmark test in the literature on surface tension algorithms for spurious currents [57-58]. Theoretically, in the absence of external forces and initial velocities, the velocity field should remain zero throughout. However, some vortex-like flows in the neighborhood of the interface, referred to as spurious currents in the literature, have been found in many surface tension simulation methods [10].

In the present study, calculations are performed on an axisymmetric computational domain of 1.0 mm×2.0 mm. Water at room temperature and standard atmospheric conditions is used. For comparison purposes, the CSF method is also included in the computations. The CSF method is used in conjunction with both the CLSVOF and the VOF algorithms. The maximum and mean magnitudes of the velocity at 0.5 ms for the different methods are given in Table 5.1.

Table 5.1 Maximum and Mean Velocity Magnitude after 0.5 ms, time step, Δt =1.0e-4, 1.0e-5, 1.0e-6 for three grids respectively.

Method	$\Delta x \times \Delta y$ (mm×mm)	Max. Magnitude (mm/ms)	Mean Magnitude (mm/ms)
VOF-CSF	0.04×0.04	0.3641080	0.00899505
	0.02×0.02	0.4120642	0.00558990
	0.01×0.01	0.5095969	0.00564543
CLSVOF-CSF	0.04×0.04	0.2005396	0.00398587
	0.02×0.02	0.2829645	0.00207592
	0.01×0.01	0.2539782	0.00108487
CLSVOF-PBM	0.04×0.04	0.0067001	6.3110e-005
	0.02×0.02	0.0037879	1.1087e-005
	0.01×0.01	0.0000000	0.0000e-005

As shown in Table 5.1, with the CSF model, the CLSVOF method produces less spurious currents than the VOF method and is hence a better method. This is perhaps not surprising since the estimation of the curvature in the CLSVOF method is more accurate than that in the VOF method. With the CLSVOF method, it is obvious that the PBM method introduced in the present study gives better results than the CSF method with significantly reduced spurious currents.

Figure 5.5 shows the maximum and mean velocity magnitudes versus time plot for the three different methods with various grid sizes. It can be seen that for both CSF

models, i.e. VOF-CSF and CLSVOF-CSF, the magnitude of the velocity increases with time initially and starts fluctuating afterward. On the other hand, the magnitudes of the spurious currents in the CLSVOF-PBM method are under control throughout.

Figure 5.6 shows the velocity profiles for the three different cases. Strong spurious currents can be seen in the vicinity of the free surface for both the VOF-CSF and CLSVOF-CSF methods but are drastically suppressed for the CLSVOF-PBM method. The pressure distributions are shown in Figure 5.7. For the CSF method, it can be seen that the pressure is smeared over 3 to 4 computational cells in the transition region across the interface where it changes gradually from the ambient pressure (taken as zero) to the jump pressure $\Delta P(=sk)$. As for the CLSVOF-PBM method, the pressure changes sharply across the interface and remains rather uniformly distributed inside the drop.

In the CSF model, non-zero pressure gradients are generated in the transition region across the interface due to the smearing nature of the pressure. Consequently, unphysical currents will inevitably be present in the region. This modeling of the surface tension effect is not consistent with the associated sharp pressure jump condition at the interface. As for the PBM method, a relatively uniform pressure field is obtained with very small pressure gradients throughout the droplet. The sharp pressure jump condition at the free surface is preserved and the undesirable spurious currents are significantly reduced.

5. 4.1.2 Impact of a Droplet onto a Substrate

To serve as a test on the dynamic performance of the present algorithm, a falling droplet impinging onto a substrate is simulated. Water droplets of 0.125 mm radius with the same physical properties as in the previous test are used. Droplet surface contours at several time instants are shown in Figure 5.8 with the flow fields given at one of the time instants prior to impingement. The deformations of the droplet after impact are indicated by the free surfaces shown at the bottom.

For droplets with small radius, surface tension will be significant, which tend to maintain a spherical shape. As shown in Figure 5.8, the results obtained with the CSF and PBM methods are in close agreement. The droplet is only slightly flattened at the bottom prior to striking the substrate in the CSF method while it remains spherical with the PBM method throughout. Spurious currents are not visible in either case. This is perhaps due to the fact that the flows are highly dynamic within the droplet and spurious current is relatively insignificant. Nevertheless, the results demonstrate the capability of the PBM scheme in dynamic simulations.

5.4.1.3 Relaxation of a Moderately Elongated Liquid Ligament

Finally, the relaxation process of a moderately elongated liquid ligament is simulated. This is a good example of capillarity-driven free surface flows where the fluid motion is driven by surface tension forces associated with curvature variations along the ligament free surface. The initial configuration of the elongated ligament is shown in Figure 5.9. It is 13.6 mm in length with a radius of 0.3 mm at the cylindrical portion. The bulbous elliptical end shape is based on the experimental findings of Stone

et al. [6]. In order to conserve computational resources, only half of the ligament is considered and the computations are conducted on an axisymmetric domain with dimensions of 7.0 mm×1.0 mm. The liquid used has water properties as in the previous test except for the value of the surface tension, which is 1000 times that of water. Again, VOF-CSF, CLSVOF-CSF and CLSVOF-PBM are used for comparison.

The relaxation sequence leading to the break-up is shown in Figure 5.10. It consists of a relatively rapid bulging of the end followed by break-off of the bulbous end from the central portion of the drop. The numerical results are in excellent agreement with the "end-pinching" mechanism outlined by Stone *et al.* [6, 7]. More details will be presented in Chapter 6.

Calculations have been made with four different meshes for grid convergence studies. As shown in Figure 5.10, grid convergence fails in the VOF-CSF method, while it appears to have been achieved in the CLSVOF-CSF and CLSVOF-PBM methods. Figure 5.11 shows the velocity fields at two time instants. In the CSF method, the spurious currents are pronounced at the earlier stage of the relaxation when the flow is weak and surface tension is dominant, and these currents become invisible prior to the breakup of the ligament when the inertial force is dominant. In the PBM method, the spurious currents are not visible in both stages.

In Table 5.2, the relative differences in the position of the interface (ligament volume is chosen here) between different grid sizes are shown. The relative differences of the interface position between succeeding grid sizes are measured since the exact solution for this problem is not known. In the VOF-CSF method, the relative

differences increase with mesh refinement, which indicates the failure of the grid convergence. The relative differences decrease in both the CLSVOF-CSF and CLSVOF-PBM methods, and the PBM differences appear to decrease faster.

Table 5.2 Relative Differences of Ligament Volume between Consecutively Reduced Grid Sizes at One Time Instant

$\Delta x \times \Delta y$ (mm×mm)	VOF-CSF	CLSVOF-CSF	CLSVOF-PBM
0.06×0.06	N/A	N/A	N/A
0.03×0.03	0.1175	0.0841	0.1069
0.015×0.015	0.2048	0.0826	0.0716
0.0075×0.0075	0.2552	0.0741	0.0355

5.4.2 Tests for Two-Phase Interfacial Flows

In free surface flows, only a single phase is considered. The effect caused by the sharp variations of the physical properties is not taken into account. In the following tests both gas and liquid phases are considered. Constant properties of air and water are chosen unless otherwise specified: g=-9.8 m/s^2, s =0.0728 kg/s^2, r_l=1000 kg/m^3, r_g=1.226 kg/m^3, m_l=1.137×10^{-3} kg/ms and m_g=1.78×10^{-5} kg/ms.

5.4.2.1 Spurious Currents Test

Consider a two-dimensional computational domain of 2.0 mm×2.0 mm, a circular liquid droplet centered at (1.0 mm, 1.0 mm) with a radius of 0.5 mm. In the absence of gravity and initial velocity, the relevant dimensionless parameters are the Ohnesorge number $Oh = m/(s r D)^{1/2}$, density ratio r_l / r_g and viscosity ratio m_l / m_g. It has been found in the literature that the spurious currents increase with density ratio and decrease with the Ohnesorge number. However, in the reported spurious current tests

[55, 57], uniform density and viscosity are often used. The effect of these physical property jumps on the generation of the spurious currents is overlooked. In [57], the tests are performed only for the cases with a relatively large Ohnesorge number of 2.37, which is a relative stable situation. In this study, much more demanding cases with much smaller Ohnesorge number (3.71×10^{-3}) and larger density ratios (up to 1000) are considered. For comparison purposes, the CSF method is included again in the computation with the interface tracked both by the CLSVOF method.

Figure 5.12 shows the velocity vector field at 0.95 ms for various cases with different density ratios obtained by the CSF and PBM methods. As expected, strong spurious currents are apparent at the interface for the CSF method. As for the PBM method, velocity vectors are almost invisible even in the case with a large density ratio, indicating the absence of the fluid flow. Moreover, as shown in the figure, the density ratio remarkably affects the magnitude of the spurious currents in the CSF method but has little effect on the PBM method. This is dearly evident in Figure 5.13 which shows the maximum velocity magnitude versus time. Obviously, the increase of the density ratio significantly strengthens the spurious currents in the CSF method. This is because of the continuum treatment of the surface tension force. On a fixed orthogonal grid, the mass contained in a given cell, which is proportional to the density, is to be accelerated by the body force. In the transition region, the body force does not vary at the same rate as the density. While the density approaches a small value (e.g., on the gas side) near the interface, the body force may still maintain a relatively large value. This leads to an increase in flow acceleration and consequently the formation of strong spurious currents

in the lower density phase. This problem is eliminated in the PBM method, where the surface tension effect is treated as a pressure jump condition which is located exactly at the interface without smoothing.

Pressure distributions for cases with a density ratio of 1 are shown in Figure 5.14. For the CSF method, the pressure profile has been smeared out with an obvious transition region across the interface. The non-zero pressure gradients in the transition region will consequently drive flows even with uniform density. As for the PBM method, the sharp pressure jump is preserved. The pressure is uniformly distributed in each individual phase where pressure gradients are approximately zero, and the surface tension forces are exactly balanced by the pressure differences across the interface. As a result, spurious currents are greatly suppressed.

The spatial resolution effect is investigated by performing the computations on three consecutively reduced grids. Maximum velocity magnitude versus time plot for different mesh sizes is shown in Figure 5.15. The magnitudes of the spurious currents increase with time in the CSF method, and mesh refinement enhances rather than reduces the spurious currents. As for the cases with the PBM method, it can be seen that the magnitude does not increase with time but tends to fluctuate or reach to zero after a period of time. At the earlier stage of the computations, the magnitudes of the spurious currents vary with mesh refinement randomly, and eventually the finer the mesh size is, the sooner the magnitude approaches zero.

5.4.2.2 A Falling Drop in Air

In this section, a water droplet falling in air is simulated to test the dynamic performance of the PBM algorithm for two-phase interfacial flows. The same initial configuration and computational domain as in the free surface flow test are used. Although the results obtained from the CSF and PBM methods are in close agreement when treated as a free surface flow problem (refer to Figure 5.8), the accuracy of the CSF method in the two-phase flow model deteriorates seriously as shown in Figure 5.16. It can be seen from the figure that the droplet does not maintain a spherical shape during its fall, and the interface is not smooth but appears to be slightly wavy throughout due to the existence of spurious currents. Figure 5.17 shows the velocity fields for the two different methods. It is clear that the CSF method produces strong irregular and chaotic flows in the gas phase near the interface, whereas the PBM method generates a smooth and continuous flow field in the whole domain.

In the free surface flow mode, where the velocity and pressure vanish as the density approaches zero, the dynamic effect of the gas phase is neglected. In the two-phase interfacial flow mode, both gas and liquid phases are considered. The spurious currents are particularly severe on the gas side of the transition region, which further propagate into the adjacent gas region. Under these currents, the interface may be distorted and the computation fails especially when the surface tension force is dominant.

The superiority of the PBM method over the CSF model is apparent in this dynamic test. To further investigate the accuracy and applicability of the PBM method

for two-phase interfacial problems, the motion of a series of air bubbles with different diameters is tested.

5.4.2.3 Rising Bubbles in Water

Air bubbles rising in water are good examples for two-phase flow problems, where surface tension and viscosity are coupled with buoyancy. Six tests were performed with the bubble diameters ranging from 1.5 mm to 48 mm. For all cases, a computational grid of 35×175 is used on an axisymmetric domain with the initial bubble radius of eight cells; therefore, the larger the bubble size the coarser the grid. Solid wall boundary conditions are applied at the side and bottom, and an open boundary condition is imposed at the top with a constant atmospheric pressure.

The simulation results are shown in Figure 5.18. In the ***Eo-Mo-diagram*** of Clift ***et al***. [1], these cases are aligned on a line of constant Morton number $Mo = 10^{-10.37}$ where the bubble shapes change from "spherical" to "elliptical" and "spherical-cap". The shapes are reasonably predicted in the present numerical simulations, except for the last case where bubble collapse occurred due to the large bubble size.

The terminal velocity versus bubble diameter plot (without the last case) is given in Figure 5.19. Comparison is made with the experimental correlation obtained in [1], which is given by:

$$u_T = \sqrt{2.14s / r_l d_e + 0.505 g d_e} \tag{5-29}$$

It can be seen from the figure that the rise velocities for most cases are comparable to the experimental data. However, in the first case with the diameter of 1.5 mm, the rise velocity is much lower than the experimental result. This problem has

always troubled CFD researchers when simulating small size bubbles [69]. A possible explanation is that initial shape deformation is inevitable after the bubble is released in the experimental measurement, which may cause an initial velocity of a certain non-zero magnitude. In the numerical simulation, no initial shape deformation occurs for small size bubbles when the bubble is prescribed a spherical initial shape.

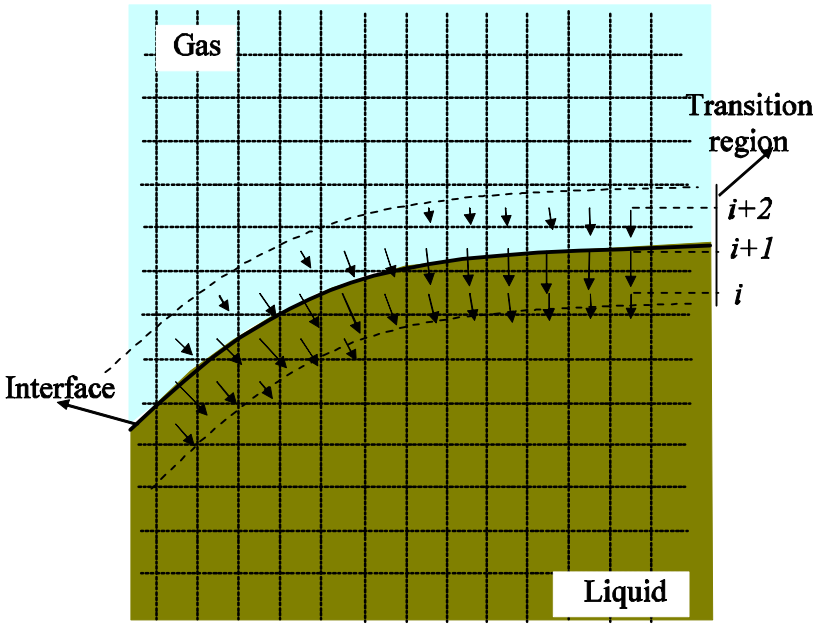

(a)

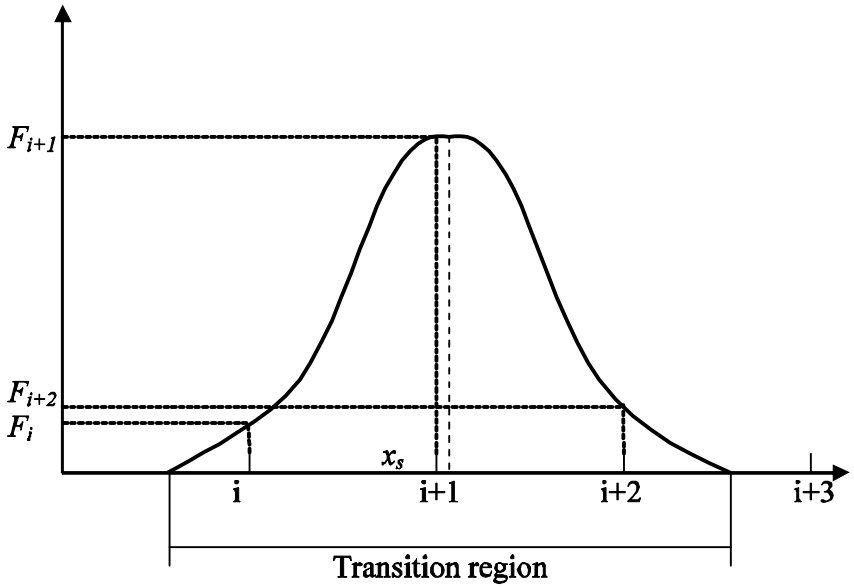

(b)

Figure 5.1 (a) Distribution of surface tension forces in the CSF model. (b)Variation of the magnitude of the body force across the transition region.

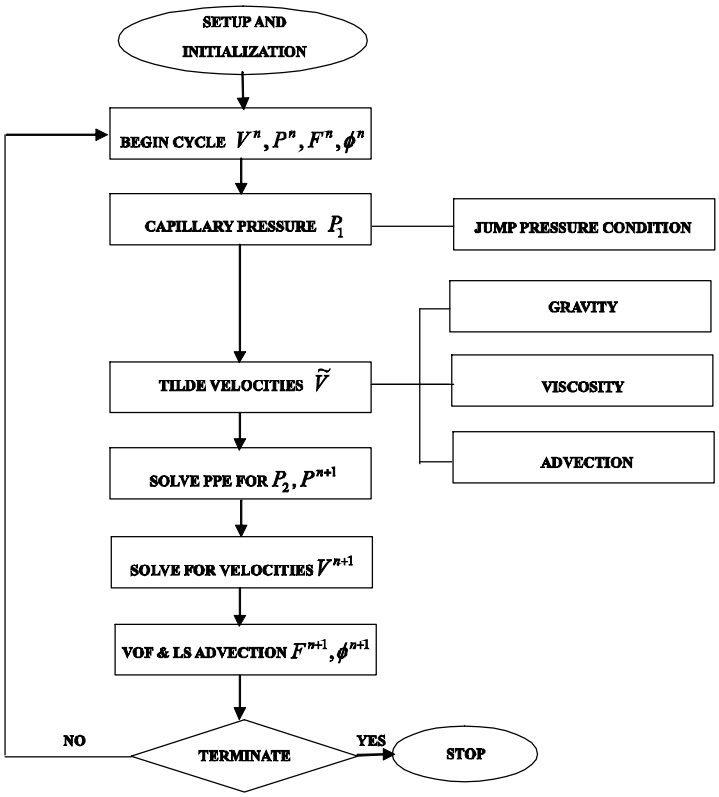

Figure 5.2 Flow chart for one computational cycle.

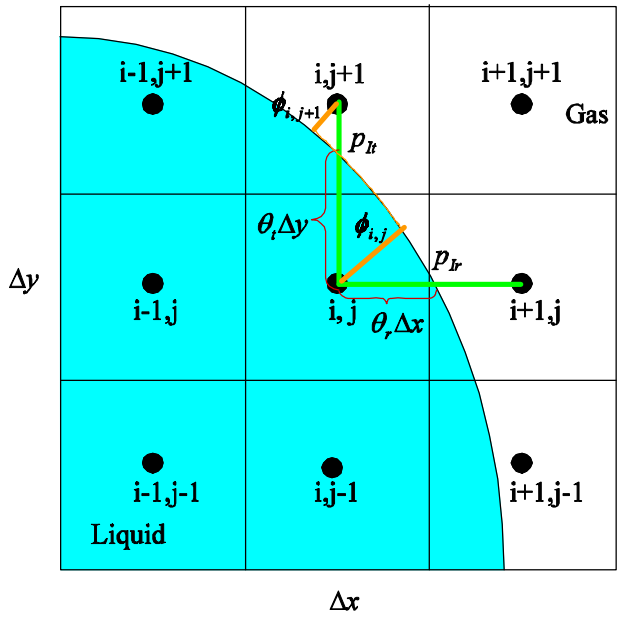

Figure 5.3 Discretization of pressure gradient at the interface and determination of the distance fraction θ.

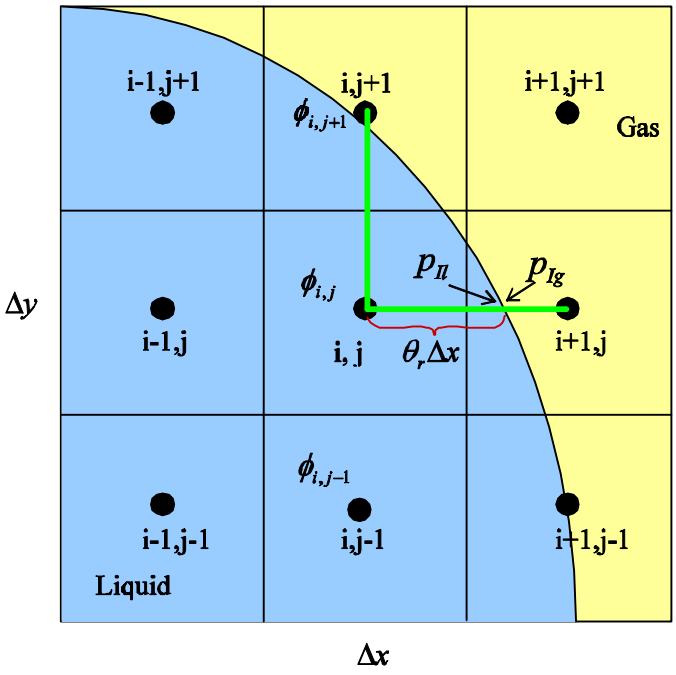

(a)

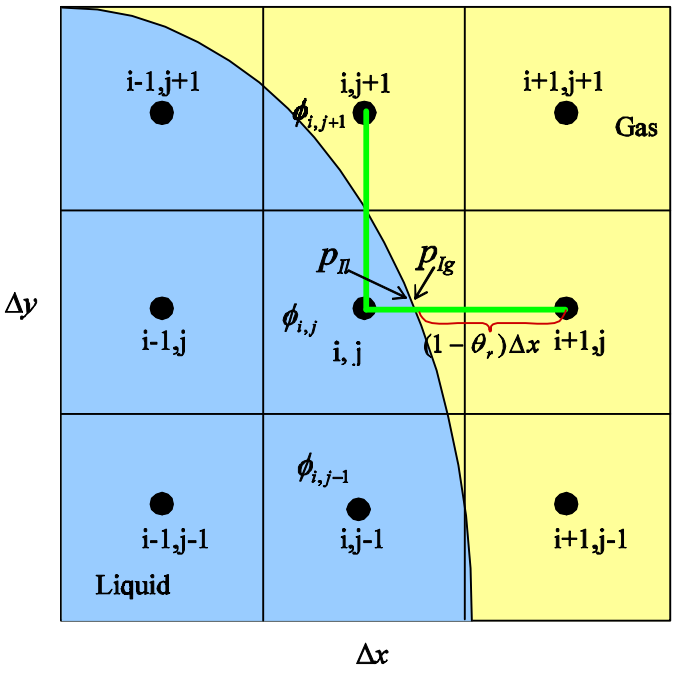

(b)

Figure 5.4 Gradient discretization across the interface: (a) $q_r > 0.5$; (b) $q_r < 0.5$.

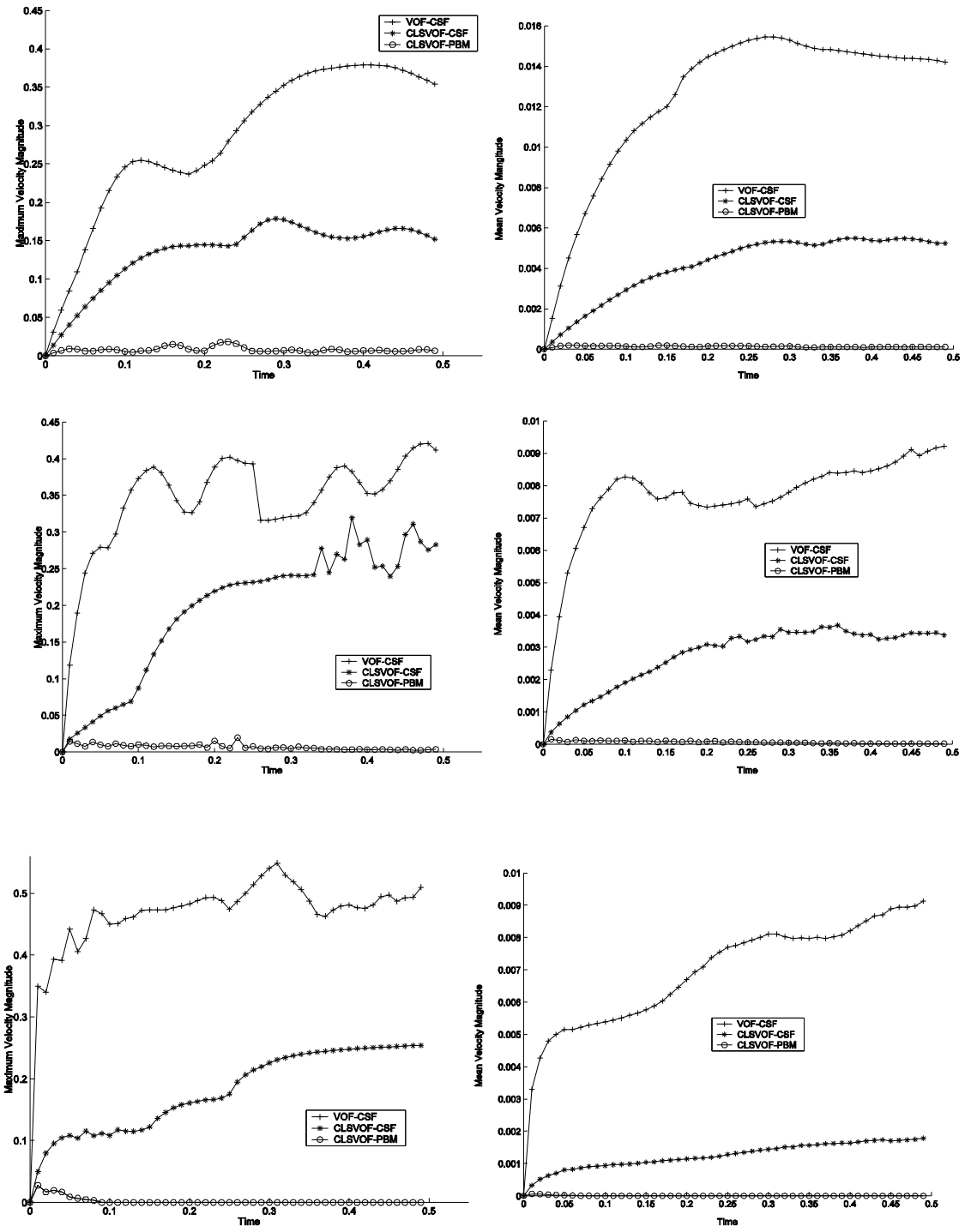

(Maximum velocity) (Mean velocity)

Figure 5.5 Maximum and mean velocity magnitudes versus time. Grid spacing at top: 0.04×0.04; middle: 0.02×0.02; bottom: 0.01×0.01.

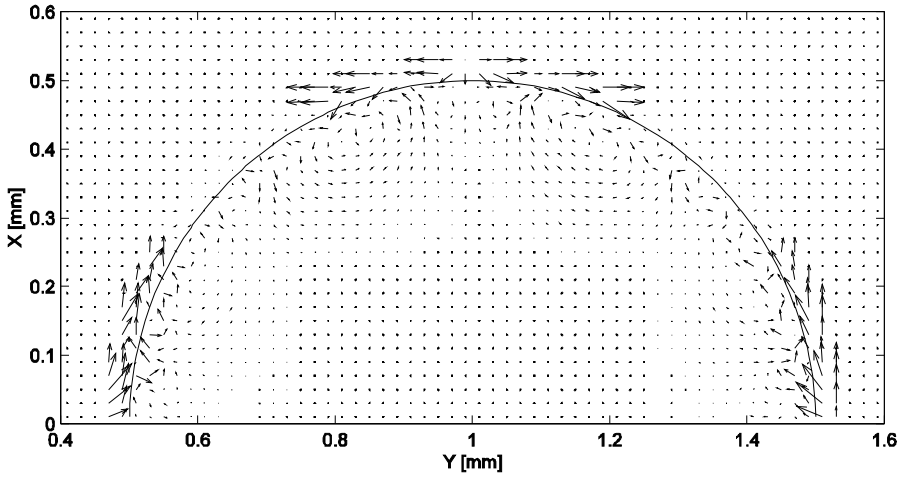

(a)

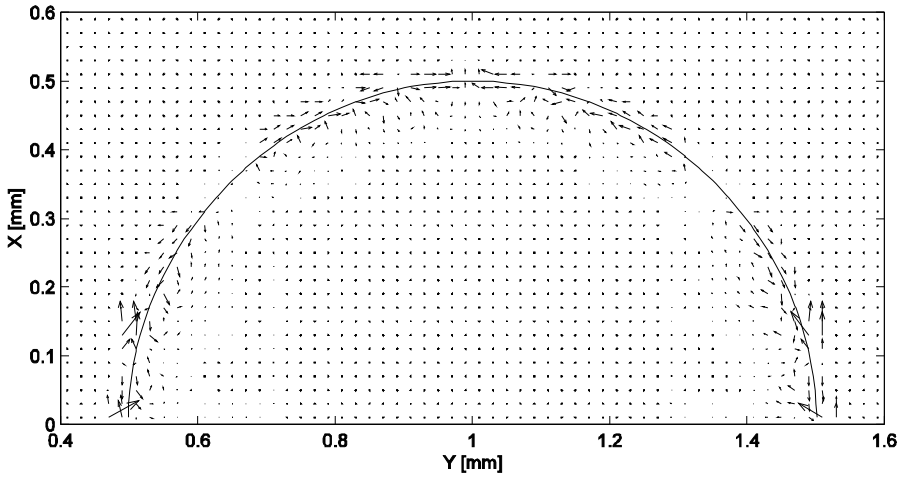

(b)

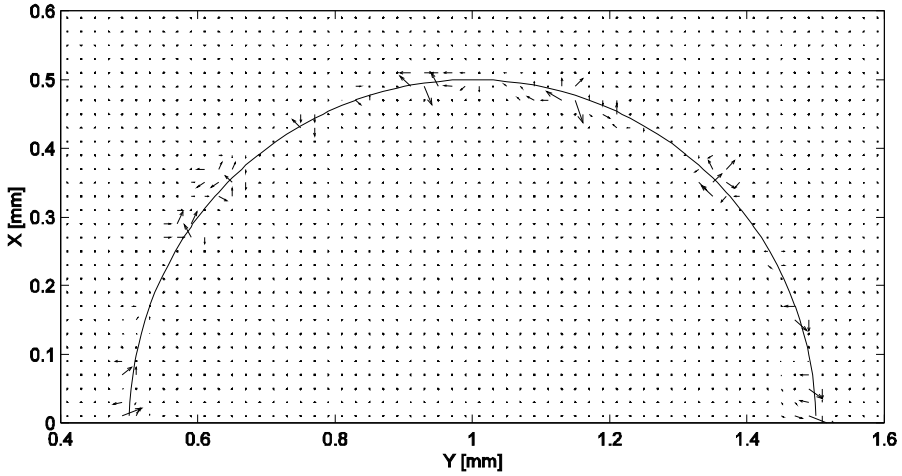

(c)

Figure 5.6 Velocity profiles for a stationary droplet at 0.5ms: (a) VOF-CSF; (b) CLSVOF-CSF; (c) CLSVOF-PBM. Grid: 0.02×0.02.

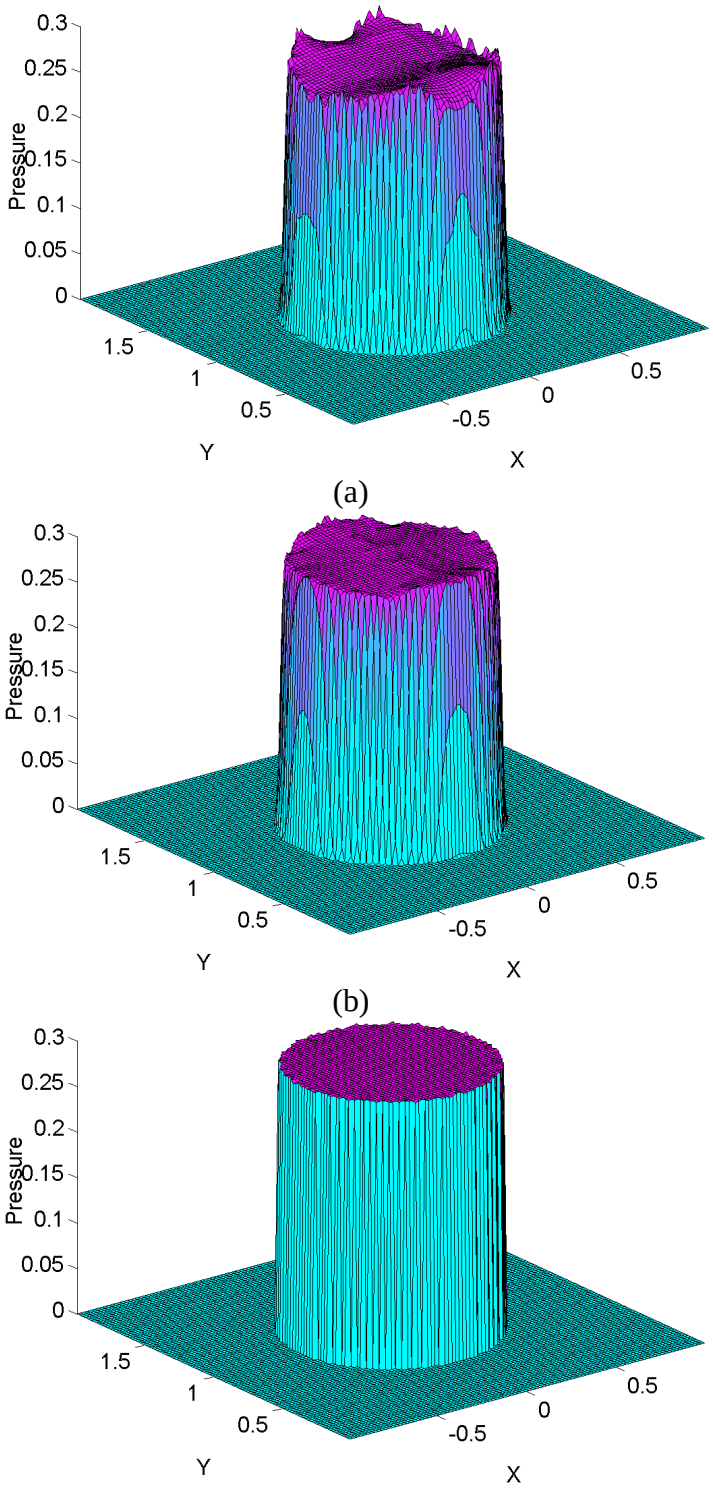

Figure 5.7 Pressure distribution for a static droplet at time 0.5ms: (a) VOF-CSF; (b) CLSVOF-CSF; (c) CLSVOF-PBM.

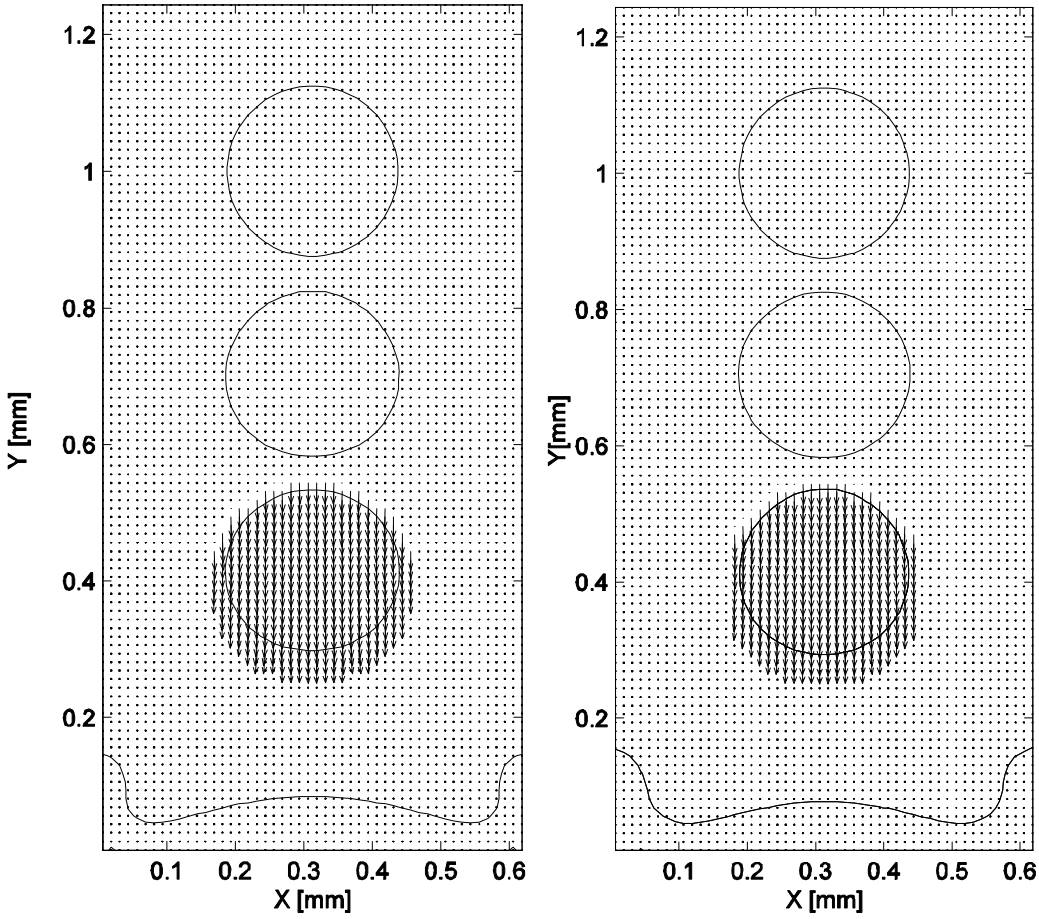

(a) CSF (b) PBM

Figure 5.8 Time sequence and velocity profiles of a falling droplet in air, CLSVOF used in both cases.

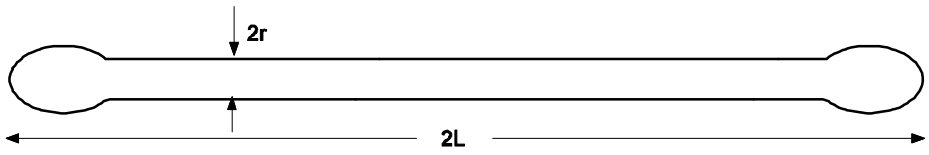

Figure 5.9 Schematic representation of an elongated liquid ligament.

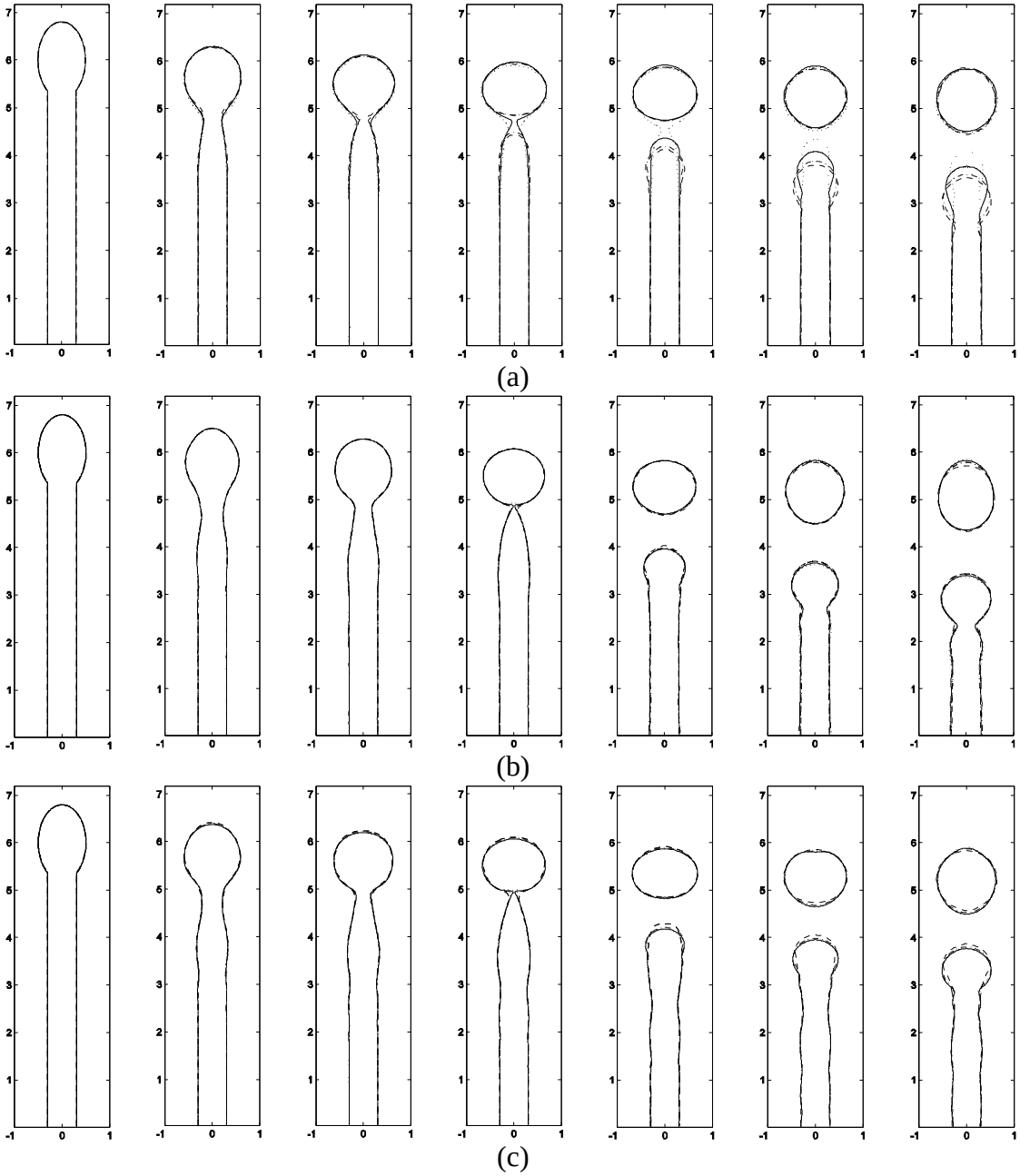

Figure 5.10 Breakup sequence of an elongated liquid ligament: (a)VOF-CSF; (b) CLSVOF-CSF; (c) CLSVOF-PBM. Dash: 0.06×0.06; dash-dot: 0.03×0.03; solid: 0.015×0.015; dot: 0.0075×0.0075.

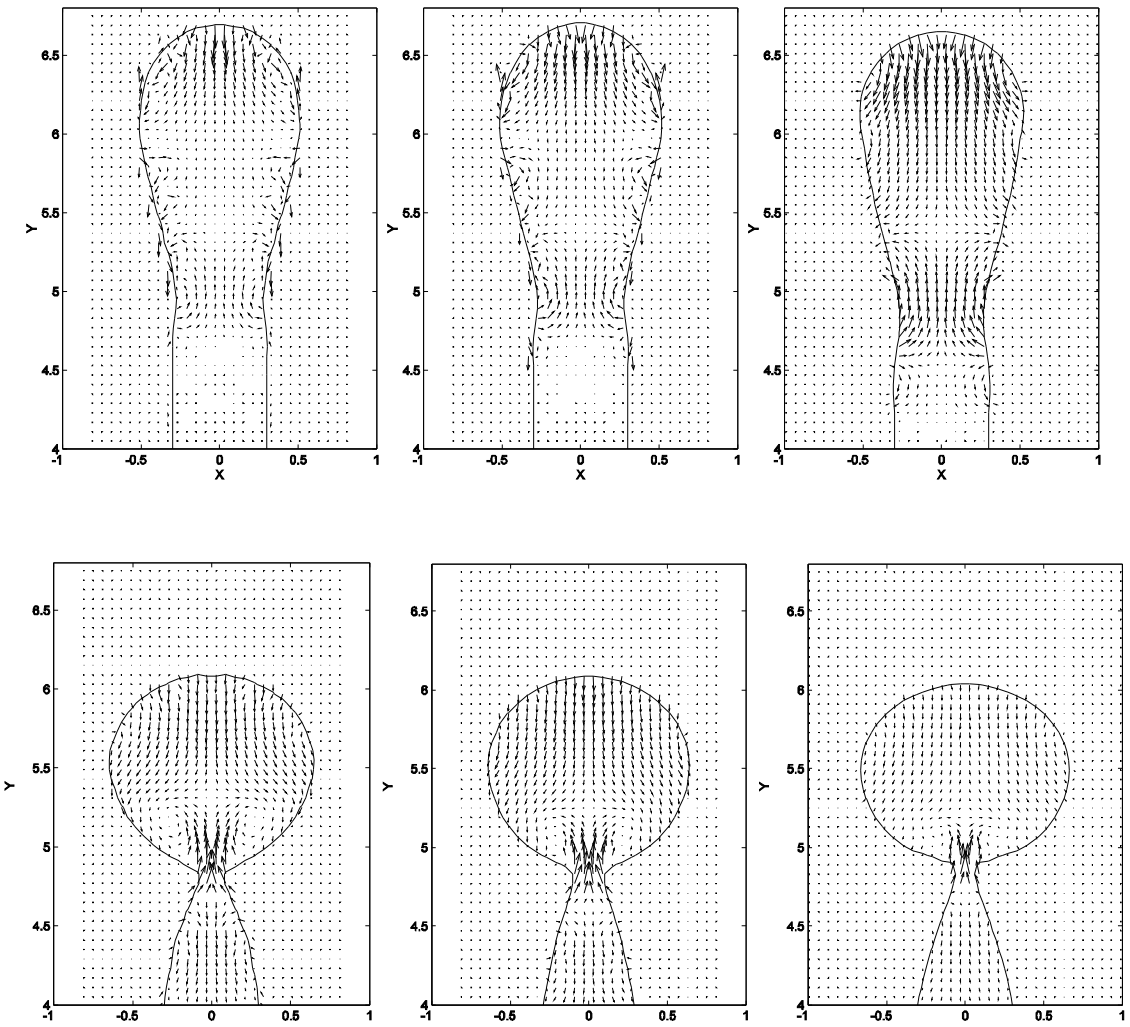

Figure 5.11 Velocity profiles of an elongated ligament for different methods. Top row: earlier stage of the relaxation process; bottom row: immediately prior to the pinch-off occurrence.

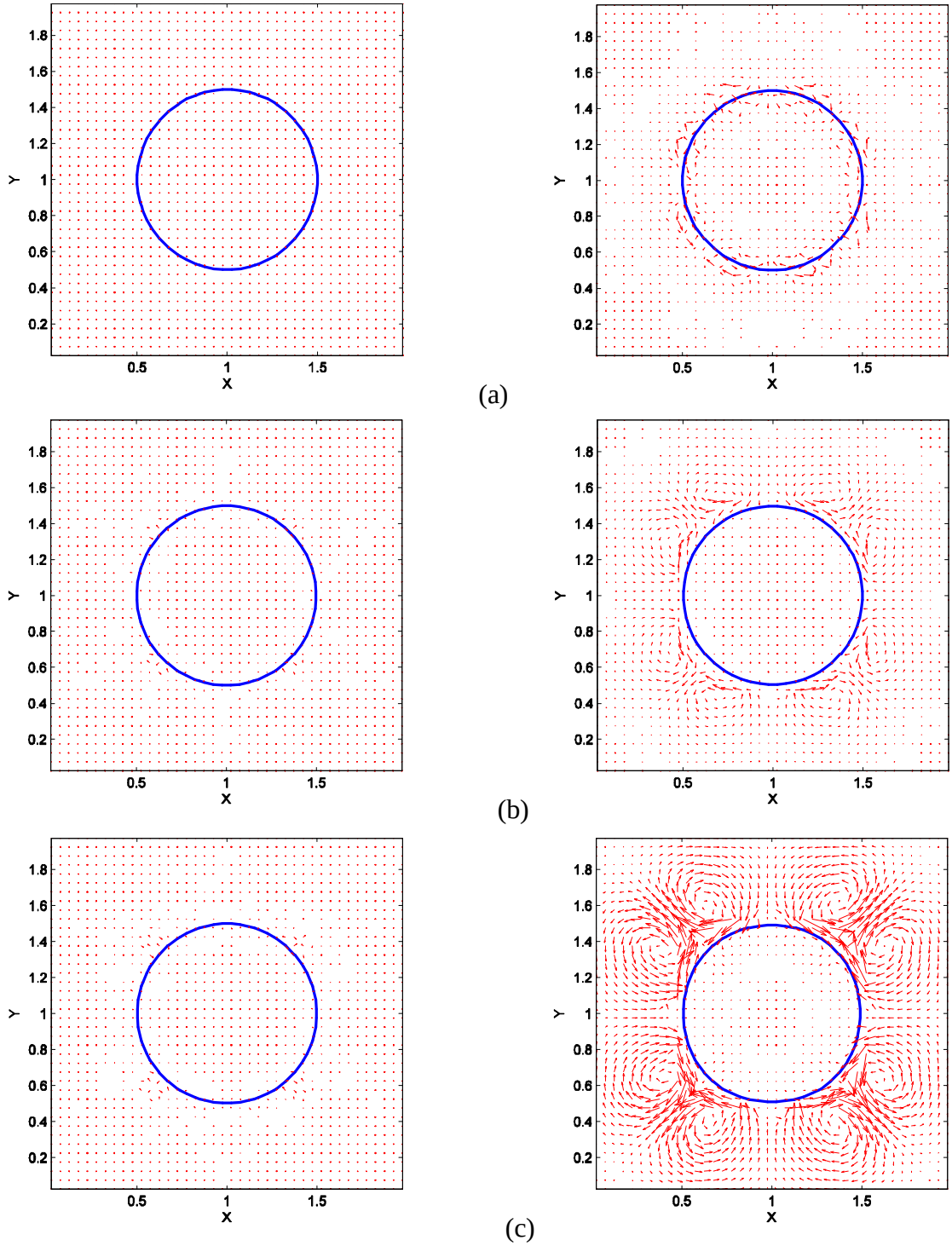

Figure 5.12 Velocity vector field for cases with different density ratios (PBM on the left, CSF on the right): (a) r_l / r_g =1; (b) r_l / r_g =100; (c) r_l / r_g =1000.

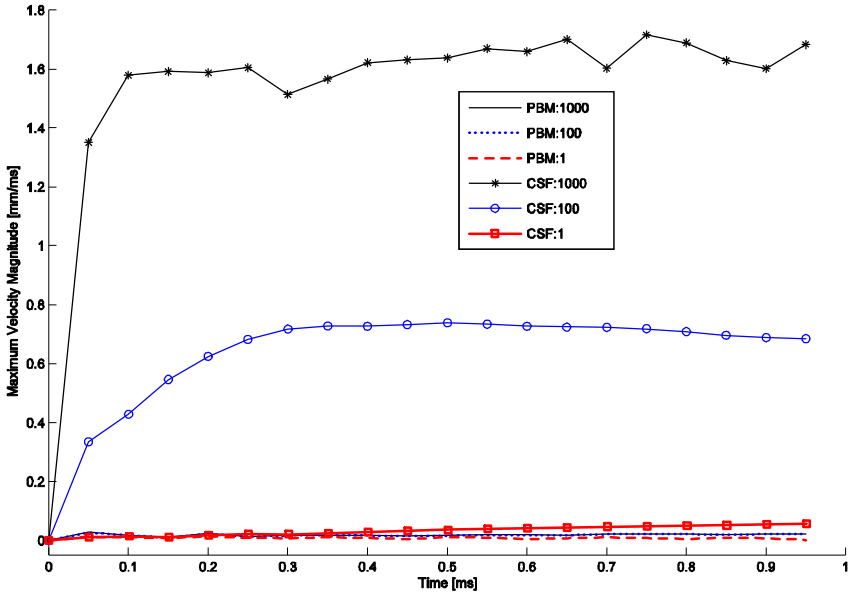

Figure 5.13 Maximum velocity magnitude versus time for different density ratios.

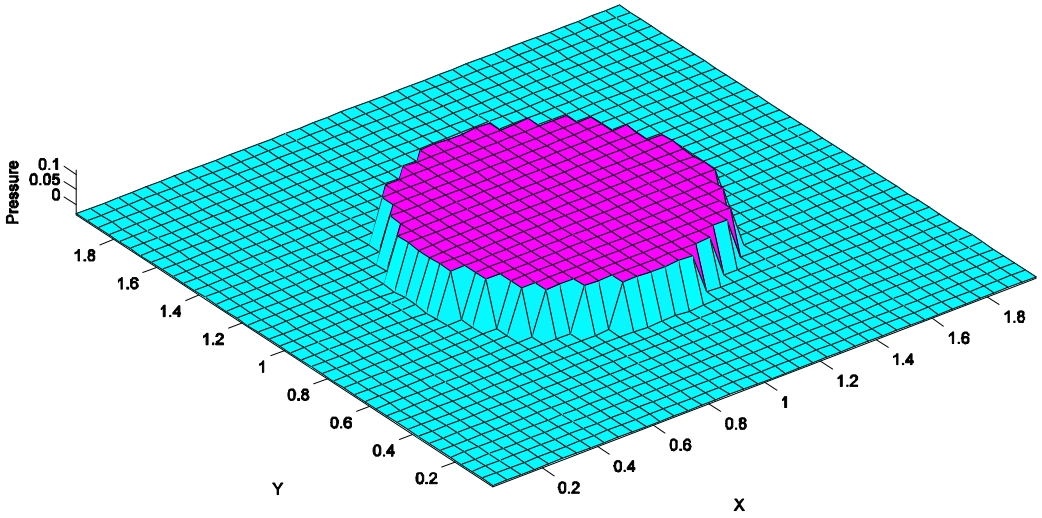

(a)

Figure 5.14 Pressure distribution: (a) PBM method; (b) CSF method.

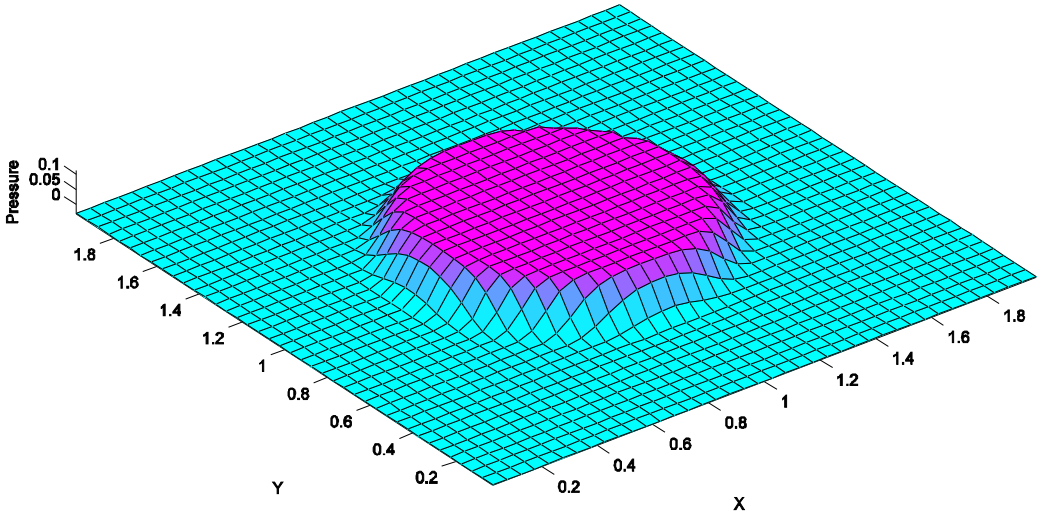

(b)

Figure 5.14 (continued)

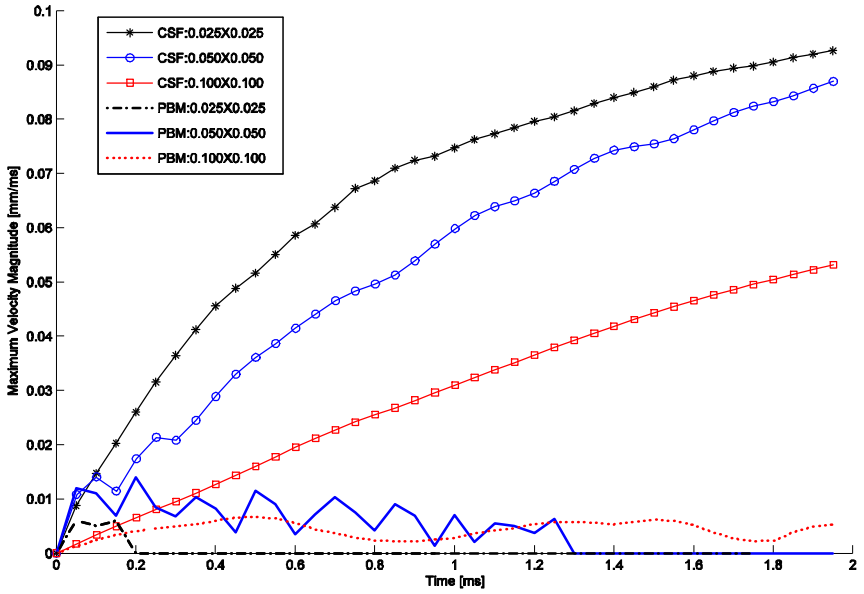

Figure 5.15 Maximum velocity magnitudes versus time for different mesh sizes.

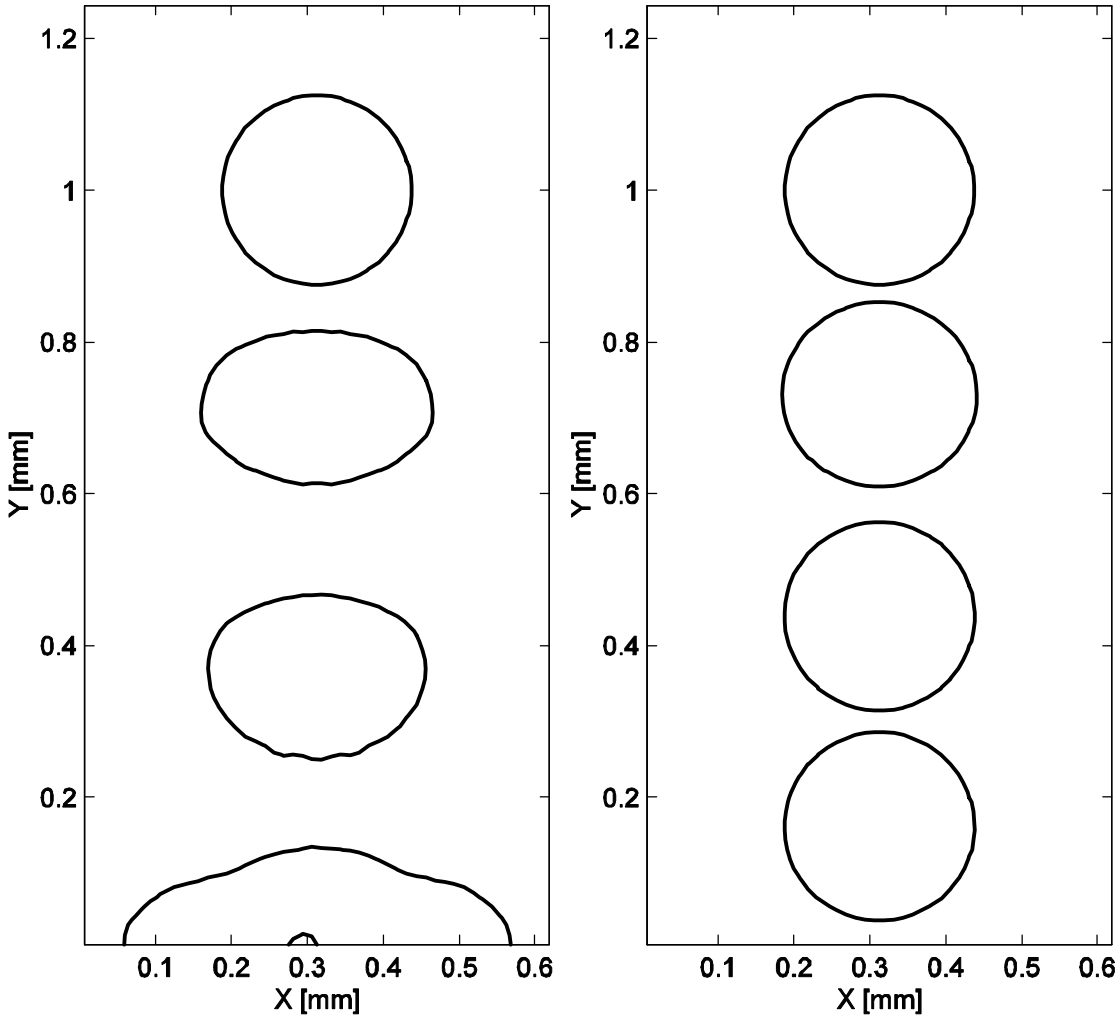

Figure 5.16 Time evolution of drop shapes for different methods: (a) CSF; (b) PBM.

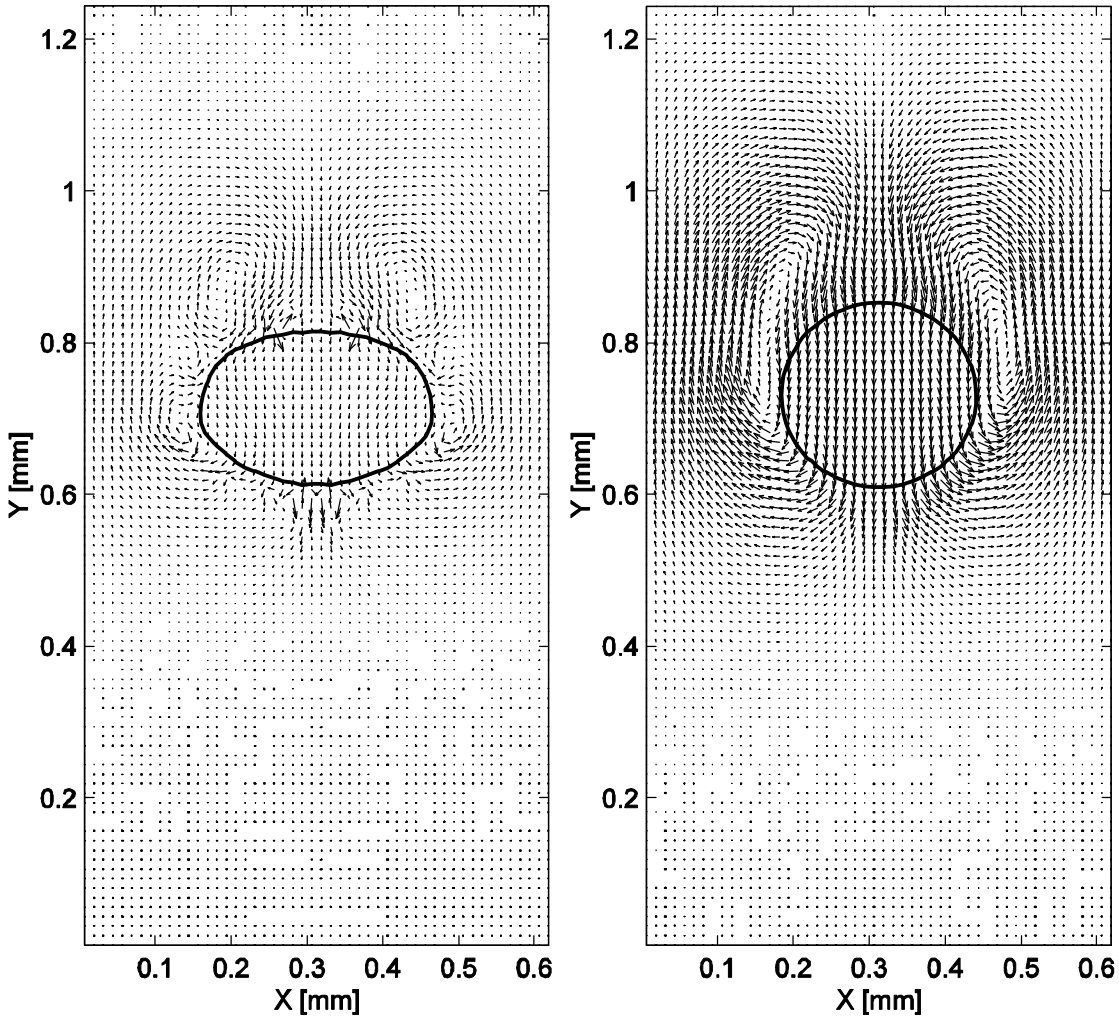

Figure 5.17 Velocity profiles of a falling drop at one time instant: (a) CSF; (b) PBM.

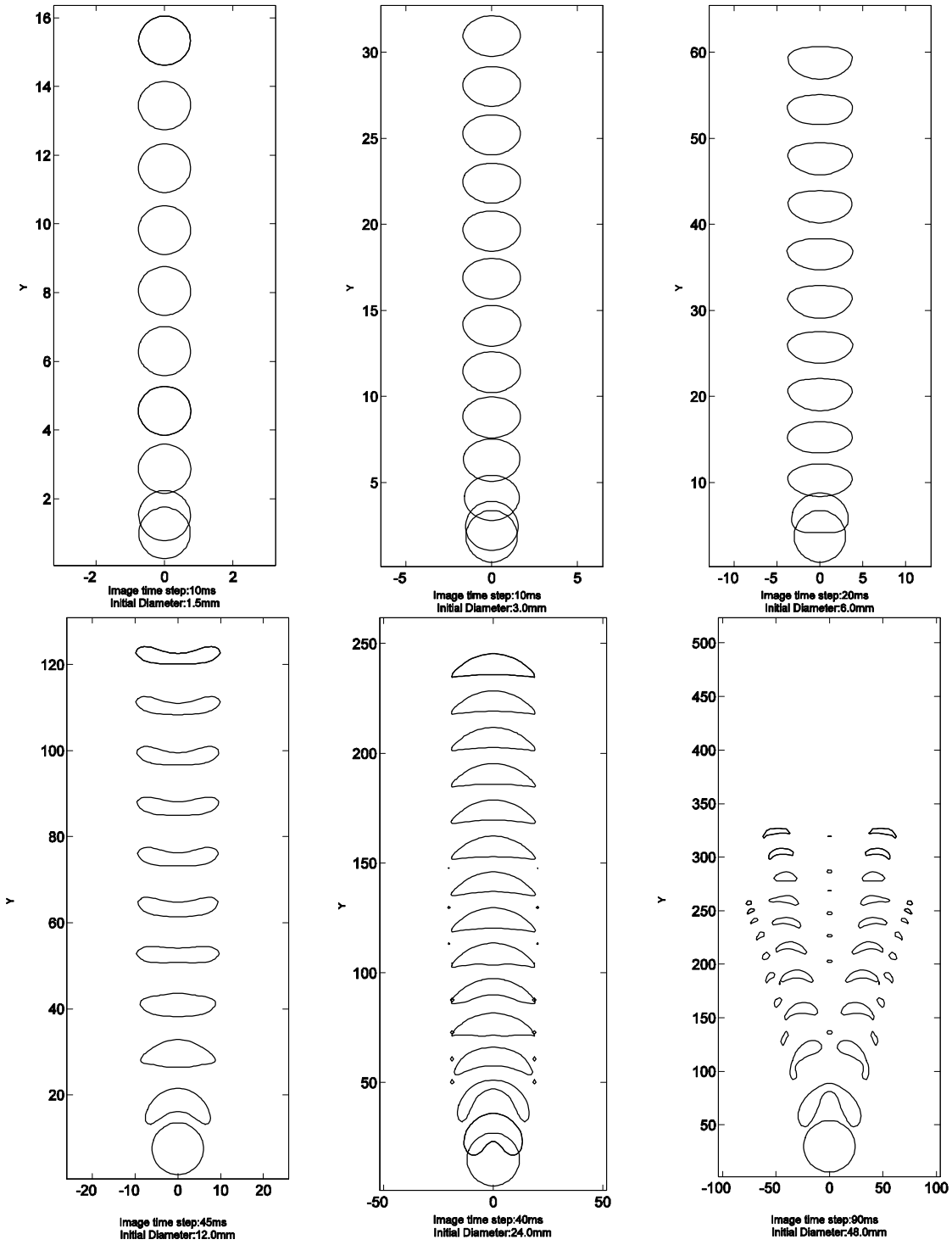

Figure 5.18 Air bubbles rising in water with different diameters.

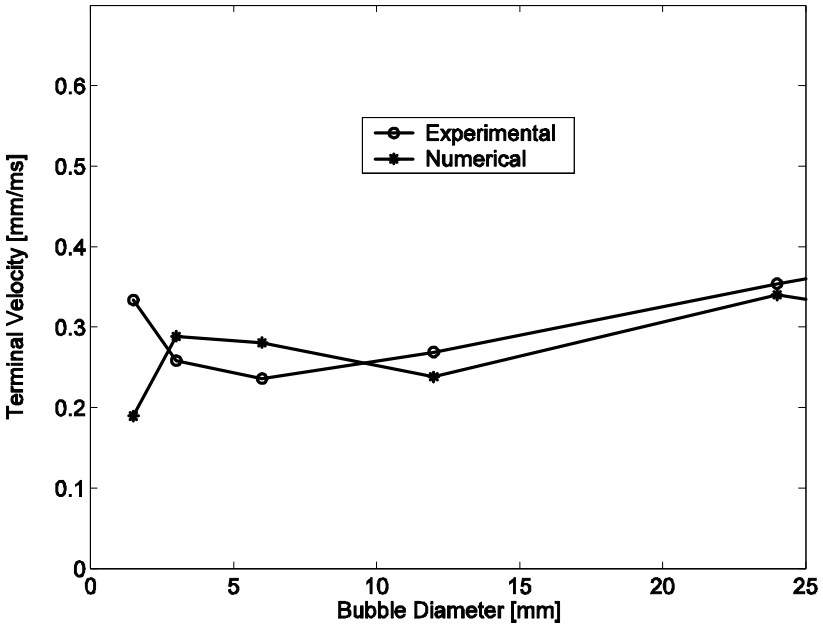

Figure 5.19 Numerical and experimental rise velocities versus bubble diameter.

CHAPTER 6

APPLICATIONS

In this chapter, the CLSVOF and PBM algorithms are applied to three different studies of free surface and two-phase interfacial flows. The accuracy of these algorithms is further confirmed. The versatility and robustness of the computer code are verified.

First, the pinch-off mechanism of a pendant droplet is investigated using the CLSVOF scheme for free surface tracking, and the CSF method for surface tension modeling. The VOF method, in conjunction with the CSF model, is also adopted for comparison purposes. The superiority of the CLSVOF scheme over the VOF method is demonstrated. As a capillarity-driven flow problem, the relaxation process of an elongated liquid ligament is also studied. Finally, the behavior of a single gas bubble rising in a narrow vertical tube is simulated. This serves as an example for two-phase interfacial flow problems. The interface of the bubble is tracked using the CLSVOF scheme and surface tension is modeled by the PBM method.

The numerical results are in good agreement with the experimental and theoretical studies reported in the literature.

6.1 Pinch-off Mechanism of a Pendant Droplet

6.1.1 Introduction

Deformation and breakup of a pendant droplet has been an intensive research topic for more than one hundred years. There are many industrial applications involving a fluid flow with free surfaces that cause a pinch-off phenomenon. Ink jet printing and gas spraying of an engine are such examples. Many studies have been experimentally and numerically carried out on the deformation and breakup of a pendant droplet. A detailed literature review can be found in [70].

Although there have been many studies on liquid pendant droplets, sufficient explanation of the breakup mechanism is lacking in the literature. Most studies do not give information on the flows such as velocity profiles and the pressure distribution that are of importance in the evolution of a pendant droplet in the neighborhood of the breakup point. The main objective of this work is to examine the breakup mechanism of a pendant droplet. Comprehensive study of the breakup mechanism of the pendant droplet is conducted in [70]. The focus of the present study is on the evaluation of the accuracy of the CLSVOF and VOF methods.

6.1.2 Initial Configuration and Boundary Conditions

The schematic of the pendant drop forming from a vertical capillary tube is shown in Figure 6.1. A capillary tube with an inner radius of 1.0 mm and outer radius of 1.6 mm is placed at the top of the domain, and the length is set to two times the outer radius. Water with constant physical properties evaluated at 20 ^{o}C is used as the working fluid. The computation is carried out on an axisymmetric domain, and the

initial configuration of the free surface is flat across the whole front tube surface as shown in Figure 6.2.

At the inner tube wall, a non-slip boundary condition is applied, and a "wet" boundary condition is imposed at the front of the tube surface:

$$F(r,z,t)=1.0,\ \text{at}\ \frac{r}{R}=1,\ \frac{z}{R}=0 \tag{6-1}$$

The flow is initially at rest and a fully developed parabolic flow enters the tube:

$$v_r=0,\ v_z=2\frac{Q}{pR_i^2}[1-(\frac{r}{R_i})^2] \tag{6-2}$$

where Q is the liquid flow rate and Q/pR_i^2 is the average velocity. The boundary conditions are set according to the experimental and numerical studies [71, 72] in order to make a comparison of the results.

Three non-dimensional characteristic values are defined [72] to compare with the results of the present study: the relative limiting lengths of the primary droplet to the outer radius of the capillary tube, l_d/R, L_d/R, and the volume of the drop, V/R^3 (refer to Figure 6.1).

6.1.3 Results and Discussion

In order to make a comparison, the simulation is performed using both the CLSVOF and VOF methods for the free surface tracking, and the CSF method for surface tension modeling.

Figures 6.3 and 6.4 show the time sequence of the evolution of a pendant droplet using the VOF-PLIC and the CLSVOF schemes, respectively. Experimental

measurement [71] shows that the primary droplet is spherical shape (see Figure 6.5), but Figure 6.3 (l) shows that the droplet is elongated in z-direction and is more like an ellipse than a sphere. The shape of the droplet reported in [72] is also elliptical. As for the CLSVOF scheme, a more spherical-shaped droplet is produced as shown in Figure 6.4(l). Moreover, after the primary droplet is detached, the top of the droplet is immediately flattened due to the high local pressure associated with the large curvature as shown in Figure 6.5 (k-m). The CLSVOF method apparently predicts the shape flattening as shown in Figure 6.4 (m-o), while in the VOF-PLIC scheme, the flattening cannot be found. When the grid spacing is reduced by half for the grid refinement test, a water jet rather than a droplet is produced with the VOF method, which implies that grid convergence fails. As for the CLSVOF scheme, results obtained on different grid sizes are in very close agreement and no spatial convergence problem is encountered [70]. This indicates that the CLSVOF method is more accurate than the VOF-PLIC method, and hence the superiority of the CLSVOF method is demonstrated.

The characteristic values of the water droplet with the CLSVOF scheme are compared with Zhang's VOF and experimental measurement over wide range of liquid flow rate in Figure 6.6. For the CLSVOF case, the uniform inlet velocity profile is also simulated at liquid flow rate of 10 mL/min. It is found that the numerical results of the CLSVOF scheme are in good agreement with the experimental measurements especially at liquid flow rates over 15 mL/min. This is further validation of the accuracy of the CLSVOF method.

The breakup mechanism is detailed in [70] and will not be repeated here. Parametric studies have also been done on the effect of inlet velocity profile, viscosity, gravity, and surface tension coefficient. The inlet velocity profile has little effect on the breakup mechanism. Viscosity is found to have negligible impact on the breakup mechanism. Gravitational acceleration and surface tension coefficient control the time of breakup. Formation of successive droplets has been studied to see the effects of the initial conditions on the droplets. The pinch-off time is affected by the initial conditions adopted in the present study but effects on the geometric properties are negligible.

6.2 Relaxation of an Elongated Liquid Ligament

6.2.1 Introduction

The deformation and breakup of a liquid drop has been of considerable interest in fluid dynamics. It occurs in processes such as raindrop formation, inkjet printing and various engineering applications involving sprays. The objective of the present study is to examine, via numerical simulations, the breakup mechanism of a moderately elongated liquid ligament in air. It is motivated by several recently published studies [4, 6, 7, 73]. The first one by Stone and coworkers [6, 7] involves both experimental and computational studies on the breakup behavior of highly elongated droplets in a neutrally buoyant quiescent suspending fluid. A computer-controlled four-roll mill is used to elongate a liquid drop in another immiscible suspending liquid. The elongated liquid drop undergoes a complicated, time-dependent relaxation process after the flow is abruptly stopped. It either returns to a single sphere or breaks into smaller drops. It was observed that breakup occurs due to deterministic flows established by capillary forces

associated with curvature variations along the interface, rather than by the classical capillary-wave instability. The observed motion consists of a relatively rapid bulging of the end of the drop followed by break-off of the bulbous end from the central portion of the drop. Detailed numerical calculations using the boundary-integral method are presented which elucidate the end-pinching mechanism. It is noted that the relaxation and breakup dynamics are completely determined by the viscosity ratio and the initial droplet shape. A critical elongation ratio exists beyond which ligament break up will eventually occur.

The next study, by Qian and Law [4], is an experimental investigation of binary droplet collision dynamics with emphasis on the transition between different collision outcomes. A long stretched ligament is produced as the two main droplet masses move away from each other after their collision. The ligament will either contract to form a single droplet or further break up into satellite droplets. It has been demonstrated that satellite droplet production for high-inertia collisions is the consequence of ligament pinching as observed in the study by Stone and coworkers [6,7].

Recently, the work of Stone and coworkers [6,7] was extended by Ha and Leal [73], whose main focus is on the effect of the strain rate that characterizes the drop stretching process. Existence of the critical elongation ratio for drop breakup is confirmed. However, it is shown that the relaxation process, for the same elongation ratio, depends on the strain rate at which the drop elongates. Even more surprisingly, ‘re-stabilization’ occurs where further increase of the elongation ratio beyond the critical value would lead to cessation of pinch-off breakup.

A key difference between the above two groups of studies is in the suspending fluid, which has a significant effect on the dynamics of the flow. The neutrally buoyant environment provided by the suspending liquid in Leal *et al.'s* study justifies the use of a quasi-steady Stokes flow model. However, the model is not applicable in the case of a gas phase suspending fluid with relatively higher Reynolds number and stronger surface tension force, and consequently the boundary integral method cannot be used. There have been very few experimental studies reported in the literature on the breakup behavior of a free liquid ligament in air. This perhaps is a reflection on the technical difficulties due to the presence of gravity whose effect cannot be eliminated as in the case of a neutrally buoyant suspending fluid in the liquid-in-liquid studies such as the experiment performed by the Leal *et al.*.

The focus of the present study is on the relaxation dynamics of a liquid ligament in air. A numerical study that takes into consideration the inertia and the transient effects of the flow is performed. The unsteady Navier-Stokes equations are solved along with the free surface tracked by the CLSVOF method and the surface tension force simulated by the CSF model.

6.2.2 Results and Discussion

A schematic of the initial configuration of an elongated ligament used in the numerical simulation is shown in Figure 6.7. The choice of the initial end shape is based on the findings of Stone *et al.* [6,7]. Water with physical properties evaluated at standard conditions is used and the initial length and radius of the ligament are 13.6 mm and 0.3 mm respectively. In order to conserve computational resources, only half of the

ligament is modeled with computations conducted on an axisymmetric domain of dimensions 7.0 mm×1.0 mm.

The following characteristic dimensional quantities are used to convert the governing equations, Eqs. (3-1), (3-2), into dimensionless form:

$$U_r = \frac{s}{m} \ , \ L_r = R_0 \ , \ t_r = \frac{mR_0}{s} \ , \ P_r = \frac{s}{R_0} .$$

yielding the dimensionless quantities:

$$u' = \frac{u}{U_r} \ , \ P' = \frac{P}{P_r} , \ t' = \frac{t}{t_r} \ , \ x' = \frac{x}{L_r} \ , \ y' = \frac{y}{L_r} .$$

Equations (3-1) and (3-2), in nondimensionalized form with the effect of gravity neglected, become:

$$\nabla \bullet u' = 0 \tag{6-3}$$

$$\frac{\partial u'}{\partial t'} + u' \bullet \nabla u' = Oh^2 \{ -\nabla P' + \nabla \bullet [(\nabla u') + (\nabla u')^T] \} + Oh^2 R_0{}^2 d(x) kn \tag{6-4}$$

where $Oh = (rn^2 / s R_0)^{1/2}$ is the Ohnesorge number which is defined as the dimensionless group obtained by dividing the square root of the Weber number by the Reynolds number. The Ohnesorge number describes the relative importance of inertial, surface tension and viscous forces in the ligament breakup process. The term $R_0{}^2 d(x) kn$ in Equation (6-4) relates to the geometry of the ligament. Thus, as demonstrated in the non-dimensional formulation, the parameters that control the relaxation dynamics of the ligament are the Ohnesorge number and the initial shape of the ligament.

The relaxation sequence leading to the break-up of an elongated liquid ligament is shown in Figure 6.8. The pressure distributions along the centerline are plotted in part (a) and the flow fields in the vicinity of the pinch off are presented in part (b). The ligament break-up shown in the figure appears to follow the "end-pinching" mechanism outlined in the studies [4,6,7,73] previously mentioned. The additional curvature at the rounded ends of the ligament, as compared to the central portion, generates a higher pressure because of surface tension. The pressure gradient drives the fluid away from the ends towards the midsection, resulting in the formation of a bulbous region at the tips. The presence of the bulb, leads to a negative curvature and consequently a minimum pressure somewhere between the bulbous end and the midsection, and sets up a local flow towards this minimum pressure point from both sides. The local flow on the midsection side creates a neck as a result of local mass reduction accompanying the flow. The formation of this neck leads to an increase in pressure due to the increase in curvature by the reduction of local ligament radius. This local peak in pressure causes further reduction of mass, leading to a further reduction in the radius of the neck. This generates an unstable situation resulting in further development of the neck and an eventual "end pinch off" of the bulbous region.

In general, the numerical results obtained in the present study are in agreement with the "end-pinching" mechanism with the exception of one notable difference, which perhaps holds the key as to why end pinching does not always occur. Upon closer examination of the flow field and the pressure distribution, it is found that a sharp pressure variation exists slightly upstream (away from the end) from the neck. This can

be clearly seen in the magnified view shown in Figure 6.9. Contrary to the end-pinching mechanism where the maximum pressure point is supposed to be located at the neck where the radius is minimum, the pressure is minimum there instead. The sharp pressure variation is due to the severe change in the geometry of the free surface where the lateral (longitudinal) curvature undergoes drastic changes from slightly convex to overly concave. Note that the surface tension force is proportional to the sum of the radial and lateral curvatures. The lateral curvature, which plays a minor role in most of the ligament regime, becomes a dominant component at the neck and consequently generates a sharp pressure variation there.

It is of interest to point out the appearance of a flow recirculation zone inside of the bulbous end. Again, contrary to the end-pinching mechanism, the flow does not originate from the neck, but instead, slightly upstream from the neck where the pressure is at a maximum. It penetrates the neck and collides with the reverse flow, resulting in the formation of the recirculation zone. This, as will be demonstrated in the later part of this study, plays a key role in controlling the fate of the ligament in the relaxation process.

In Stone *et al's* numerical study [7], it is mentioned that the flow and the subsequent breakup of ligaments are determined by the viscosity ratio and the elongation ratio. It is also concluded that the initial shape at the end of the ligament does not affect the end-pinching mechanism and it is the overall global geometry and the viscosity ratio that control end pinching. However, in the recent study by Ha and Leal [73], it was reported that with the same elongation and viscosity ratio, the

ligaments behave differently with different strain rates, which resulted in different initial ligament end shapes. The latter result appears to be in agreement with the findings of the present study. As shown in Figure 6-10, a more circular bulbous end enhances the likelihood of pinch off and at an accelerated pace. On the other hand, a more elliptical end shape tends to hinder the breakup process. With a 'pencil-head' end shape, it eventually contracts back to a single drop. This is in contradiction to the end-pinching theory. This is a flaw in the theory where the lateral curvature in the neck is not properly taken into account.

The relaxation sequence of a pencil-head ligament is shown in Figure 6.11. Note that, for illustration purposes, only the flow fields in the region enclosed by the dashed line are shown and the sequence is split into two columns. The reopening of the neck is clearly shown. Basically, the outcome of a relaxation process is controlled by the relative strength of the inward reverse flow from the bulb to the center and the outward flow towards the neck from the main body. A stronger outward flow would enhance end-pinching breakups by pushing away and consequently detaching the bulb. This is shown in Figure 6.8 where the overwhelming pressure gradient on the immediate left of the neck pushes away the bulb resulting in end-pinching breakup. On the other hand, a stronger reverse flow would push the fluid in the bulb inward through the neck, preventing pinch off at the neck. This is indeed the case with the pencil-head ligament shown in Figure 6.11. With a pointed end shape, the curvature at the end is larger, which results in a higher pressure and a stronger reverse flow to impinge on the outbound opposing flow.

The dimensionless form of the governing equations, i.e. Eqs. (6-3) and (6-4), indicates that the relaxation dynamics of the ligament are governed by the initial geometrical shape and the Ohnesorge number. This has been confirmed by a parametric study performed with varying fluid properties. It is found that, for a given initial ligament shape, variations of surface tension coefficient, viscosity and density will not affect the breakup process if the Ohnesorge number, *Oh*, is kept constant. However, the time scale, $t = mR_0/s$, will not be preserved.

The results for four cases with the Ohnesorge number ranging from 0.01 to 0.2 are shown in Figure 6.12. There exists a critical *Oh* value beyond which no pinch-off breakup is observed. In the current study, it is between 0.067~0.08. The critical Oh number is dependent on the initial ligament shape.

6.2.3 Conclusions

The time-dependent relaxation dynamics of a moderately elongated liquid ligament has been studied numerically using a CLSVOF method for tracking the free surface in conjunction with the CSF model for the surface tension calculation. The breakup mechanism has been examined and a flaw in the published "end-pinching" mechanism has been identified that enables an explanation of the "re-open" process of the neck. The relaxation dynamics of the ligament are governed by the initial shape and the Ohnesorge number. The end shape in particular plays a key role in the breakup process. A more circular bulbous end enhances the likelihood of pinch off and at an increased pace. The numerical simulations are in agreement with the experimental findings in the literature.

6.3 Motion of a Large-Sized Gas Bubble in a Narrow Vertical Tube

6.3.1 Introduction

Bubble-driven flows appear in various natural and industrial processes with a wide range of applications such as oil transportation, steam generation, cooling systems of nuclear power plants, propagation of sound in the ocean, cloud cavitations, *etc*. Numerous experimental and theoretical studies have been carried out during the past fifty years [1]. Due to the complex two-phase flow patterns associated with bubble behavior, some issues are still unresolved. Among these, bubble oscillations have attracted much attention in recent years due to the development of advanced measurement techniques and tools that provide more detailed information about the dynamics of bubble motion. Bubble oscillations are complicated phenomena that include the bubble-rising trajectory and shape instabilities as well as the associated velocity and pressure fluctuations. These oscillations further complicate bubble flow problems and cast doubt on the accuracy of the terminal velocity and the existence of a "steady state".

Much research work has been devoted to the study of bubble trajectory and shape oscillations with experimental methods [74-77]. For example, it has been found that large bubbles in an unbounded liquid do not move rectilinearly but follow a zigzag or spiral path instead. It is also generally believed that the vortex shedding at the wake of the bubble is responsible for these oscillations. Ellingsen and Risso [78] investigated the rise of a 2.5 mm diameter air bubble in water with high-speed video and LDA (laser Doppler anemometer). It was revealed that steady path oscillations, with the major axis

of the ellipsoidal shaped bubble in the direction of its velocity, developed in the absence of any shape oscillations. Di Marco *et al*. [79] studied a nitrogen bubble rising in a fluoroinert liquid (FC-72) and reported that the oscillations of the ascending velocity were well correlated with shape oscillations. Behavior of a single bubble in a surface tension dominant regime was investigated by Tomiyama *et al.* [80] both theoretically and experimentally with the focus on the terminal velocity. It was discovered that the initial shape deformation of a bubble has remarkable effects on the bubble trajectory, shape and velocity.

Most of the bubble oscillation studies were conducted in an infinite fluid environment where the wall effects of containers are negligible. Although bubble oscillations in a confined tube or pipe have practical significance, studies on the subject are relatively scarce. If a large bubble is confined in a narrow tube with a comparable cross-sectional diameter, the bubble will rise along the tube centerline, and path instabilities will not occur. The problem seems to become somewhat simpler without trajectory oscillations and is often neglected by researchers. Typically, for a large bubble in a narrow tube, a 'slug flow' will develop which is characterized by a rounded cap front, followed by a long main body surrounded by a falling annular liquid film [81]. Much of the work on slug flows has focused on the terminal velocity, steady shape and drag force. In a recent study [82], a universal correlation for the rise velocity of a long gas bubble in stagnant fluids contained in a vertical tube was obtained based on the data collected from published literature. The velocity field in the liquid around the bubble has been investigated using Particle Image Velocimetry (PIV) by some

researchers [83-85]. However, due to experimental difficulties, velocity profiles in the gas phase are seldom available. In the case of numerical simulations, because of the large density ratio between liquid and gas, the momentum equations and hence flow calculations are often ignored [86] in the gas phase. Polonsky *et al*. [87] observed the oscillatory motion of the bubble bottom for a long gas bubble rising in a vertical tube while the nose of the bubble retains its shape. The amplitude of oscillations increases with the bubble length, whereas the frequency remains constant. van Hout *et al.* [83] investigated the velocity field induced by a Taylor bubble rising in stagnant liquid. Velocity fluctuations were noticeable fifty tube diameters away from the wake of the bubble. It should be noted that the experimental measurements were performed at steady state while the transient effect is not accounted for in the last two studies.

In the present study, the motion of a large single gas bubble, with diameter comparable to that of the tube, rising through a stagnant liquid is investigated. The transient governing equations are solved by a finite volume scheme with a two-step projection method. The interface between the liquid and gas phase is tracked by a coupled level set and volume-of-fluid (CLSVOF) method. The PBM is employed for surface tension modeling in this study. The focus of the present work is to investigate the bubble oscillations during the initial acceleration stage by analyzing the deformation shape and the associated velocity fluctuations. The velocity field and pressure distribution in the bubble and the surrounding liquid are thoroughly examined as well.

6.3.2 Results and Discussion

As shown in Figure 6.13, a spherical air bubble with a diameter of 20 mm is located near the bottom of a vertical tube (diameter D=25 mm and height L=150 mm) containing quiescent water. Non-slip boundary conditions are imposed at the solid walls, and an open boundary condition is applied at the top of the tube. The calculations are carried out on an axisymmetric computational domain. Constant properties are used for air and water unless stated otherwise. They are given by: r_l = 1000 kg/m^3, r_g = 1.226 kg/m^3, m_l = 1.137x10^{-3} kg/ms, m_g = 1.78x10^{-5} kg/ms with g = 9.8 m/s^2, and s = 0.0728 kg/s^2. The key dimensionless parameters used in this study include: Morton number $Mo = gn^4 r_l^3 / s^3$, Eötvös number $Eo = r_l g D^2 / s$, density ratio r_l / r_g and viscosity ratio m_l / m_g.

6.3.2.1. Dynamics of Bubble Motion and Deformation

The time evolution of bubble shapes is given in Figure 6.14. The bubble, exerted by buoyancy force, rises rapidly after its release. This acceleration process is simultaneously accompanied by bubble shape deformation from the initially spherical shape to the final bullet-like shape. The bottom of the bubble rapidly moves upwards, and thus a concave shape is formed at the bottom. This cupped bottom immediately rebounds downwards into a convex shape. This up-and-down oscillatory movement of the bubble bottom continues as the bubble rises but with decreasing amplitude. The top of the bubble, on the contrary, retains a spherical cap shape with very little deformation while rising.

The velocity field at one time instant is presented in Figure 6.15 with the corresponding streamline plot shown on the left. The magnified views of several regions around the bubble are given in Figures 6.16a, b, and c. For example, the axial velocity along the center axis of the tube decreases rapidly upward away from the nose tip, and the effect of the bubble motion becomes negligible 0.5D beyond the bubble nose (Figure 6.16a). In the radial direction, the radial velocity increases away from the tip of the bubble nose and the fluid enters into the falling liquid film near the tube wall. Along the bubble interface, the flow reverses from upward inside the bubble to downward in the liquid (Figure 6.16b). In the wake region of the bubble, the falling flow in the liquid film near the tube wall mixes with the liquid slug induced by the gas bubble at approximately 2.0D away from the bottom of the bubble (Figure 6.16c). As a result, a toroidal vortex is generated, which is immediately followed by another much weaker one that circulates in the opposite direction (see Figure 6.15). It should be mentioned that the observations of the flow structure in the present numerical study are in good agreement with the findings reported in previous experimental studies on slug flows [83-85].

Figure 6.17 shows the axial velocity versus time plot at the nose and bottom of the bubble. The velocity at the bottom undergoes significant oscillations at the initial acceleration stage where the oscillation amplitude decreases gradually with time. However, these oscillations at the bottom have no influence on the behavior of the bubble nose, where the velocity rapidly accelerates and immediately reaches a constant

value of around 0.1735 mm/ms. This is in excellent agreement with the terminal velocity correlation given by $U_T = 0.35\sqrt{gD}$ reported in the literature [81, 84].

The pressure contours and the pressure distribution along the axial direction are shown in Figures 6.18a and 6.18b respectively. The top of the tube is open to the atmosphere, and thus an open boundary condition is applied there with the atmospheric pressure taken as zero. As shown in Figure 6.18a, the pressure increases gradually with depth from top to bottom, while in the gas phase the pressure is constant. Figure 6.18b shows the axial pressure distribution at three radial positions. The fluid motion is relatively weak in the region from the opening of the tube to the nose of the bubble with an almost linear increase in pressure. In the region from the top to bottom of the bubble, the pressure maintains a constant value inside the bubble and changes non-linearly in the liquid film. In the wake region of the bubble, the pressure changes non-linearly in the first recirculation zone beyond which the pressure varies approximately linearly again when the flow diminishes. It is also shown that the pressure variation in the radial direction is very small except near the bubble interface where a pressure jump induced by the surface tension exists.

6.3.2.2 Bubble Oscillations

As discussed previously, during the acceleration process, significant bubble deformation occurs, which is characterized by oscillatory motions at the bottom with a relatively stable spherical cap shape maintained at the nose (see Figure 6.14). This is also manifested by the velocity fluctuations at the bottom as shown in Figure 6.17. The velocity at the nose quickly reaches the terminal velocity and remains constant, while

the velocity at the bottom undergoes severe oscillations. The variation of the bubble length (distance from the nose to the bottom) with time is given in Figure 6.19, where bubble shape oscillations can be inferred. The Fourier transforms of the bubble length and the bottom velocity are obtained to correlate and analyze the oscillation characteristics. Power spectra of bubble lengths and bottom velocity oscillations are given in Figure 6.20. Note that both the bubble length oscillations and the bottom velocity oscillations have an almost identical dominant frequency at approximately 12.7 Hz.

It is of interest to compare the numerical results of the present study with theoretical calculations in order to validate the accuracy of the numerical simulation. In a recent study [87] of the time-dependent characteristics of the motion of an elongated bubble in a vertical pipe, the bubble bottom is treated as a circular liquid membrane modeled by potential flow theory. The velocity potential, Φ, is governed by the Laplace equation:

$$\nabla^2 \Phi = 0 \tag{6-5}$$

with a solution given by:

$$\Phi(r,q,z,t) = A_s J_s(kr)\cos(sq)e^{kz+i(wt+e)} \tag{6-6}$$

where A_s is the arbitrary amplitude, J_s the Bessel function of the first kind of order *s*, *k* the wave number, *w* the angular frequency, and *e* the arbitrary phase angle. The derivation follows that of Lamb [88] where a more detailed discussion of the solution can be found. The wave number *k* is determined by the condition that the radial velocity at the rim of the bubble bottom is zero, i.e.,

$$\left.\frac{\partial \Phi}{\partial r}\right|_{r=R} = 0 \tag{6-7}$$

Due to the symmetrical oscillation character of the bubble bottom imposed in the present numerical simulation, *s* is taken as zero, and Eq. (6-7) becomes:

$$J_0'(kr)\big|_{r=R} = 0 \tag{6-8}$$

The oscillation frequency, $f(=\frac{w}{2p})$, can then be obtained by substituting *k* into the gravity-capillary wave dispersion relation below:

$$w = gk + \frac{s}{r}k^3 \tag{6-9}$$

For a bubble bottom radius of 10.6 mm, the oscillation frequency corresponding to the lowest mode is 13.3 Hz. This is in good agreement with the value of 12.7 Hz obtained in the present numerical simulation.

6.3.2.3 Effects of Fluid Parameters on the Oscillations

A number of cases for different fluid parameters are investigated to identify the factors controlling the oscillatory behaviors of bubble velocity and shape. Figures 6.21a and 6.21b show the velocity versus time plot for cases with different liquid viscosities. The liquid viscosity values used are 10.0 times that of water in case a, and 0.1 times in case b. It can be seen that an increase in liquid viscosity leads to a decrease in oscillation amplitude and overall duration with larger amplitude and longer overall duration attained by reduction in liquid viscosity. This implies that liquid viscosity has a damping effect on the oscillations, as expected. However, as shown in Figure 6.22a, the oscillation frequency is relatively unaffected by the variation in liquid viscosity. The

dominant frequencies for all three cases with different viscosities are almost identical. The gas viscosity plays a negligible role in the bubble motion and is therefore ignored.

Figures 6.21c and 6.21d show rise velocity versus time plots for cases with different surface tension coefficients. The surface tension coefficient values considered are twice and half that of water. With larger surface tension force, the oscillations become stronger in the sense that both the amplitude and the frequency are increased. With decreased surface tension force, both the amplitude and frequency are decreased. Power spectra of bottom velocity oscillations with different surface tension coefficients are shown in Figure 6.22b. It is clear that the dominant frequency increases with increase in surface tension.

It should be noted that for all the cases discussed above, *Mo* is less than 2.56×10^{-7} and *Eo* is greater than 42.0. According to the *Eo*-*Re*-Diagram (Figure 2.5 in [1]), the bubble will take on a "spherical-cap" shape in an unbounded liquid under these conditions. However, the bubble considered in the current study is confined in a narrow tube. As shown in Figure 6.23, the bubble nose takes on a slightly prolate spheroid shape due to the effect of the tube wall. Meanwhile, the bubble nose shape does not vary much between the different cases, although the bottom shape changes significantly. Moreover, velocity oscillations occur only at the bottom of the bubble, while the velocity at the nose maintains a nearly constant value during bubble rise (Figures 6.21a, b, c, and d). It appears that the behavior of the bubble nose is independent of the parameters studied. However, a close examination of Figure 6.21c reveals that the nose velocity curve is slightly wavy, which suggests that nose

oscillations might occur if the surface tension force is sufficiently large. This speculation is confirmed by further increasing the surface tension coefficient by a factor of 10 resulting in $Mo = 2.56\times10^{-14}$ and $Eo = 8.4$. As shown in Figure 6.24a, the velocities at both the nose and the bottom exhibit severe oscillations. In this case, the surface tension force is dominant, and the bubble will take on an "ellipsoidal or wobbling" shape which is outside the Taylor bubble regime. The time sequence of bubble shapes is shown in Figure 6.24b where apparent shape oscillations can be seen. In this regime, non-axisymmetric oscillations, such as trajectory instabilities, will certainly occur in an infinite liquid. In the present study, such trajectory oscillation has been eliminated due to the constraints at the tube wall.

6.3.3 Conclusions

The dynamics of a single gas bubble rising in a narrow vertical tube have been studied via a numerical method. The velocity field as well as the pressure distribution have been investigated and analyzed. The results obtained in the present study are in very good agreement with experimental results reported in the literature. Special attention is paid to bubble oscillations at $Mo < 2.56\times10^{-7}$ and $Eo > 42.0$. It has been found that the bubble nose retains a relative stable shape while significant oscillations occur at the bubble bottom as it rises through the liquid from the static state. The parametric study shows that the liquid viscosity plays an important role in damping the oscillations without altering the oscillation frequency; while the surface tension significantly changes both the oscillation frequency and the amplitudes.

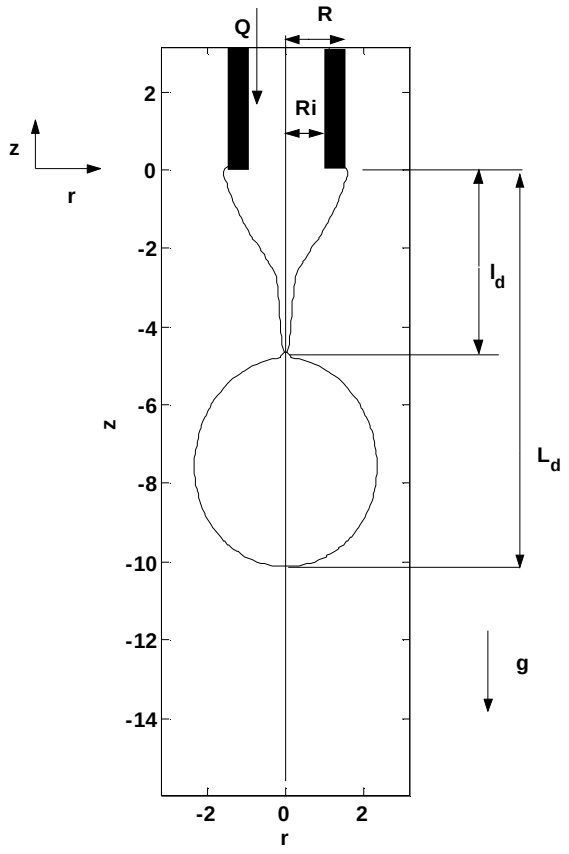

Figure 6.1 The schematic of pendant drop forming from a vertical capillary tube.

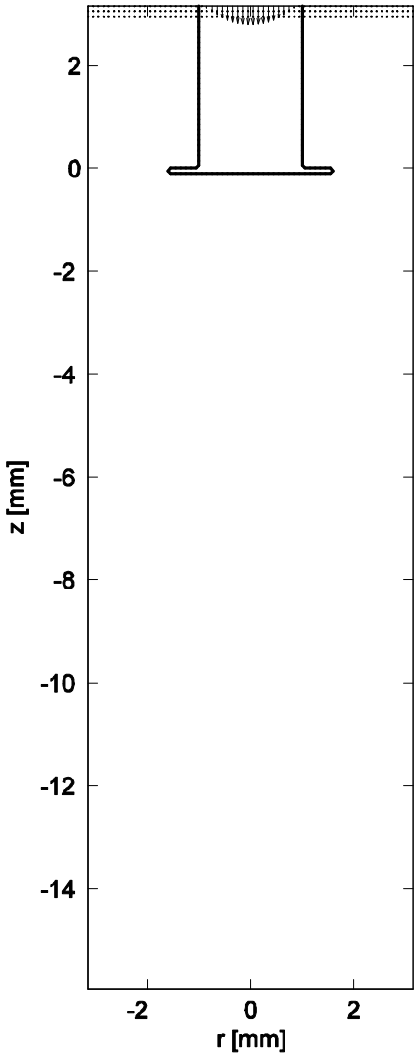

Figure 6.2 The initial flow field of water droplet computation.

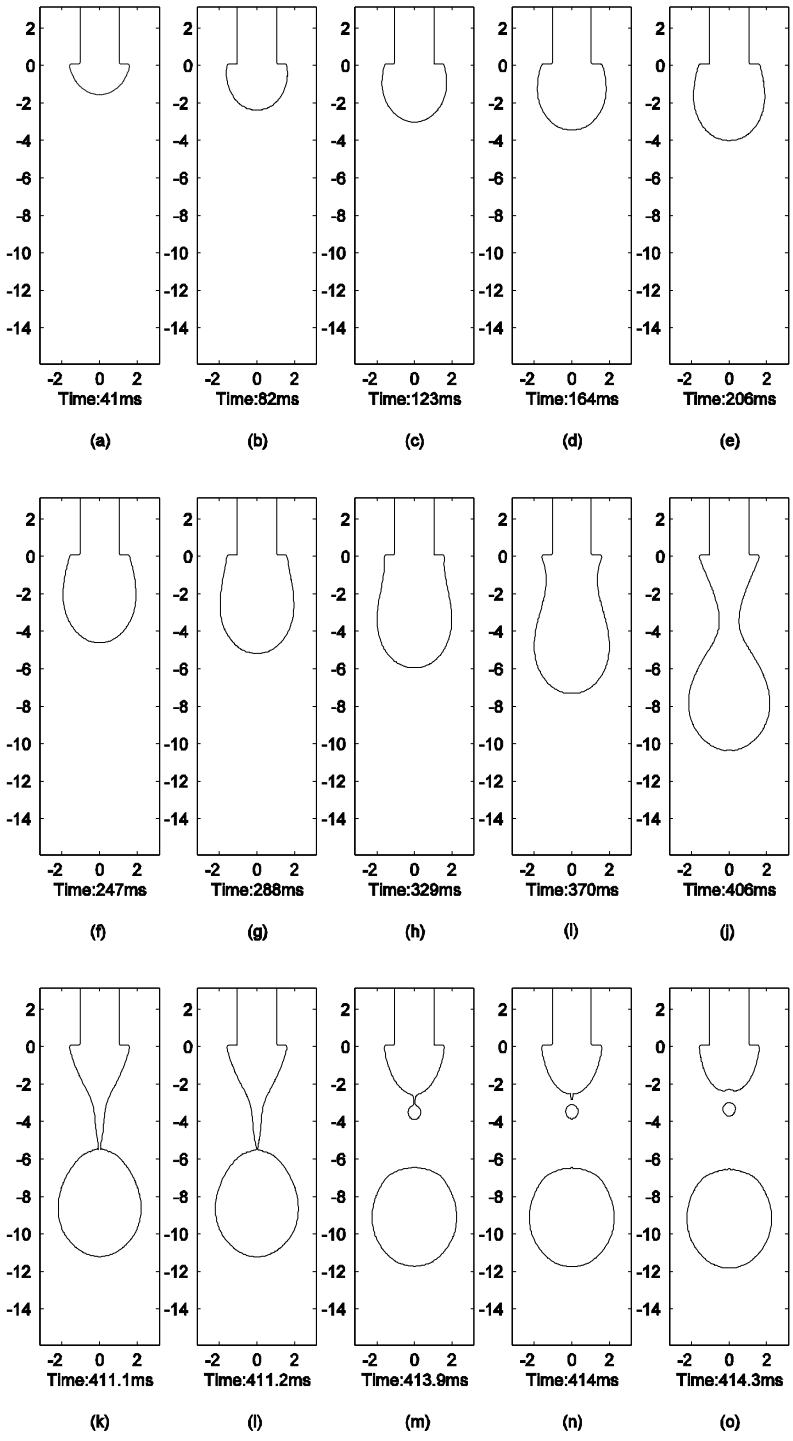

Figure 6.3 (a)-(o) The evolution of a pendant drop from a tube of inner radius R_i = 1.0 mm and outer radius R = 1.6 mm at the liquid flow rate Q = 10 mL/min with a parabolic inlet velocity profile. The numerical scheme is the VOF-PLIC.

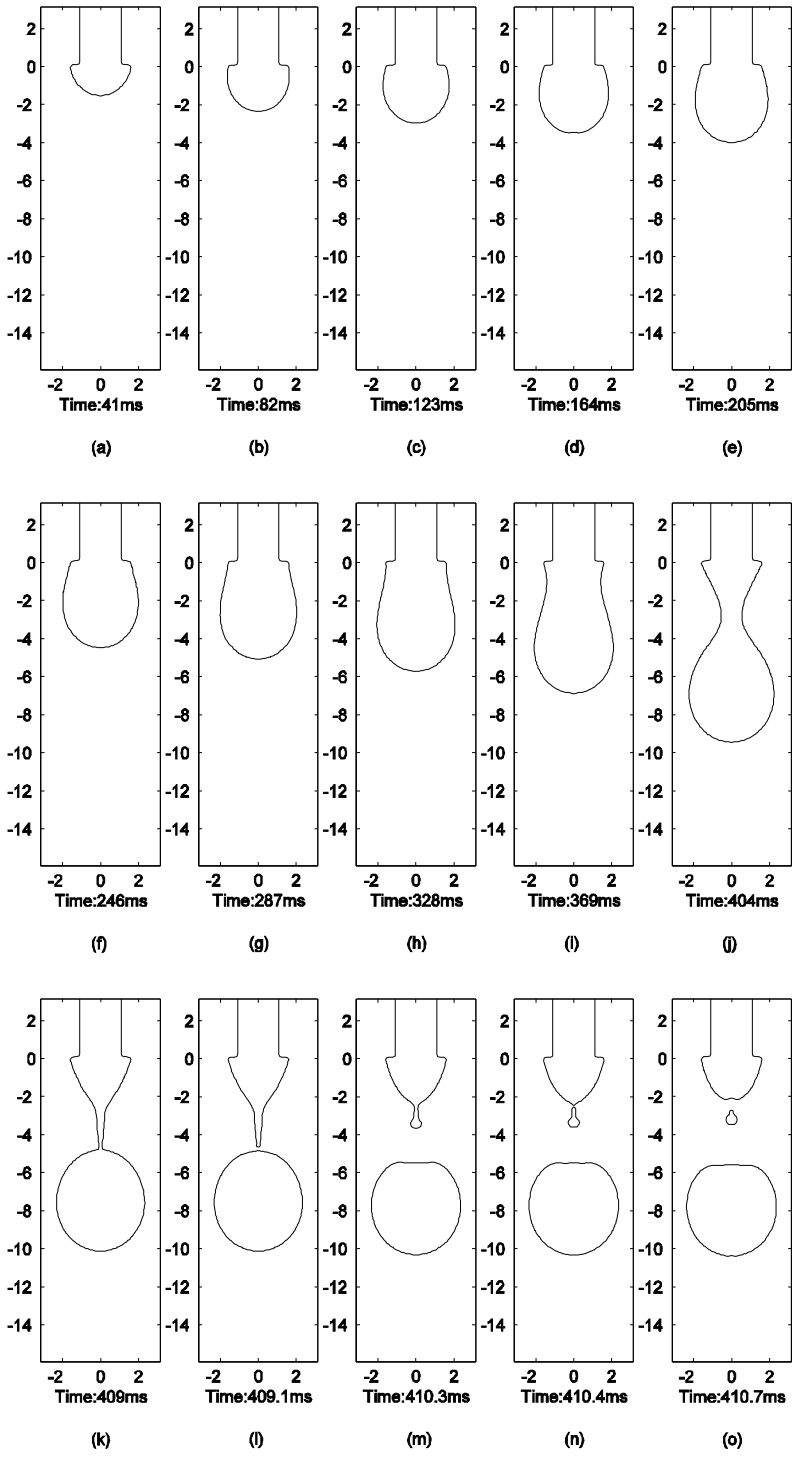

Figure 6.4 (a)-(o) The evolution of a pendant drop from a tube of inner radius R_i = 1.0 mm and outer radius R = 1.6 mm at the liquid flow rate Q = 10 mL/min with a parabolic inlet velocity profile. The numerical scheme is the CLSVOF.

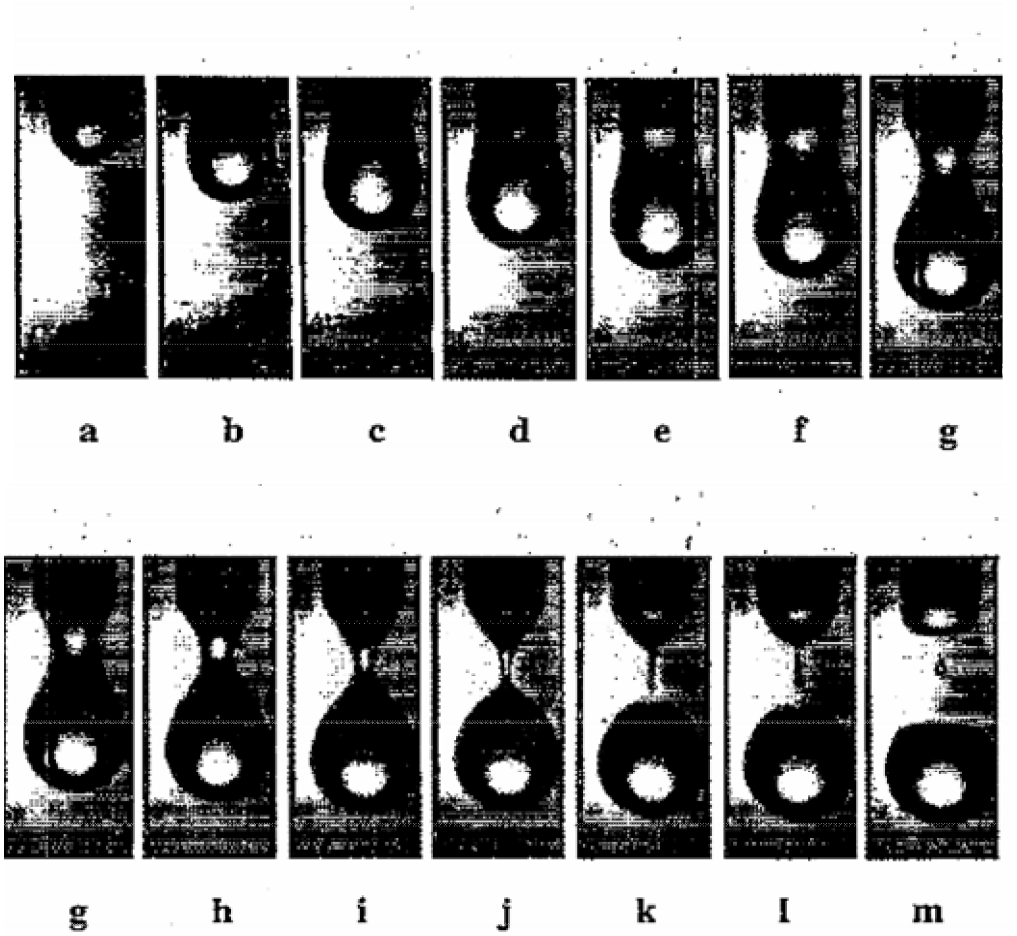

Figure 6.5 (a)-(m) Time sequence of a pendant water droplet from a tube in air. [Zhang and Basaran, 1995]

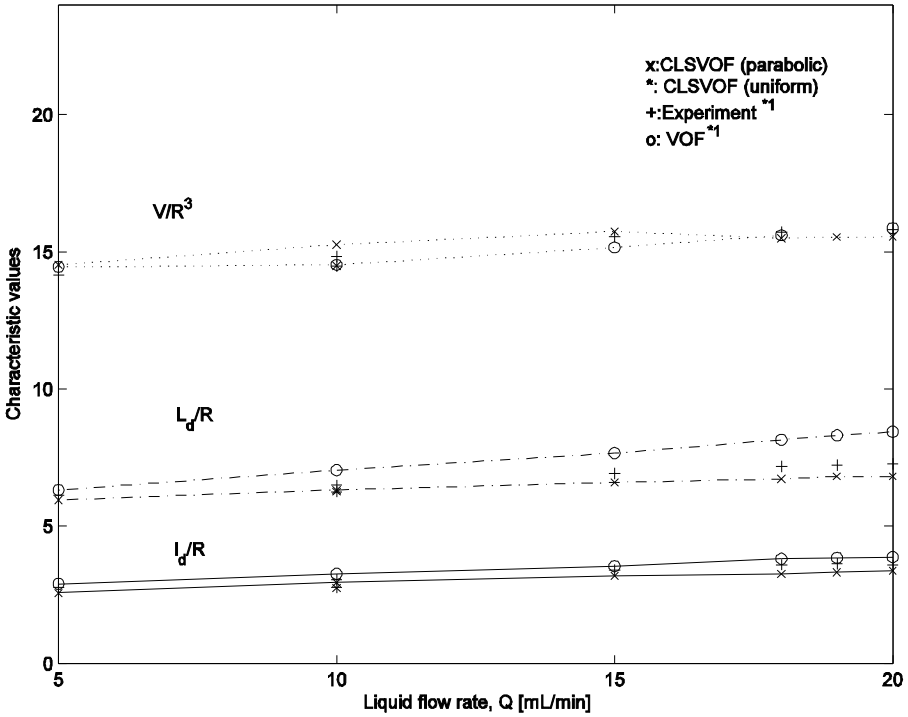

*1: Data from Zhang [1995]

Figure 6.6 Comparison of characteristic values of water droplets as a function of the liquid flow rate.

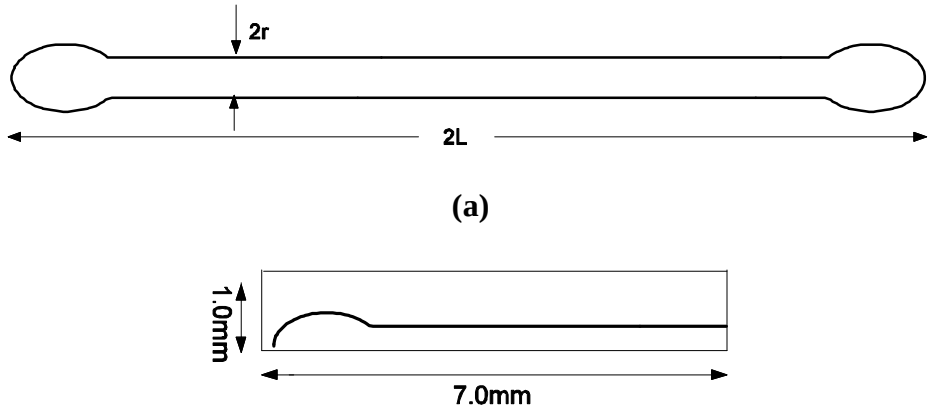

Figure 6.7 Schematic representation of an elongated ligament: (a) a full ligament with elliptic ends; (b) computational domain configuration.

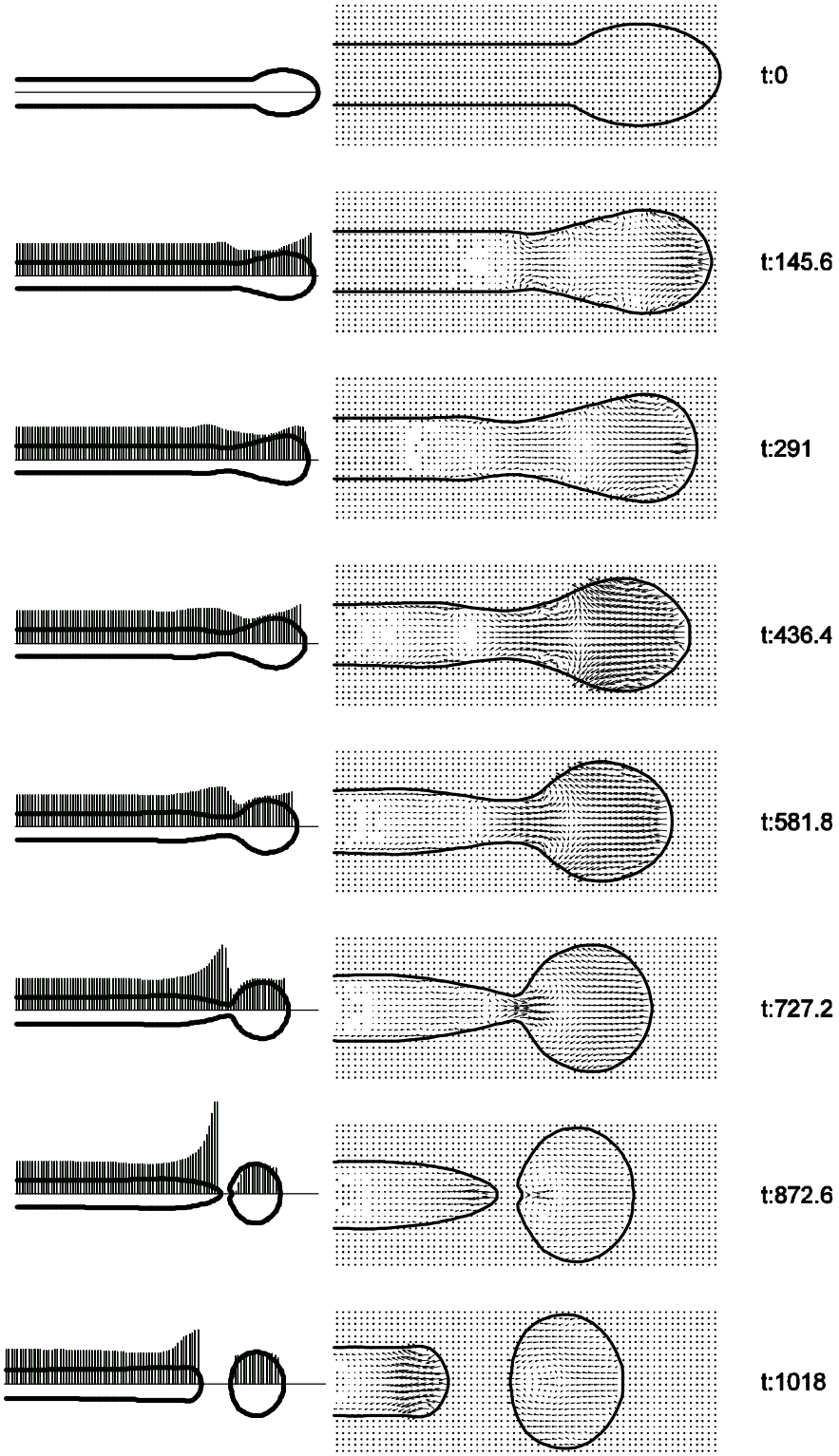

(a) (b)

Figure 6.8 Pressure and velocity distribution during relaxation process: (a) pressure distribution along the axis of the ligament; (b) velocity profile.

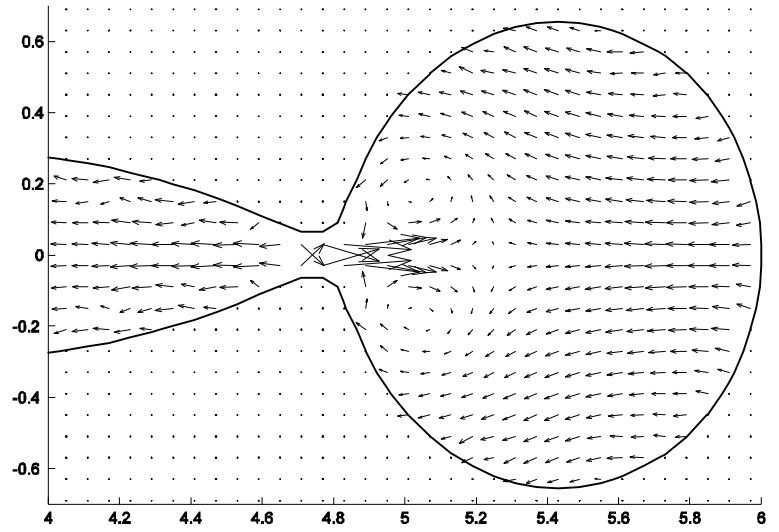

(a)

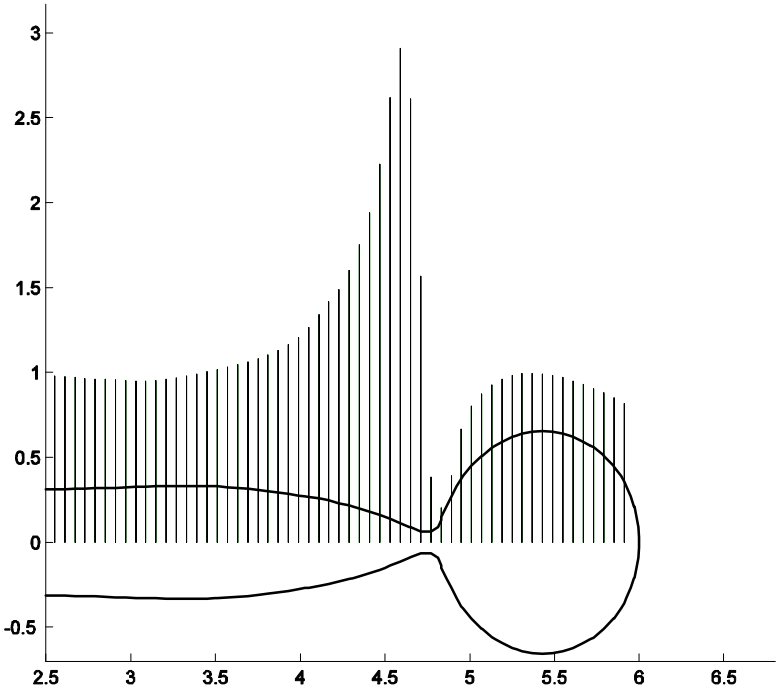

(b)

Figure 6.9 Flow field and pressure distribution immediately prior to breakup (magnified view): (a) flow field; (b) pressure distribution.

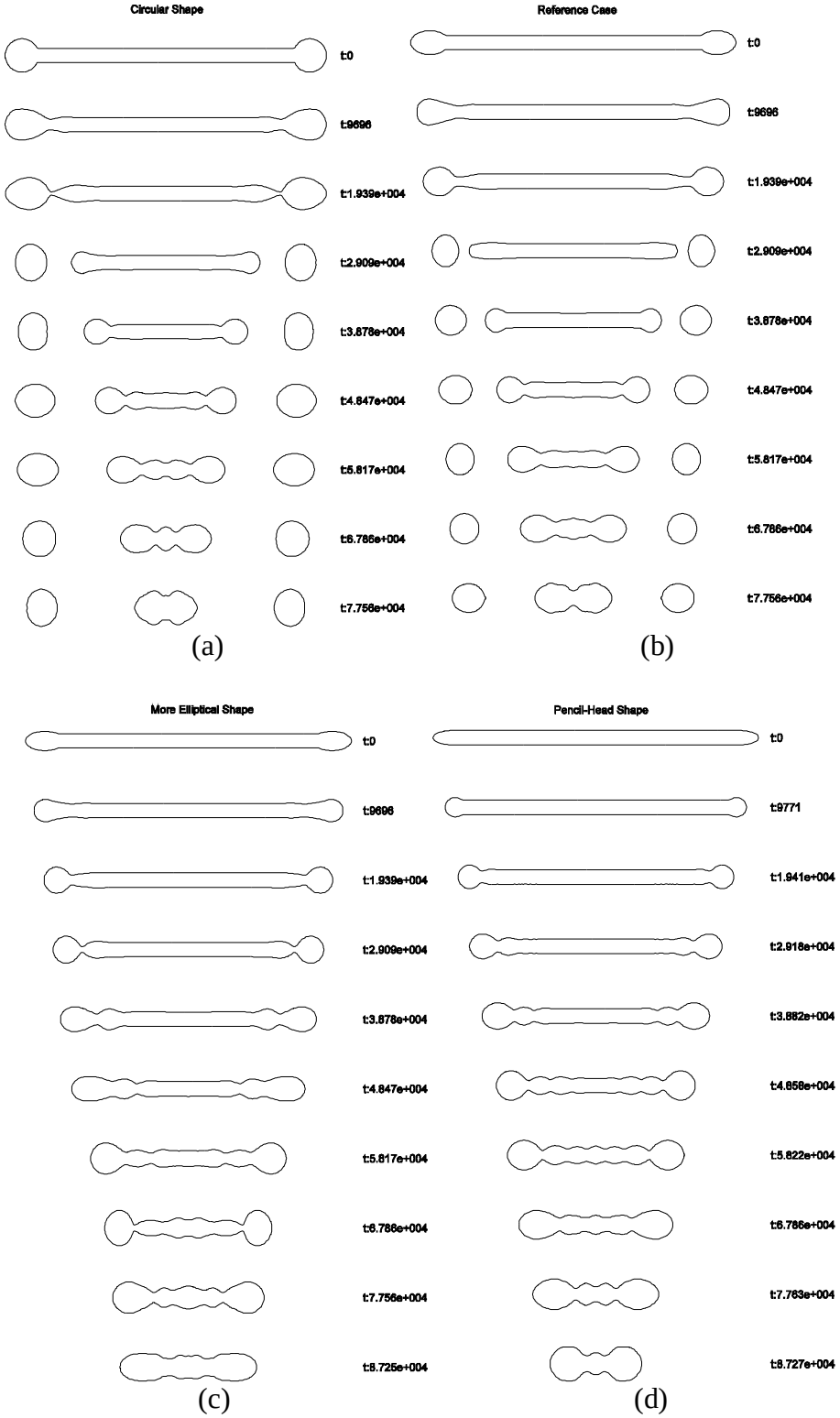

Figure 6.10 Ligament relaxation process with different end shapes: (a) circular shape; (b) reference case (elliptic shape); (c) more elliptic shape; (d) pencil-head shape.

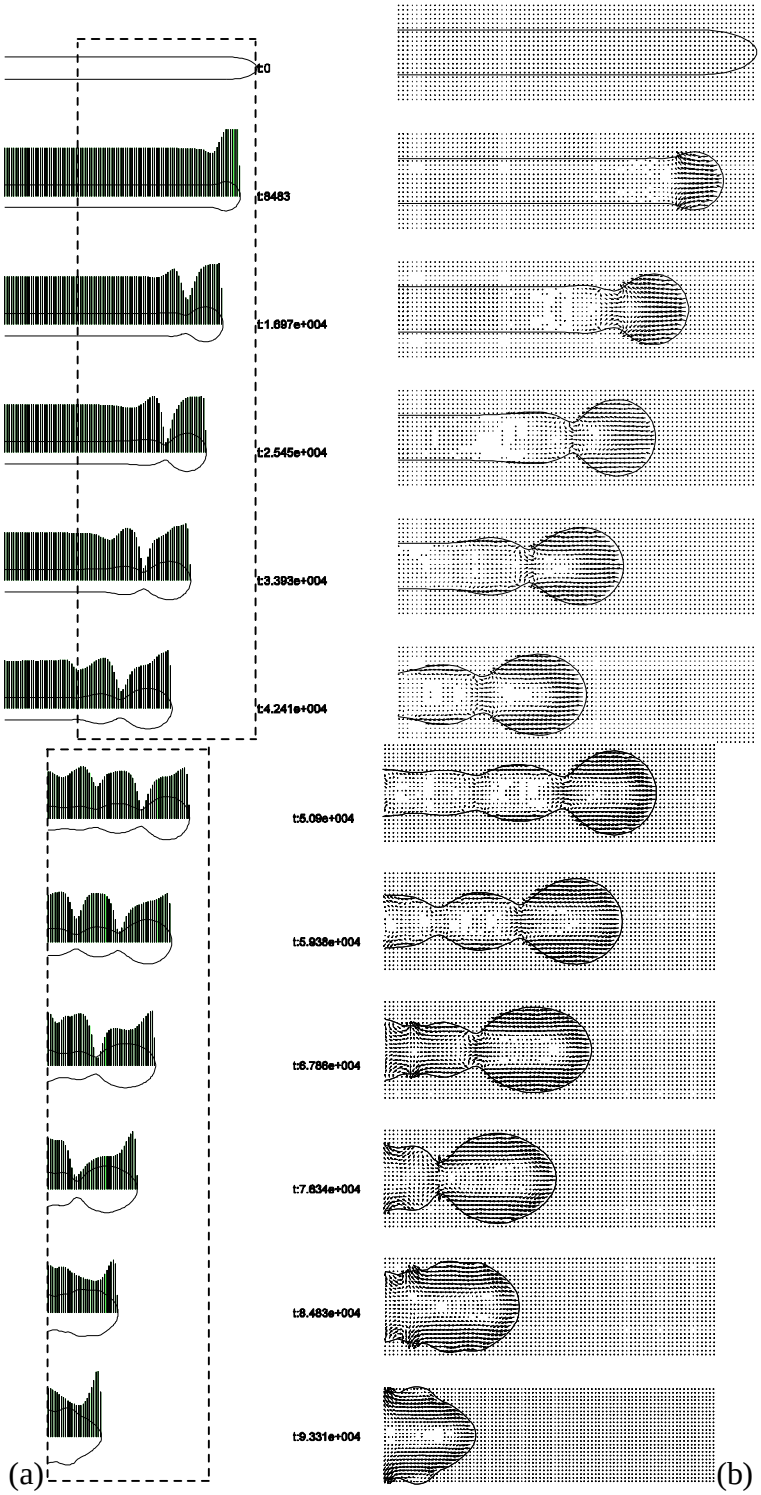

Figure 6.11 Relaxation process of an elongated ligament with pencil-head end shape: (a) pressure distribution along the axis of the ligament; (b) velocity profile, magnified the dashed region of (a).

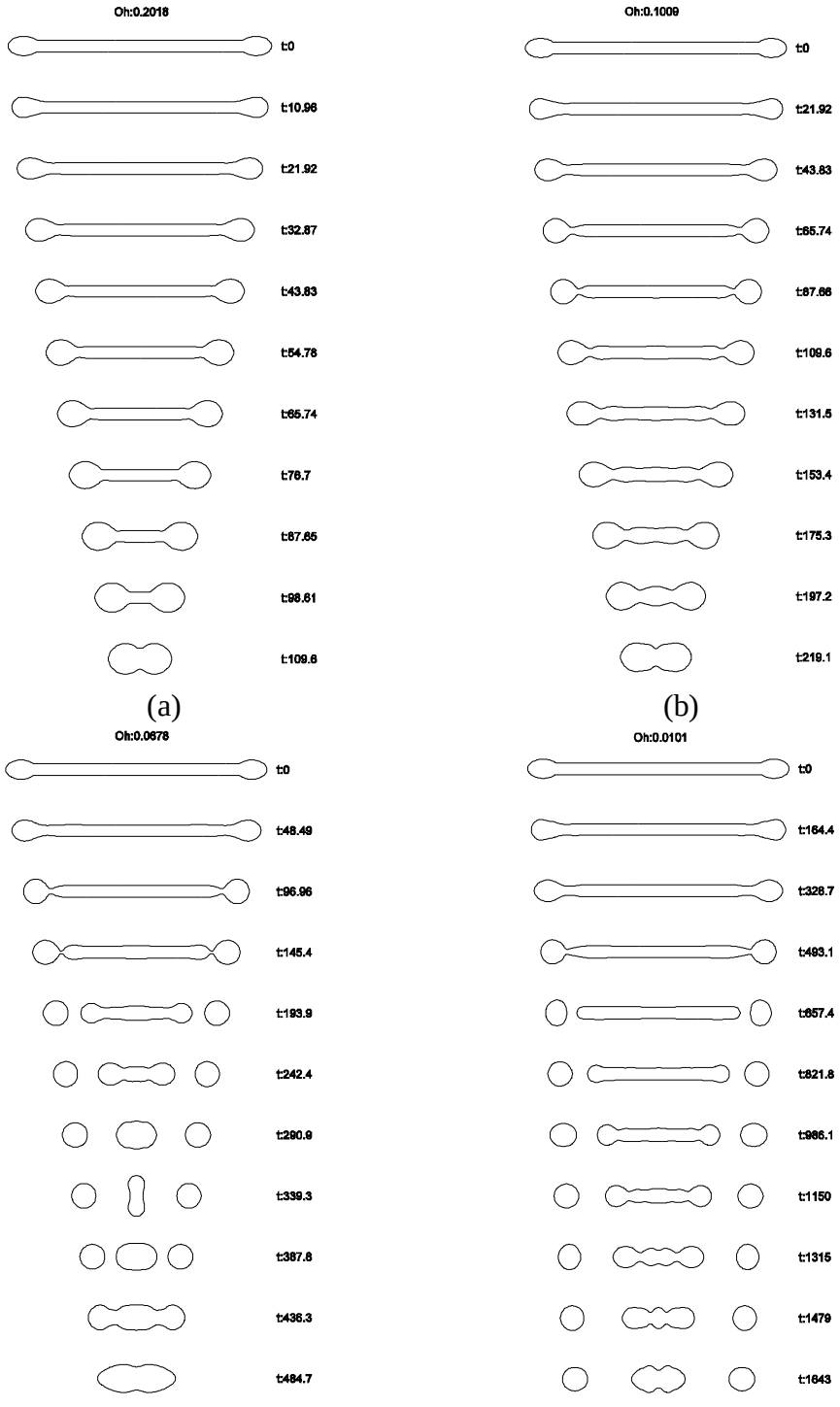

Figure 6.12 Relaxation processes of a ligament with different Oh numbers: (a) Oh=0.2018; (b) Oh=0.1009; (c) Oh=0.0678; d) Oh=0.0101.

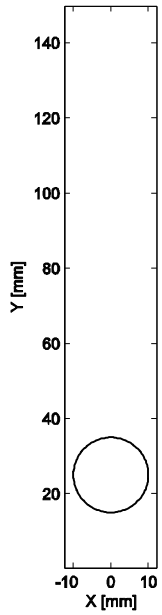

Figure 6.13 Initial configuration of the computational domain.

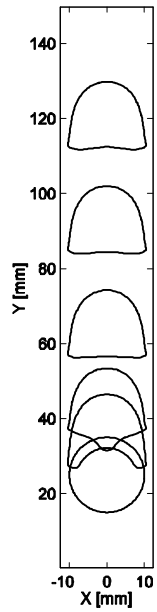

Figure 6.14 Time dependent deformation sequence of a single air bubble in a narrow tube.

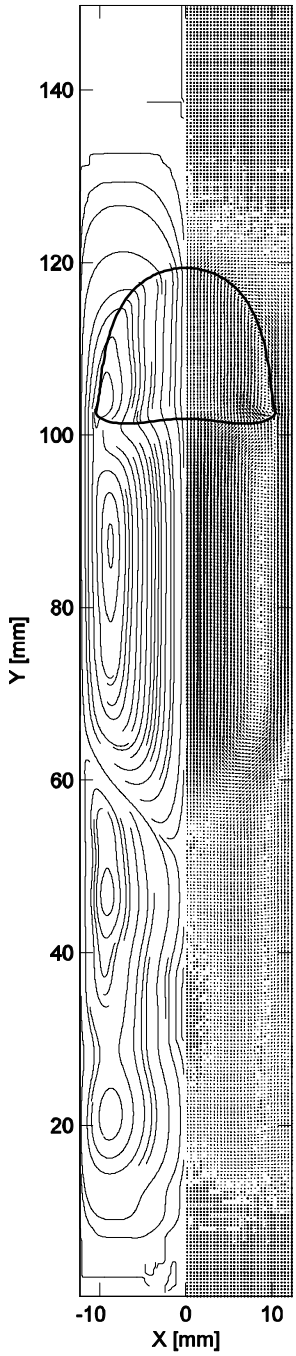

Figure 6.15 Velocity vector field and streamline plot at one time instant.

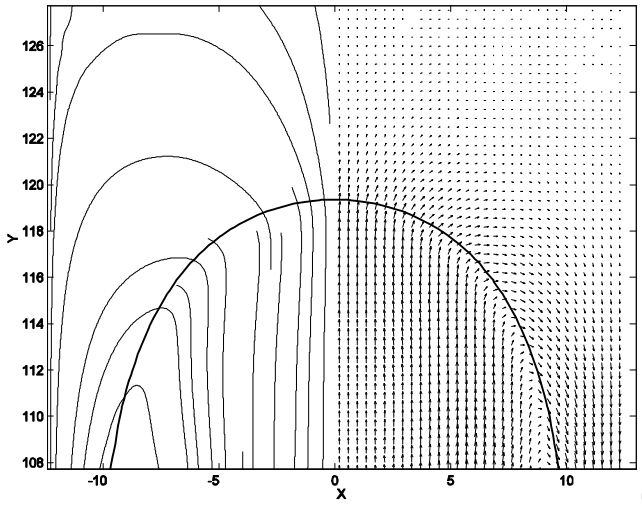

(a)

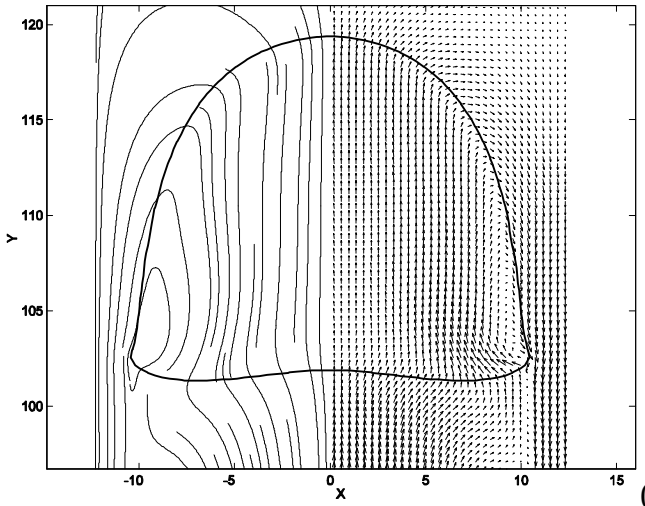

(b)

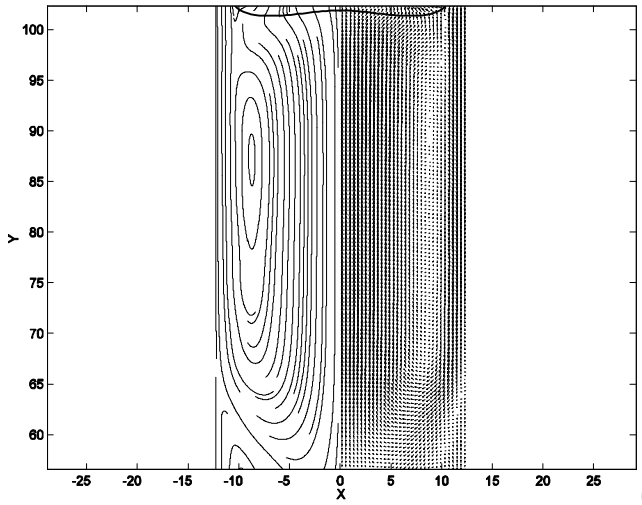

(c)

Figure 6.16 Velocity field (magnified views): (a) top region; (b) side region; (c) wake region.

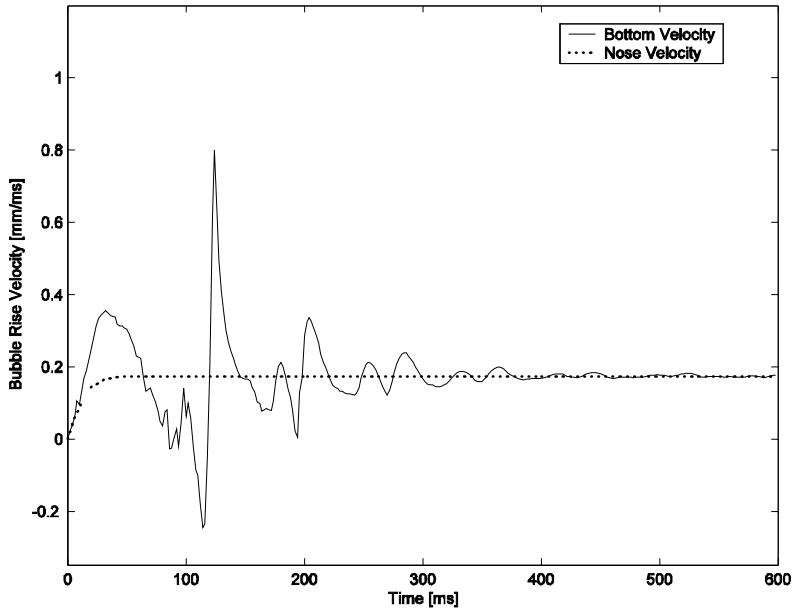

Figure 6.17 The axial velocity versus time at the nose and bottom of the bubble.

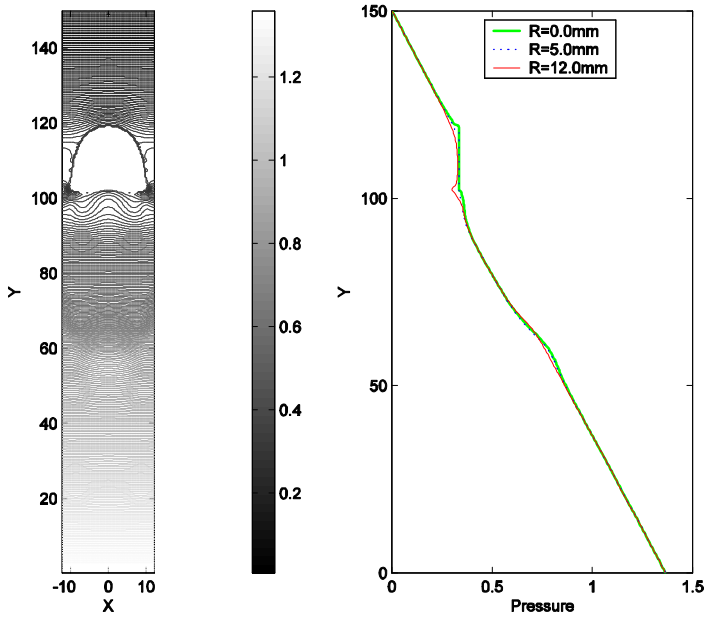

(a) (b)

Figure 6.18 (a) Pressure contour plot. (b) Pressure distribution along the centerline of the tube at various radial positions.

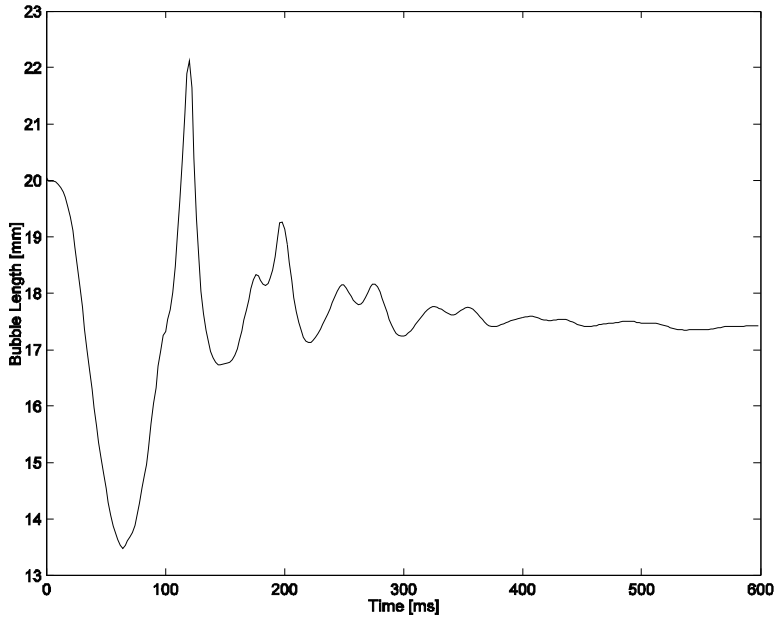

Figure 6.19 The variation of bubble length versus time.

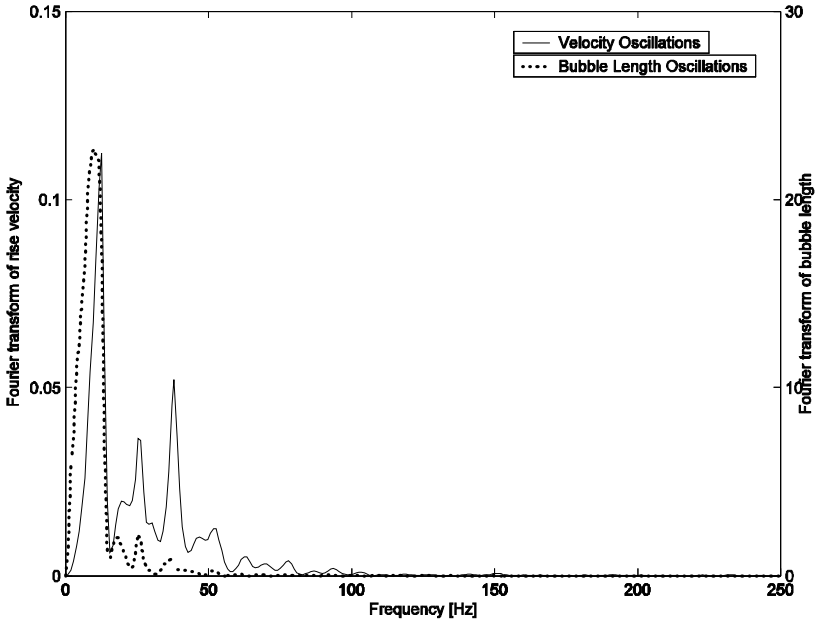

Figure 6.20 Power spectra for the oscillations of the bottom velocity and bubble length.

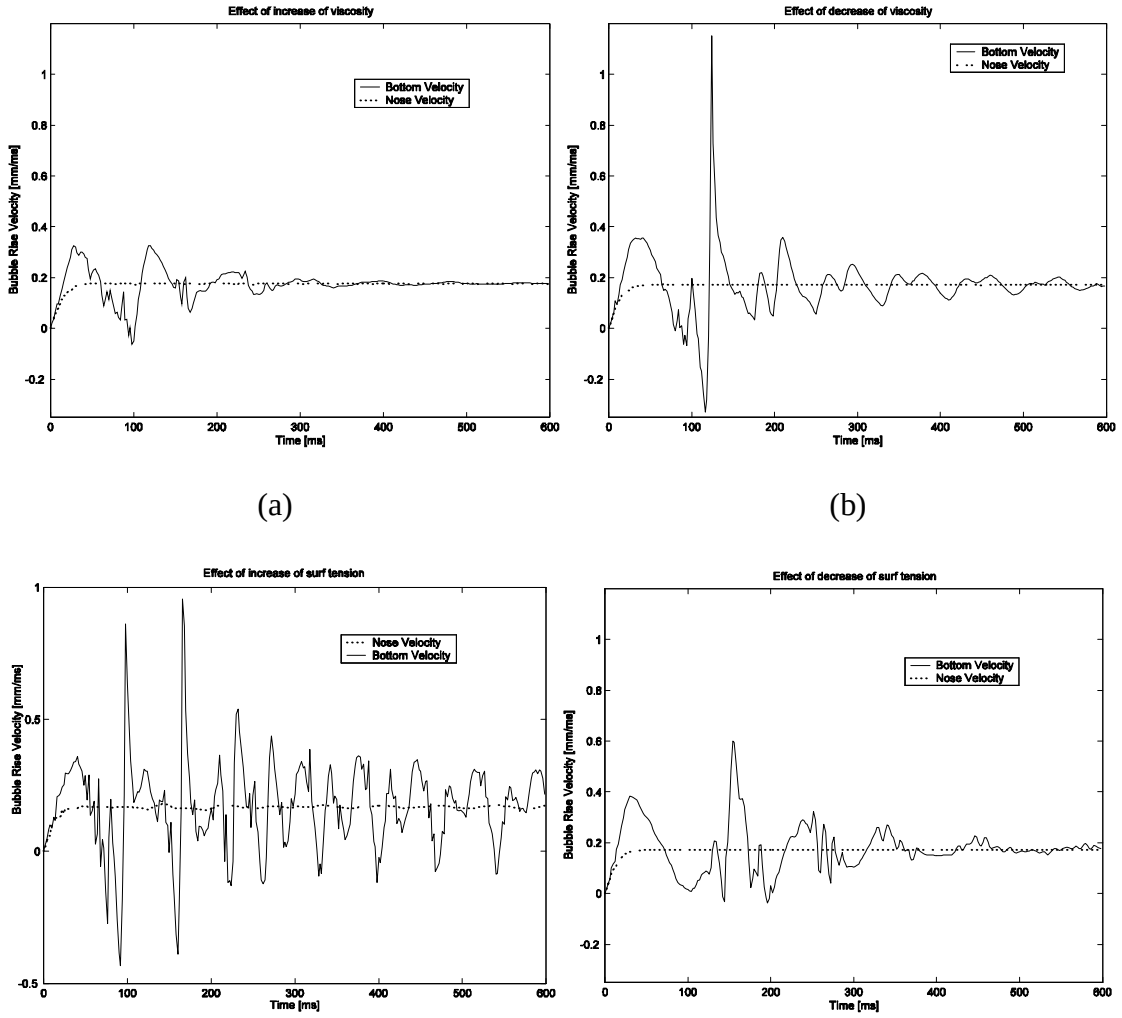

Figure 6.21 Bubble rise velocity at the nose and bottom for different cases: (a) high viscosity ($10n$); (b) low viscosity ($0.1n$); (c) high surface tension ($2.0\,s$); (d) low surface tension ($0.5\,s$).

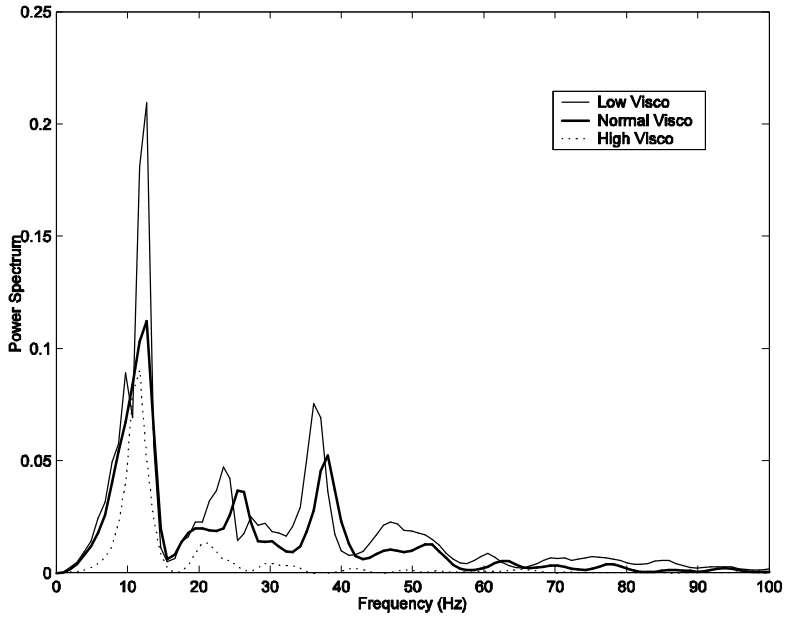

(a)

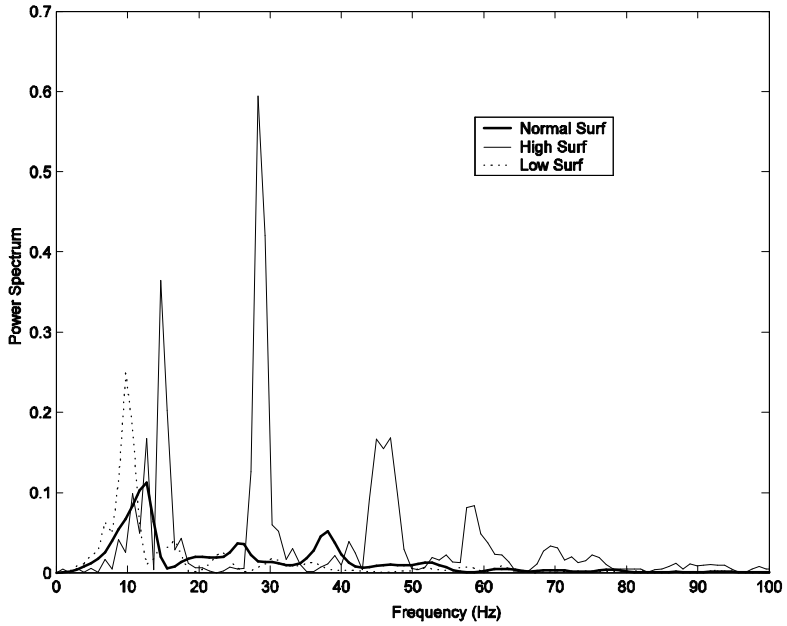

(b)

Figure 6.22 Spectra of bubble bottom velocity oscillations: (a) viscosity effect; (b) surface tension effect.

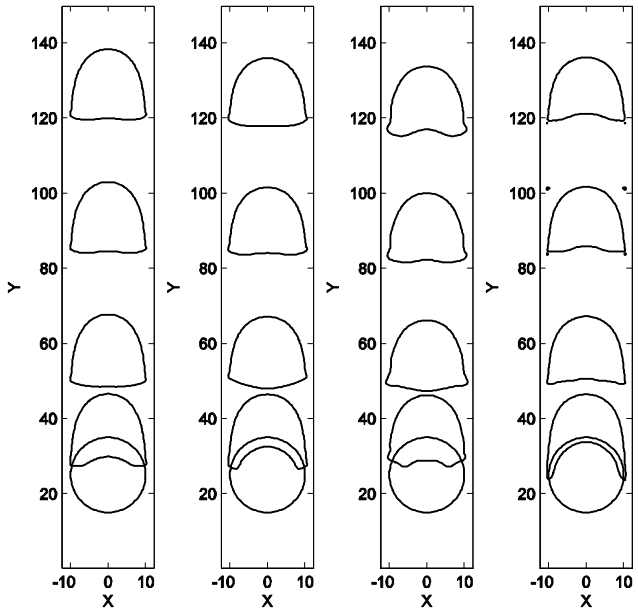

Figure 6.23 Time evolution of the bubble shapes for different cases: (a) high viscosity; (b) low viscosity; (c) high surface tension; (d) low surface tension.

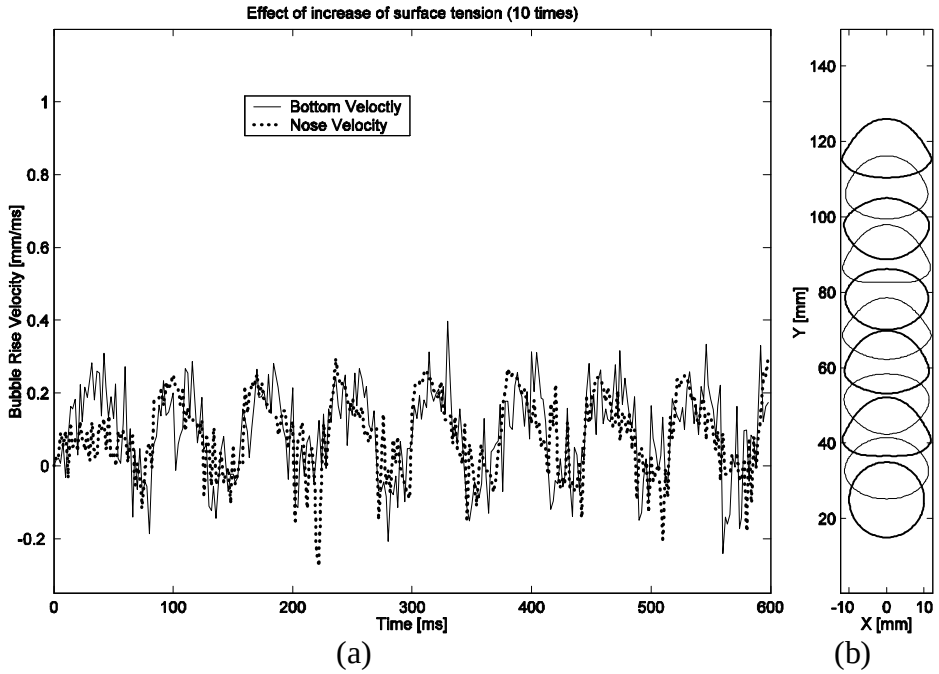

Figure 6.24 (a) Bubble rise velocity at the nose and bottom of the bubble with a higher surface tension ($10\,s$). (b) Time evolution of bubble shapes.

CHAPTER 7

CONCLUSIONS AND FUTURE WORK

Numerical methods for interface simulation and surface tension modeling have been investigated with the focus on surface tension dominant free surface and interfacial flows. A coupled level set and volume-of-fluid (CLSVOF) scheme has been employed and successfully implemented for the interface tracking. A surface tension modeling algorithm, referred to as the pressure boundary method (PBM), has been developed and applied in both free surface and two-phase interfacial flows.

The CLSVOF method combines both the strengths of the LS and the VOF methods with the advantages that the computation of the curvature and the normal is more accurate, and the mass conservation is preserved as well. In free surface flows, the CLSVOF method in conjunction with the CSF model shows superiority over the VOF method for surface tension modeling. The spurious currents originating from the CSF model are greatly reduced in the CLSVOF method. Although the combination of the CLSVOF and the CSF succeeds in some free surface flow problems, its capability is limited for two-phase interfacial flows. For two-phase interfacial flow with a high surface tension and a large density ratio, the accuracy of the CLSVOF-CSF method deteriorates seriously and leads to the failure of the computation due to the existence of spurious currents. This problem is eliminated with the PBM method used for surface

tension force modeling. The CLSVOF-PBM method drastically suppresses the spurious currents not only in free surface flows but also in two-phase interfacial flow. The sharp pressure jump is preserved in the PBM method without numerically smoothing of the pressure profile, which is more consistent with the nature of the surface tension effect. The accuracy and capability of the various algorithms are summarized in Table 7.1,

Table 7.1 Comparison of the Accuracy and Capability of Different Methods for Free Surface and Two-Phase Interfacial Flows

Numerical Methods	Free Surface flow		Two-phase interfacial flow	
	High surface tension	Low surface tension	Large density ratio	Small density ratio
VOF-CSF	Low	Moderate	N/A	N/A
CLSVOF-CSF	Moderate	High	N/A	Low
CLSVOF-PBM	High	High	High	High

The CLSVOF and PBM algorithms have been applied to several practical problems, through which the robustness and versatility are further validated. In the first application, the breakup mechanism of a pendant droplet is studied. In this study, both the CLSVOF method and the VOF method combined with the CSF model are used for comparison purposes. The numerical results are compared with experimental and numerical data available in the literature, with the CLSVOF method yielding better agreement than the VOF method. Furthermore, while grid convergence is achieved by

the CLSVOF method, the VOF scheme fails to converge in the grid refinement test. The superiority of the CLSVOF method over the VOF method is apparent.

In the study of the relaxation of an elongated liquid ligament, the CLSVOF method is used for the free surface tracking in conjunction with the CSF model for the surface tension. The breakup mechanism has been examined and a flaw in the published "end-pinching" mechanism has been identified that enables an explanation of the "re-open" process of the neck of the ligament. The relaxation dynamics of the ligament have been found to be governed by the initial shape and the Ohnesorge number. The end shape has been found to play an important role in the breakup process. A more circular bulbous end enhances the likelihood of pinch off. The results of the numerical simulations are in agreement with the experimental findings in the literature.

As an example of two-phase interfacial flow problems, the dynamics of a single gas bubble rising in a narrow vertical tube are investigated, with the interface tracked by the CLSVOF method and the surface tension modeled by the PBM method. The velocity field as well as the pressure distribution have been investigated and analyzed. The results obtained in the present study are in very good agreement with experimental results reported in the literature. Special attention is paid to bubble oscillations at $Mo < 2.56\times10^{-7}$ and $Eo > 42.0$. It has been found that the bubble nose retains a relatively stable shape while significant oscillations occur at the bubble bottom as it rises through the liquid from the initial static state. A parametric study has been performed which shows that the liquid viscosity plays an important role in damping the

oscillations without altering the oscillation frequency, while the surface tension significantly changes both the oscillation frequency and the amplitudes.

The above applications provide evidence for the accuracy, robustness and versatility of the numerical algorithms developed in this study. With this numerical tool, various free surface and interfacial flow problems, such as bubble formation, bubble coalescence and breakup, droplet impingement, *etc.*, can be studied.

It should be noted that the current methods are limited to the two dimensional axisymmetric case. Extension to three-dimensional problems is desirable which involves more challenges and difficulties (e.g., a more complex interface reconstruction scheme is needed). Due to the explicit treatment of the viscous term in the Navier-Stokes equation, the current code is unable to solve low Reynolds number flow problems. An implicit treatment of the viscous term will allow the code to model more viscous flows and to eliminate the time step constraints due to the viscosity. In this code, only the momentum and the continuity equations are solved; adding an energy equation model with phase-change will allow the code to simulate two-phase interfacial flows with heat transfer and evaporation. With these further enhancements, the range and variety of free surface and interfacial flow problems that are able to be modeled can be extended. This might be attempted in future work.

APPENDIX A

COMPUTER PROGRAM EXECUTION

A1. OVERVIEW

The computer program used in this thesis includes three different versions, which were developed based on a single-phase flow solver [16]. These codes were written in the computer language FORTRAN under the UNIX/LINUX operating system. All the calculations in this thesis are performed on the High Performance Computing (HPC) system of the University of Texas at Arlington. These three program packages are devised for different purposes: two for free surface flows and one for two-phase interfacial flows. Some comments regarding the codes and numerical algorithms used are given below.

1. Free Surface Flow Code

Two different versions of the code featuring different surface tension modeling methods, CSF or PBM, are available for free surface flows.

1). For the code with the CSF model, there are two options for the free surface tracking methods. The free surface can be tracked either by the "pure" VOF method or the "CLSVOF" scheme.

2). If the PBM method is used, the free surface can only be tracked by the CLSVOF scheme. This is because the level set functions are needed in the PBM algorithm.

2. Two-Phase Interfacial Flow Code

For two-phase interfacial flow problems, only one version of the code is available. In this package, the surface tension force is modeled by the PBM method with the interface tracked by the CLSVOF scheme.

A2. PROBLEM SET-UP AND SAMPLE INPUT

1. Problem Set-Up

A physical problem can be treated either in free surface flow mode or two-phase interfacial flow mode, the choice of which depends on the problem to be simulated. Generally, if the "dispersed phase" is liquid and the "continuous phase" is gas, such as a water droplet falling in air, the free surface mode is suitable. On the other hand, if the "dispersed phase" is air or liquid and the "continuous phase" is liquid, such as an air bubble rising in water, or an oil droplet moving in water, the two-phase mode is desirable. Once the appropriate mode is chosen, necessary information, such as geometry, fluid properties, boundary conditions and initial conditions, needs to be gathered, which can be specified and incorporated into the code via an *input* file. Detailed information and explanation of the input variables can be found in [15, 16, 70]. A sample input file for a water droplet falling in air is given in the following; modifications made to the input file suited for the new programs are described.

2. Sample INPUT

```
Droplet_impact  [mm,ms,mg,K]
 $numparam
   alpha=2.0,
   autot=1.0,
   conserve=.true.,
   delt=1.0e-3,
   dtmax=1.0e-2,
   twfin=200000.0,
   con = 0.3
   fcvlim=0.5,
   idiv=1,
   dmpdt=3000000.0,
   prtdt=1000000.0,
   pltdt=4.0e-2,
   sym=.true.,
   kt=2,
   kb=2,
```

```
  kl=1,
  kr=1,
$end
$fldparam
  gy=-9.81e-3,
  icyl=0,
  isurf10=1,
  psat = 0.0,
  xnul=1.08e-3,------Liquid viscosity,
  xnug=1.78e-5,------Gas viscosity,
  rhofl=1.0,---------Liquid density,
  rhofg=1.0e-3,------Gas density,
  sigma=7.28e-2,
  vi=1.0,
  canglet=45.0,
$end
$mesh
  nkx=1,
  xl=0.0,0.625,
  xc=0.625,
  nxl=50,
  nxr=0,
  dxmn=0.0125,
  nky=1,
  yl=0.0,1.25,
  yc=1.25
  nyl=100,
  nyr=0,
  dymn=0.0125,
$end
$obstcl
  nobs=0,
$end
$freesurf
  nfrsrf=2,iequib=0,
  fc1(1)=-1.0, ifh(1)=1,
  fa1(2)=-0.625, fa2(2)=1.0,
  fb1(2)=-2.0, fb2(2)=1.0, fc1(2)=1.08203125, ifh(2)=0,
$end
$graphics
  plots=.true., dump=.false.,
  iout = 0, 1, 0, 0, 0, 0, 0, 0, 0, 0, 0, 0, 0,
         0, 0, 0, 0, 0, 0, 0, 0, 0, 0, 0, 0, 0,
         0, 0, 0, 0, 0, 0, 0, 1, 0, 0,-1, 0, 1,
  iysymplt=1,
$end
$heateq
  heat = .false.,
  ischeme = 3,
  tid = 525.0,
  tip = 300.0,
  tia = 100.0,
  cpp = 227.0,
```

```
  cpd = 227.0,
  cpa = 50.0,
  tkp = 432.2,
  tkd = 67.0,
  lhpc = 58900.0,
  hmr = 5.0,
  tl = 510.0,
  ts = 505.0,
  teps = 1.0e-8,
$end
$coupled
  lsvof=.true.,-----------Using CLSVOF method,
  ls=.false.,-------------Not using LS method,
$end
```

Note:
In the *"fldparam"* section, for the free surface code, the variables *"xnul"* and *"xnug"* are replaced by *"xnu", "rhofl"* and *"rhofg"* by *"rhof".*

In the *"coupled"* section, if *"lsvof"* is true, then CLSVOF will be used. If *"lsvof"* is false, the pure VOF method will be used. If both *"lsvof"* and *"ls"* are set to be true, then the pure level set method will be used.

A3. SAMPLE OUTPUT AND DATA POST-PROCESSING

1. Sample OUTPUT

```
3.60034E-001 <----time
 2, 50       <----1st real cell, last real cell in x-direction
 2,100       <----1st real cell, last real cell in y-direction
0.00000E+000 <----location of the left side of each
1.25000E-002      computational cell in x-direction
2.50000E-002
3.75000E-002
5.00000E-002
6.25000E-002
7.50000E-002
8.75000E-002
     .
     .
     .
0.00000E+000 <----location of the lower side of each
1.25000E-002      computational cell in y-direction
2.50000E-002
3.75000E-002
5.00000E-002
6.25000E-002
7.50000E-002
8.75000E-002
```

```
            .
            .
            .
0.00000E+0, 0.00000E+0, 0.00000E+0, 1.80971E-1, 0.00000E+0, 5.21999E-4
7.64340E-4, 0.00000E+0, 0.00000E+0, 1.80971E-1, 0.00000E+0, 5.21999E-4
1.51660E-3, 0.00000E+0, 0.00000E+0, 1.80971E-1, 0.00000E+0, 5.22089E-4
2.24484E-3, 0.00000E+0, 0.00000E+0, 1.80971E-1, 0.00000E+0, 5.22268E-4
2.93749E-3, 0.00000E+0, 0.00000E+0, 1.80971E-1, 0.00000E+0, 5.22534E-4
^            ^           ^           ^           ^           ^
|            |           |           |           |           |
|            |           |           |           |           |
|            |           |           |           |           |
x-velocity  y-velocity   VOF         level set    enthalpy    pressure
component   component    function    function
```

2. Data Post-Processing

In this thesis, all the data files generated from the simulations were post-processed by using MATLAB under the Microsoft Windows system.

REFERENCES

1. Clift, R., Grace, J.R., Webber, M. E., 1978. Bubbles, Drops, and Particles. Academic Press, New York.

2. Taylor, G.I., The viscosity of a fluid containing small drops of another fluid, Proc. R. Soc. Lond. A, (1932), vol. 138, pp. 41-48.

3. Ashgriz, N. & Poo, J.Y., Coalescence and separation in binary collisions of liquid drops. J. Fluid Mech. (1990), vol. 221, pp. 183-204.

4. Qian, J. & Law, C.K., Regimes of coalescence and separation in droplet collision, J. Fluid Mech. (1997), vol. 331, pp. 59-80.

5. Jiang, Y.J., Umemura, A. & Law, C.K., An experimental investigation on the collision behavior of hydrocarbon droplets, J. Fluid Mech. (1992), vol. 234, pp. 171-190.

6. Stone, H.A., Bentley, B.J. & Leal, L.G., An experimental study of transient effects in the breakup of viscous drops, J. Fluid Mech. (1986), vol. 173, pp. 131-158.

7. Stone, H.A. & Leal, L.G., Relaxation and breakup of an initially extended drop in an otherwise quiescent fluid, J. Fluid Mech. (1989), vol. 198, pp. 399-427.

8. Baker, G.R. and D.W. Moore, (1989), The rise and distortion of a two-dimensional gas bubble in an inviscid liquid. Phys. Fluids A 1, 1451-1459.

9. Bhaga, D. and M.E. Weber, (1981), Bubbles in viscous liquids: shapes, wakes and velocities. J. Fluid Mech. 105, 61-85.

10. Scardovelli, R. and Zaleski, S., Direct numerical simulation of free-surface and interfacial flow, Annual Review of Fluid Mechanics *(*January 1999), Vol. 31, pp. 567-603.

11. Bourlioux, A., A coupled level-set volume-of-fluid algorithm for tracking material interfaces, Proc. 6th Int. Symp. On computational fluid dynamics, (1995), Lake Tahoe, CA, pp. 15-22.

12. Sussman, M. and Puckett, E.G., A coupled level set and volume-of-fluid method for computing 3D axisymmetric incompressible two-phase flows, J. Comp. Phys., (2000), Vol. 162, pp. 301-337.

13. Son, G. and Hur, N., A coupled level set and volume-of-fluid method for the buoyancy-driven motion of fluid particles, Numerical Heat Transfer, part B, (2002), Vol. 42, pp. 523-542.

14. Son, G., Efficient Implementation of a coupled level-set and volume-of-fluid method for three-dimensional incompressible two-phase flows, Numerical Heat Transfer, part B, (2003), Vol. 43, pp. 549-565.

15. Mu-Chen, Lu, "Numerical Modeling of Multi-Phase Surface Flow", Ph.D. thesis, The University of Texas at Arlington, 2000.

16. Kothe, D. B., Mjolsness, R. C. and Torrey, M. D., RIPPLE: A computer program for incompressible flows with free surfaces, (1991), Technical Report, LA-12007-MS, Los Alamos National Laboratory.

17. Shyy, W., Udaykumar, H. S., Rao, M. M., and Smith, R. W., Computational Fluid Dynamics with Moving Boundaries, Taylor & Francis, 1996.

18. Ryskin, G, Leal L. G., (1984) Numerical solution of free-boundary problems in fluid mechanics. Part2: Buoyancy-driven motion of a gas bubble through a quiescent liquid. J. Fluid Mech. 148, pp. 1-18.

19. Ryskin, G, Leal L. G., (1984) Numerical solution of free-boundary problems in fluid mechanics. Part2: Buoyancy-driven motion of a gas bubble through a quiescent liquid. J. Fluid Mech. 148, pp. 19-36.

20. Dandy D. S., Leal L. G., (1989), Buoyancy-driven motion of a deformable drop through a quiescent liquid at intermediate Reynolds numbers. J. Fluid Mech. 208, pp.161-192.

21. Hirt, C. W., Cook, J. L. and Butler, T. D., "A Lagrangian Method for Calculating the Dynamics of an Incompressible Fluid with Free Surface," Journal of Computational Physics, Vol. 5, 1970, p. 103.

22. Hirt, C. W., Amsden, A. A. and Cook, J. L., "An Arbitrary Lagrangian-Eulerian Computing Method for all Flow Speeds," Journal of Computational Physics, Vol. 14, 1974, p. 227.

23. Hyman, J., "Numerical Methods for Tracking Interfaces," Fronts, Interfaces, and Patterns, Physics D, North-Holland Physics, New York, 1984.

24. Harlow, F. H. and Welch, J. E., "Numerical Study of Large-Amplitude Free-Surface Motions," Physics of Fluids, Vol. 9, 1966, pp. 842-851.

25. Daly, B. J., Physics of Fluids, "Numerical Study of Two Fluid Rayleigh-Taylor Instability," Vol. 10, 1967, pp. 297-307.

26. Glimm, J., Klingenberg, C., McBryan, O., Plohr, B., Sharp, D. and Yaniv, S., "Front Tracking and Two-Dimensional Riemann Problems," Advances in Applied Mathematics, Vol. 6, 1985, pp. 259-290.

27. Chern, I-L., Glimm, J., McBryan, O., Plohr, B. and Yaniv, S., "Front Tracking for Gas Dynamics," Journal of Computational Physics, Vol. 62, 1986, pp. 83-110.

28. Unverdi, S. O. and Tryggvason, G., "A Front-Tracking Method for Viscous Incompressible Multi-Fluid Flows," Journal of Computational Physics, Vol. 100, 1992, pp. 25-37.

29. Juric, D. and Tryggvason, G., "A Front-Tracking Method for Dendritic Solidification," Journal of Computational Physics, Vol. 123, 1996, pp. 127-148.

30. Juric, D., Modeling of Casting, Welding, and Advanced Solidification Processes VIII, New York, 1998.

31. Kane, J. H., (1994), Boundary-Element Analysis. Eaglewood Cliffs, NJ, Prentice Hall.

32. Harlow, F. H., Computer Physics Communications, Vol. 48, 1988, pp. 1-11.

33. Monaghan, J., (1992), Smoothed particle hydrodynamics. Annu. Rev. Astron. Astrophys. 30, pp. 543-574.

34. Belytschko, T., Krongauz, Y., Organ, D., Fleming, M. and Krysl, P., Computer Methods in Applied Mechanics and Engineering, Vol. 139, 1996, pp. 3-47.

35. van Leer, B., "Towards the Ultimate Conservative Difference Scheme. IV. A New Approach to Numerical Convection," Journal of Computational Physics, Vol. 23, 1977, pp. 276-299.

36. Colella, P. and Woodward, P., "The Piecewise Parabolic Method (PPM) for Gas-Dynamical Simulations," Journal of Computational Physics, Vol. 54, 1984, pp. 174-201.

37. Sweby, P. K., Lectures in Applied Mathematics, Vol. 22, 1985, pp. 289-309.

38. Pericleous, K. A. Chan, K. S. and Cross, M., "Free Surface Flow and Heat Transfer in Cavities: the SEA Algorithm," Numerical Heat Transfer, Part B, Vol. 27, 1995, pp. 487-507.

39. Yabe, T. and Xiao, F., Computers in Mathematics Applications, Vol. 29, 1995, pp. 15-25.

40. DeBar, R., Technical Report UCIR-760, Lawrence Livermore National Laboratory, 1974.

41. Nichols, B. D. and Hirt, C. W., Technical Report LA-UR-75-1932, Los Alamos National Laboratory, 1975.

42. Hirt, C. W. and Nichols, B. D., "Volume of Fluid (VOF) Method for the Dynamics of Free Boundaries," Journal of Computational Physics, Vol. 39, 1981, pp. 201-225.

43. Rider, W. J. and Kothe, D. B., Technical Report LA-UR-96-2375, Los Alamos National Laboratory, 1998.

44. Rudman, M., "Volume-Tracking Methods for Interfacial Flow Calculations," International Journal for Numerical Methods in Fluids, Vol. 24, pp. 671-691, 1997.

45. Rudman, M., "A Volume-Tracking Method for Incompressible Multifluid Flows with Large Density Variations," International Journal for Numerical Methods in Fluids, Vol. 28., pp. 357-378, 1998.

46. Osher, S. and Sethian, J. A., "Fronts Propagating with Curvature-Dependent Speed: Algorithms Based on Hamilton-Jacobi Formulations," Journal of Computational Physics, Vol. 79, 1988, pp. 12-49.

47. Osher, S., Fedkiw, R., Level set methods and dynamic implicit surfaces. New York: Springer, 2002.

48. Sethian, J. A., Smereka, P., Level set methods for fluid interfaces. Annu. Rev. Fluid Mech., (2003), 35, pp. 341-372.

49. Sussman, M., Smereka, P. and Osher, S., A level set approach for computing solutions to incompressible two-phase flow, *J. Comp. Phys.*, (1994), Vol. 114, pp. 146-154.

50. Boettinger, W. J., Warren, J. A., Beckermann, C., Karma, A., Phase-field simulation of solidification. Annu. Rev. Mater. Res., (2002), 32, pp. 163-194.

51. Badalassi, V. E., Ceniceros, H. D., Banerjee, S., Computation of multiphase systems with phase field models. Journal of computational physics.(2003), 190, pp. 371-397.

52. Shin, S., Juric, D., Modeling three-dimensional multiphase flow using a level contour reconstruction method for front tracking without connectivity, J. Comput. Phy. 180 (2002) 427-470.

53. Tryggvason,G., Bunner, B., Esmaeeli, A., Juric, D., Al-Rawahi, N., Tauber,W., Han, J., Nas, S., and Jan, Y.-J. "A Front Tracking Method for the Computations of Multiphase Flow", Journal of Computational Physics, Volume 169, pp. 708-759, 2001.

54. Shin, S., Abdel-Khalik, S.I., Daru, V. and Juric, D., Accurate representation of surface tension using the level contour reconstruction method, *J. Comp. Phys.*, (2004), in Press.

55. Popinet, S. and Zaleski, S., A front-tracking algorithm for the accurate representation of surface tension, *Int. J. Numer. Methods Fluids,* (1999), Vol. 30, pp. 775-793.

56. Brackbill, J. U., Kothe, D. B., and Zemach, C., "A Continuum Method for Modeling Surface Tension," Journal of Computational Physics, Vol. 100, pp. 335-354, 1992.

57. Renardy, Y. and Renardy, M., PROST: a parabolic reconstruction of surface tension for the volume-of-fluid method, *J. Comp. Phys.,* (2002), Vol. 183, pp. 400-421.

58. Meier, M., Yadigaroglu, G. and Smith, B. L., A novel technique for including surface tension in PLIC-VOF methods, *European Journal of Mechanics B - Fluids,* (2002), Vol. 21, pp. 61-73.

59. Kang, M., Fedkiw, R. and Liu, X.-D., A Boundary Condition Capturing Method for Multiphase Incompressible Flow, *J. Sci. Compt.,* (2000), Vol. 15, pp. 323-360.

60. Torrey, M. D., Cloutman, L. D., Mjolsness, R. C., and Hirt, C. W., "NASA-VOF2D : A Compueter Program for Incompressible Flows with Free Surfaces," Technical Report, LA-10612-MS, 1985.

61. Mangiavacchi, N., Castelo, A., Tome, M. F., Cuminato, J. A., Oliveira, M. L. B. D., Mckee, S., An effective implementation of surface tension using the marker and cell method for axisymmetric and planar flows. *Siam J. Sci. Comput.*, Vol. 26, No. 4, pp.1340-1368.

62. Kershaw, D. S., "The Incomplete Cholesky-Conjugate Gradient Method for the Iterative Solution of Systems of Linear Equations," *Journal of Computational Physics*, Vol. 26, pp. 43-65, 1978.

63. Zalesak, S. T., "Fully Multi-Dimensional Flux Corrected Transport Algorithms for Fluid Flow," *Journal of Computational Physics*, Vol. 31, pp. 335-362, 1979.

64. Private communications.

65. Helenbrook, B.T., Martinelli, L. and Law, C.K., A numerical method for solving incompressible flow problems with a surface of discontinuity, *J. Comp. Phys.*, (1999), Vol. 148, pp. 366-396.

66. Fedkiw, R., Aslam, T., Merriman, B., and Osher, S., A non-Oscillatory Eulerian Approach to Interfaces in Multimaterial Flows (The Ghost Fluid Method), *J. Comp. Phys.*, (1999), Vol.152, pp. 457-492.

67. Gibou, F., Fedkiw, R., Cheng, L. T.and Kang, M., A second order accurate symmetric discretization of the Poisson equation on irregular domains, *J. Comput. Phys.*, (2002), Vol. 176, pp. 205-227.

68. Liu, X.-D., Fedkiw, R. and Kang, M., A Boundary Condition Capturing Method for Poisson's Equation on Irregular Domains, *J. Comp. Phys.,* (2000), Vol.160, pp. 151-178.

69. Tomiyama, A., Celata, G.P., Hosokawa, S., Yoshida, S., 2002. Terminal velocity of single bubbles in surface tension force dominant regime. Int. J. Multiphase Flow 28, 1497-1519.

70. Ryohei Kamiya, "A Numerical Study of Pendant Drop Formation From a Capillary Tube", Master's thesis, The University of Texas at Arlington, 2005.

71. Zhang, X. and Basaran, O. A., "An experimental study of dynamics of drop forma-tion", *Phys. Fluids*, 1995, pp.1184-1203.

72. Zhang, X., "Dynamics of growth and breakup of viscous pendant drops into air", *J.Colloid Interface Sci*., Vol. 212, 1999, pp.107-122.

73. Ha, J. W. and Leal, L. G., "An experimental study of drop deformation and breakup in extensional flow at high capillary number," Phys. Fluids **13**, 1568(2001).

74. Kelley, E., Wu, M.M., 1997. Path instabilities of rising air bubble in a hele-shaw cell. Phys. Rev. Lett. 79(7), 1265-1268.

75. Mougin, G., Magnaudet, J., 2002. Path Instability of a rising bubble. Phys. Rev. Lett. 88(1), 014502.

76. de Vries, A.W.G., Biesheuvel, A., van Wijngaarden, L., 2002. Notes on the path and wake of a gas bubble rising in pure water. Int. J. Multiphase Flow 28, 1823-1835.

77. de Vries, A.W.G., 2001. Path and wake of a rising bubble. Ph.D. Thesis, University of Twente.

78. Ellingsen, K., Risso, F., 2001. On the rise of an ellipsoidal bubble in water: oscillatory paths and liquid-induced velocity. J. Fluid Mech. 440, 235-268.

79. Di Marco, P., Grassi, W., Memoli, G., 2003. Experimental study on rising velocity of nitrogen bubbles in FC-72. Int. J. Thermal Sci. 42, 435-446.

80. Tomiyama, A., Celata, G.P., Hosokawa, S., Yoshida, S., 2002. Terminal velocity of single bubbles in surface tension force dominant regime. Int. J. Multiphase Flow 28, 1497-1519.

81. Fabre, J., Line, A., (1992). Modeling of two-phase slug flow. Annu. Rev. Fluid Mech., 24, 21-46.

82. Viana, F., Pardo, R., Yanez, R., Trallero, Jose L., Joseph, Daniel D., 2003. Universal correlation for the rise velocity of long gas bubbles in round pipes. J. Fluid Mech. 494, 379-398.

83. van Hout, R., Gulitski, A., Barnea, D., Shemer, L., 2002. Experimental investigation of the velocity field induced by a Taylor bubble rising in stagnant water. Int. J. Multiphase Flow 28, 579-596.

84. Polonsky, S., Shemer, L., Barnea, D., 1999. The relation between the Taylor bubble motion and the velocity field ahead of it. Int. J. Multiphase Flow 25, 957-975.

85. Bugg, J.D., Saad, G.A., 2002. The velocity field around a Taylor bubble rising in a stagnant viscous fluid: numerical and experimental results. Int. J. Multiphase Flow 28, 791-803.

86. Bugg, J.D., Mack, K., Rezkallah, K.S., 1998. A numerical model of Taylor bubbles rising through stagnant liquids in vertical tubes. Int. J. Multiphase Flow 24, 271-281.

87. Polonsky, S., Barnea, D., Shemer, L., 1999. Averaged and time-dependent characteristics of the motion of an elongated bubble in a vertical pipe. Int. J. Multiphase Flow 25, 795-812.

88. Lamb, H., 1932. Hydrodynamics, article 191. Cambridge University Press, Cambridge, pp. 284-290.

BIOGRAPHICAL INFORMATION

Zhaoyuan Wang was born in Shandong, China. He received his B.E. degree in 1997 and M.E. degree in 2000 both in Thermal Engineering from Northeastern University at Shenyang, China. After graduation, he became a lecturer in Guangdong Mechanical and Electrical College (Guangzhou, China). He entered The University of Texas at Arlington for his PhD study in Mechanical Engineering in August 2002. He received his PhD degree in May 2006.